

9. SITE 997¹

Shipboard Scientific Party²

HOLE 997A

Position: 31°50.588'N, 75°28.118'W

Start hole: 1825 hr, 6 December 1995

End hole: 0015 hr, 10 December 1995

Time on hole: 122.50 hr (5.10 days)

Seafloor (drill pipe measurement from rig floor, mbrf): 2781.6

Total depth (drill pipe measurement from rig floor, mbrf): 3215.9

Distance between rig floor and sea level (m): 11.5

Water depth (drill pipe measurement from sea level, m): 2770.1

Penetration (mbsf): 434.3

Coring totals:

Type: APC

Number: 19

Cored: 165.9 m

Recovered: 173.77 m (104.7%)

Type: XCB

Number: 28

Cored: 260.4 m

Recovered: 166.54 m (64.0%)

Type: PCS

Number: 8

Cored: 8.0 m

Recovered: 2.77 m (34.6%)

Formation:

Unit I: 0–6.2 mbsf; Holocene to late Pleistocene; light greenish gray foraminifer-bearing nannofossil-rich clay

Unit II: 6.2–107.83 mbsf; late Pleistocene to late Pliocene; light greenish gray nannofossil-rich clay and diatom-rich nannofossil-rich clay

Unit III: 107.83–434.3 mbsf; early to late Pliocene; dark greenish gray diatom-bearing nannofossil-bearing clay and claystone

HOLE 997B

Position: 31°50.598'N, 75°28.110'W

Start hole: 0045 hr, 10 December 1995

End hole: 730 hr, 17 December 1995

Time on hole: 175.25 hr (7.30 days)

Seafloor (drill pipe measurement from rig floor, mbrf): 2781.6

Total depth (drill pipe measurement from rig floor, mbrf): 3532.3

Distance between rig floor and sea level (m): 11.5

Water depth (drill pipe measurement from sea level, m): 2770.1

Penetration (mbsf): 750.7

Coring totals:

Type: XCB

Number: 38

Cored: 356.3 m

Recovered: 239.63 m (67.3%)

Type: PCS

Number: 9

Cored: 9.0 m

Recovered: 1.62 m (18.0%)

Formation:

Unit III: 318.5–750.7 mbsf; late Pliocene to late Miocene; dark greenish gray diatom-bearing nannofossil-bearing clay and claystone

Principal results: Site 997 is located on the topographic crest of the Blake Ridge, in an area where an extremely well-developed and distinct BSR exists. It is the last of three sites (994, 995, and 997) drilled along a transect extending from the ridge flank where this BSR is not detectable (Site 994), to the ridge crest (Site 997). Along this transect, variations in seismic blanking and development of the BSR are especially distinct. However, the geology and topography are relatively simple, providing an opportunity to assess basic properties of gas hydrate-bearing sediments and to understand lateral hydrate variations caused by local lithologic, chemical, and hydrologic factors.

The sedimentary section recovered at Site 997 is a composite 750-m section of Holocene to upper Miocene sediments and sedimentary rocks. Three lithostratigraphic units are recognized on the basis of sediment composition, primarily variations in the nannofossil, diatom, and total carbonate contents. These lithostratigraphic units and their lithologies are very similar to those at Sites 994 and 995.

Unit I (0–6.2 mbsf) consists of interbeds of foraminifer-bearing nannofossil-rich clay with color repetition of light gray and greenish gray. The uppermost 19 cm of grayish brown bioturbated foraminifer-bearing nannofossil-rich clay is identified as Subunit IA; sediments below (0.19–6.2 mbsf) comprise Subunit IB. Beds with disseminated and concentrated glauconite occur, especially in the basal portion. Total carbonate contents range from 11 to 50 wt% CaCO₃.

Unit II (6.2–107.3 mbsf) consists of interbeds of greenish gray, intensely burrowed nannofossil-rich clay and darker colored bioturbated clay with lower nannofossil abundance. The top of the unit is marked by a sharp decrease in nannofossil abundance to <20% and the appearance of diatoms. Diatom abundances reach 35% in the interval from 37.9 to 50.4 mbsf. Total carbonate contents decrease to <30%.

Unit III (107.3–750.0 mbsf) consists of homogeneous, dark greenish gray diatom-bearing nannofossil-bearing clay and claystone, with two diatom-rich intervals at 146.9–183.2 and 452.6–587.2 mbsf. The top is marked by the last occurrence of a mottled nannofossil-bearing clay bed. Total carbonate contents decrease to <20% with nannofossil abundance <10%.

Evidence for contourite deposition extending back into the Miocene is suggested by a foraminifer-rich graded bed at 722.23–723.24 mbsf, which is the deepest occurrence of such beds at the three sites on the Blake Ridge. Rare intervals of thin, parallel laminations in Unit III may also indicate contour-current activity.

Two intervals of diatom-rich sediments in Unit III from all three Blake Ridge sites (160–232 mbsf and 430–660 mbsf at Site 994, 131.9–252.3

¹Paull, C.K., Matsumoto, R., Wallace, P.J., et al., 1996. *Proc. ODP, Init. Repts.*, 164: College Station, TX (Ocean Drilling Program).

²Shipboard Scientific Party is given in the list of participants that precedes the Table of Contents.

mbsf and 464.2–656.0 mbsf at Site 995, and 146.9–183.2 mbsf and 452.6–587 mbsf at Site 997) occur at times of higher sedimentation rates, as deduced from the nannofossil biostratigraphy (~5.8–5.0 and 3.0–2.6 Ma).

The 750-m sequence recovered at this site is Holocene to late Miocene in age. Two short hiatuses were detected in the upper lower Pleistocene and upper lower Pliocene, and the third short hiatus is likely in the upper Miocene. Nannofossils are abundant throughout the cores, and below 30 mbsf they showed evidence of weak dissolution. Sedimentation rates increased with depth throughout the sedimentary sequence. Because of a hiatus and coring gap detected between Cores 164-997A-1H and 2H, the Quaternary sedimentation rate at Site 997 (40 m/m.y.) is only two-thirds of the value observed at Sites 994 and 995. The Pliocene rates calculated excluding the hiatuses (133 m/m.y.), however, are the highest among the three sites. The minimum rate for the upper Miocene is more than 340 m/m.y., which is very close to the value obtained for the uppermost Miocene sequence at Hole 994C. The oldest age estimated at Hole 997B is ~6.4 Ma.

A well-defined magnetostratigraphy can be defined for the upper part of Site 997. The lower boundary of the C1r.1n subchron (Jaramillo normal chron) is at 52 mbsf. The upper and lower boundaries of the C2n (Olduvai normal chron) are at 72 and 84 mbsf, respectively, and the C2An/C2r boundary (Gauss/Matuyama boundary) is at 122 mbsf. The C1n/C1r boundary (Brunhes/Matuyama boundary) and the upper boundary of the C1r.1n (top of Jaramillo normal chron) are tentatively defined at 36 and 41 mbsf, respectively.

Sediment physical properties at Site 997 are generally similar to those at Sites 994 and 995. Most notably, all three sites have a well-defined lowermost unit (upper boundary at 610–625 mbsf) in which wet bulk density increases with depth more rapidly than in the overlying and largely homogeneous unit that makes up most of the sedimentary section.

Rock magnetism defines a similar downhole sequence of reduction steps to that seen at Sites 994 and 995. Magnetite authigenesis from 0 to 2 mbsf is followed by reduction of magnetite to pyrite via magnetic sulfides. Two reduction styles are apparent. The first is a background trend of magnetite-greigite-pyrite conversion in which greigite apparently develops within the first 20 mbsf in response to bacterial oxidation of organic material and is progressively reduced to pyrite downhole. A second generation of greigite, as observed at Sites 994 and 995, extends downward to ~260–300 mbsf. Rock-magnetic data suggest that the second-generation greigite has been largely reduced to pyrite below 300 mbsf. Site 997 differs from Sites 994 and 995 in that magnetic sulfide development within the interval above 260 mbsf is more consistent from sample to sample and that the conversion of greigite to pyrite in the interval from 300 to 400 mbsf is more complete.

Seventeen in situ temperature measurements were obtained between 0 and 414.1 mbsf in Hole 997A using the Adara and WSTP tools and a prototype thermal probe (DVTP) designed by E. Davis and H. Villinger. The data indicate that Site 997 is characterized by a linear geothermal gradient of 36.9 ± 0.4 mK/m, which is within 1 standard deviation of the estimated gradient at Site 994 (36.4 ± 1.3 mK/m) and 9% higher than the gradient at Site 995 (33.5 ± 0.9 mK/m). The estimated temperatures at the BSR are 18.7°C (440 mbsf) at Site 995 and 20.0°C (450 mbsf) at Site 997. At Site 994, where there is no BSR, the temperature at a comparable depth (440 mbsf) is estimated at 20.1°C. On the Blake Ridge, sediments overlying a BSR (Sites 995 and 997) are not uniformly cooler than those at a comparable depth in a location with no BSR (Site 994) as would be expected if gas trapped below the BSR acted as an insulator and caused heat to be refracted to an area lacking a BSR. Heat flow estimated from the in situ temperature data in Hole 997A is 20% lower than earlier determinations (Ruppel et al., 1995) based on the results of a traditional deep-sea heat-flow survey conducted within a few kilometers of the site.

The concentrations of methane in headspace gas samples increase from 0.022 mL/kg of sediment near the sediment-water interface to a maximum of 180 mL/kg at a depth of 50.4 mbsf. The concentration steadily declines to ~6.6 mL/kg near 210 mbsf and thereafter remains at concentrations ranging from 0.4 to 61 mL/kg. Notable spikes in methane

concentrations occurred in the same intervals in which gas hydrate was found or inferred by catwalk core temperature measurements. Methane/ethane ratios decrease with depth and reach a minimum of 109 at 725.8 mbsf. Higher molecular weight hydrocarbons are present throughout the hole in <100 ppm concentrations and increase with depth. Heptane occurs from 153.3 to 750.0 mbsf. Microscopically visible oil occurred from ~500 to 620 mbsf. This observation, coupled with the occurrence of higher molecular weight hydrocarbon gases, suggests some migration of oil and gas. The TOC contents of the sediments are near 1% above 200 mbsf and ~1.5% in the interval from 200 to 700 mbsf. The amount and composition of volatile and nonvolatile organic matter are very similar to those found at Sites 994 and 995.

The interstitial-water chemistry at Site 997 is very similar to that documented at Sites 994 and 995. Downhole profiles of interstitial-water compositional data show the same general trends with the same approximate depths for maxima and minima as those seen at the other Blake Ridge sites. However, absolute concentrations differ from site to site. Chloride profiles have been used as a proxy indicator of the amount of in situ gas hydrate. The zone of anomalous chloride concentrations occurs at approximately the same depths (~200–440 mbsf) over the 9.6-km transect. Furthermore, the two depth intervals showing the largest chloride anomalies, at ~250 and ~400 mbsf, also are depth correlative. Thus, the similarity of the Cl⁻ profiles at the ridge sites strongly suggests that the gas hydrate zones are correlative over the expanse of the Blake Ridge. The amount of gas hydrate appears to increase from the ridge flank (Site 994) to the ridge crest (Site 997). There is a minimum of ~1.4%, 1.7%, and 2.1% gas hydrate at Sites 994, 995, and 997, respectively, assuming (1) that the chloride excursions represent dilution of interstitial-water chloride by dissociating hydrate, (2) a background chloride value of 512 mM, and (3) sediment porosity of 50%.

The PCS was successfully deployed 11 times at Site 997, including one deployment to determine the volume and composition of gas in sediment immediately below the prominent BSR at 462 mbsf. The volume of methane evolved from this particular PCS core suggests that interstitial waters at this depth are 10 times oversaturated with methane. Chemical analyses also show that pore waters at this depth do not have the low chloride concentrations associated with the presence of gas hydrate. Together, these observations provide the first direct evidence for significant free gas immediately below a BSR.

Zero-offset vertical seismic profiling was conducted between 120 and 712 mbsf during two lowerings of the three-component WHOI borehole seismometer in Hole 997B. During the first lowering, air gun shots were fired at 8-m intervals from 120 to 712 mbsf. During the second lowering, shots from both the air and water guns were recorded at 4-m intervals from 164 to 684 mbsf. A stacked air gun section shows clear downgoing first arrivals and an upgoing reflection from the BSR. The depth of the BSR is defined by the intersection of its reflection with the downgoing arrival at 464 ± 8 mbsf. Beneath the BSR, velocities decrease rapidly to a minimum of 1400 m/s at 480 mbsf and remain lower than ~1650 m/s to the base of the hole.

A suite of wireline logs, including natural gamma, bulk density, electrical resistivity, *P*-wave sonic, *S*-wave sonic, geochemical, and Formation MicroScanner, was run in Hole 997B from 113 to 715 mbsf. Preliminary analysis of the *P*-wave acoustic and electrical resistivity logs shows a pattern similar to those at Sites 994 and 995, with low acoustic velocities (~1600 m/s) in the top of the hole that begin to increase at 186 mbsf to a maximum of 2000 m/s at 451 mbsf before decreasing again to 1100 m/s at 597.0 mbsf. The electrical resistivity and *P*-wave acoustic velocity measurements are consistent with the presence of gas hydrate in the zone from 186 to 451 mbsf and with the presence of free gas in the section below 451 mbsf.

BACKGROUND AND OBJECTIVES

Site 997, on the crest of the Blake Ridge, was the second site of Leg 164 to penetrate below the base of gas hydrate stability where a

strong BSR exists (Fig. 1). Sites 994, 995, and 997 form a transect that is intended to help establish lateral variations in the extent of gas hydrate and refine our understanding of the lateral development of BSRs (Fig. 2) within similar sedimentary sequences.

The geologic setting of Site 997 is similar to that of Sites 994 and 995. All these sites are on the Blake Ridge, a Neogene sediment drift (Tucholke and Mountain, 1979). Previous drilling (DSDP Sites 102, 103, 104, and 533; Shipboard Scientific Party, 1972; Gradstein and Sheridan, 1983) has shown that this sediment drift is largely composed of fine-grained nannofossil-bearing hemipelagic sediments that accumulated at unusually high rates.

Site 997 is located on the crest of the Blake Ridge in 2770.1 m water depth. Seismic reflection profiles over Site 997 (Fig. 2) lack significant reflections between 0.3 and 0.55 s sub-bottom. However, a well-developed BSR is at 0.55 s sub-bottom. The reflective section below the BSR is ~0.2 s thick.

Gas hydrate development may be extensive at Site 997. The distribution of the BSR and structure contours on the BSR surface in the area around Site 997 are shown in Figure 1. Many previous workers have noted that BSR development is characteristically strong on the crest of the Blake Ridge (Markl et al., 1970; Tucholke et al., 1977; Shipley et al., 1979; Dillon et al., 1980; Paull and Dillon, 1981; Dillon and Paull, 1983; Markl and Bryan, 1983; Katzman et al., 1994). Because the BSR mimics the seafloor topography, the surface formed by the BSR has structural closure in three directions along the crest of the Blake Ridge (Dillon et al., 1980). The base of the gas hydrate stability zone may act as a relative seal because gas hydrate development will reduce the porosity (and possibly the permeability) of the sediment. Thus, buoyant fluid and gas migration will be preferentially directed upslope from the flanks to the crest of the Blake Ridge.

The specific objectives at Site 997 are:

1. To assess the amount and lateral extent of gas trapped in gas hydrate-bearing sediments (Comparative studies between Sites 994, 995, and 997 will provide insight into the utility of acoustic techniques for assessing the amounts of gas hydrate in marine sediments);
2. To establish whether the topography of the Blake Ridge is acting as a trap that will concentrate buoyant fluids and gases;
3. To establish temperature gradients to assess the relationship between the theoretical position of the base of the gas hydrate stability zone and the position of the BSR; and
4. To recover data on in situ characteristics of the sediments to (1) estimate the total amount of gas hydrate at these Sites, (2) establish the sources of the gases associated with the gas hydrate (e.g., in situ-produced microbial mediated gases, migrated and concentrated microbial gases, or migrated thermogenic gases), and (3) recover natural gas hydrate samples to determine the hydrate crystal structure, composition, and volumetric ratio of gas to water.

OPERATIONS

Transit to Site 997

The sea voyage to Site 997 (prospectus site BRH-1a) covered 98 km in 4.2 hr at an average speed of 12.6 kt. A Datasonics beacon 354M was dropped at the Global Positioning System coordinates. Drillers were advised of the increased potential for hydrocarbons at Hole 997A, based on geological and seismic evidence. Dynamic well-control procedures were reviewed, and 10.5 ppg kill-weight mud was prepared.

Hole 997A

The same BHA was run with a polycrystalline diamond compact drill (PDC) bit and nonmagnetic drill collar. Hole 997A was spudded

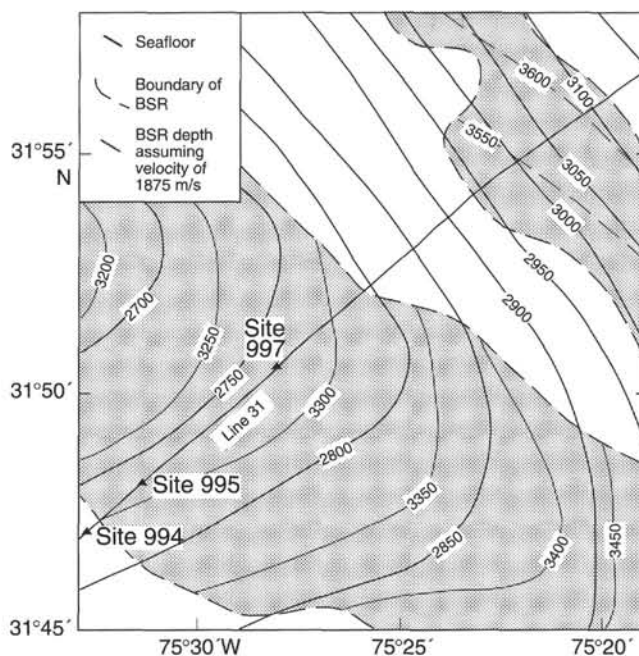


Figure 1. Map showing bathymetry, the distribution of the BSR, the depth to the BSR surface (assuming a velocity of 1875 m/s), and the position of seismic Profile CH-06-92 Line 31 (shown in Fig. 2) in the area where Sites 994, 995, and 997 were drilled. Depths to the BSR were calculated using pre-leg velocity estimates, which are higher than those measured during Leg 164 (see "Geophysics" section, this chapter). Contours are in meters. Shading indicates the regions in which a BSR is present.

at 1825 hr on 6 December. The seafloor was estimated at 2770.1 mbsl, based on recovery of a mudline. Nineteen APC cores (164-997A-1H through 17H and 19H and 20H) were taken from 0 to 146.9 mbsf and from 147.9 to 166.9 mbsf (Table 1), with a total of 165.9 m cored (104.7% recovery). A single PCS core (164-997A-18P) was taken from 146.9 to 147.9 mbsf, with 1.0 m cored and 0.45 m recovered. Cores were oriented from Core 164-997A-3H. Adara temperature measurements were taken at Cores 164-997A-2H, 4H, 10H, 13H, 16H, and 20H. WSTP temperature and water samples were taken after Cores 164-997A-6H, 10H, 13H, 16H, and 18P. The FWS was deployed before Core 164-997A-15H.

Twenty-eight XCB cores and seven PCS cores were taken from 166.9 to 434.3 mbsf. The XCB cores (164-997A-21X through 54X) were obtained by coring 260.4 m (64.1% recovery). The PCS cores (164-997A-18P, 25P, 29P, 33P, 40P, 49P, 51P, and 55P) were obtained by coring 7.0 m, with 1.47 m recovered (21.0% recovery). Massive gas hydrate was recovered in Core 164-997A-42X (327.4–337.0 mbsf).

Previous PCS runs during Leg 164 were evaluated to determine the optimum conditions for recovery. The most successful PCS coring technique was to force the push-in shoe as deep as possible using a push-in force of 15,000–20,000 lb weight on bit (wob) for 5 min, followed by 0.5 m (or 5 min) advance by rotation at 20–30 rpm. Circulation at 200 gpm was used if required to force the shoe to advance. The 36³/₈-in-long extension was used until the formation became hard, followed by the 18¹/₈-in extension. The basket core catcher was used while the supply lasted. The auger shoe was used when recovery decreased below 0.20 m. The PCS cores were all obtained using the push-in shoe, and coring results are summarized below in the "Down-hole Tools and Sampling" section, this chapter.

Cores 164-997A-29P, 33P, and 40P were pushed in without rotation and had no recovery; however, they were followed by successful coring runs in which rotation was used. This result suggests that ro-

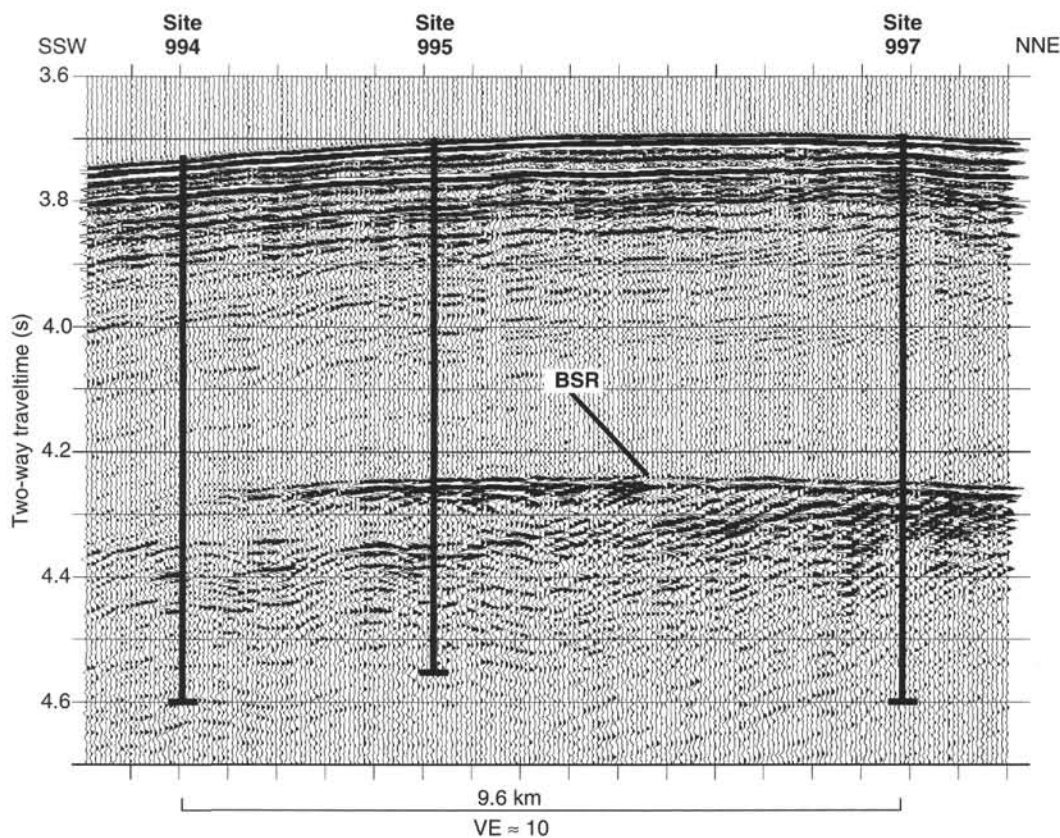


Figure 2. Seismic reflection Profile CH-06-92 Line 31 along which Sites 994, 995, and 997 were drilled.

tation is useful in moderately compacted clays after pushing in. The PCS push-in shoe unscrewed from the core barrel after taking Core 164-997A-55P. An attempt to recover the shoe with a modified GS overshot was unsuccessful. Two set screws were added to the PCS push-in and auger-type shoes to lock them on the core barrel. The PDC bit would have been destroyed by rotation on the shoe; therefore, coring was terminated. The hole was filled with sepiolite mud, and the pipe was pulled, clearing the seafloor at 0010 hr on 10 December.

Hole 997B

The ship was moved 20 m northeast, and Hole 997B was spudded at 0045 hr on 10 December. The same seafloor depth of 2770.1 mbsf was used. The hole was drilled with a center bit to 318.5 mbsf at 41.1 m/hr. Three XCB cores were taken over the interval in Hole 997A where a large hydrate section was recovered. Cores 164-997B-1X through 3X were taken from 318.5 to 347.3 mbsf, with 28.8 m cored and 12.57 m recovered (43.6% recovery). The hole was drilled with a center bit from 347.3 to 414.2 mbsf at 26.7 m/hr.

Nine PCS and 35 XCB cores were attempted from 414.2 to 750.7 mbsf. One PCS water sample was taken after Core 164-997B-28X at 606.5 mbsf. Nine PCS cores (164-997B-6P, 10P, 15P, 21P, 25P, 32P, 36P, 40P, and 44P) were taken, with 9.0 m cored and 1.62 m recovered (18% recovery). The practical depth limit for the PCS push-in shoe appears to be ~450 mbsf in these clays. Thirty-five XCB cores (164-997B-4X through 47X) were taken from 414.2 to 750.7 mbsf, with 357.3 m cored and 239.63 m recovered (67.1% recovery).

The formation was predominately a gassy, dry clay except for a 2-m hard section at 447–449 mbsf (near the BSR at ~450 mbsf). Core was lost by extrusion from the liner top, and most cores showed clear indications of gas expansion. The C_1/C_2 ratio in headspace gas sam-

ples declined from 20,000–16,000 at 35–65 mbsf to 109 at 725 mbsf, indicating that the mostly methane gas was biogenic in origin with some migration of heavy hydrocarbons, especially below 450 mbsf. A geothermal gradient of 36.9°C/km was assumed, based on Hole 997A. The C_1/C_2 ratios declined in vacutainer samples from 108 mbsf and remained steady below 466 mbsf. Iso/normal C_4 through C_6 ratios decreased below 466 mbsf, a mild to strong petroleum odor was common, and a light yellow fluorescence was noted in sediments from 452.6 to 568.0 mbsf (see “Organic Geochemistry” section, this chapter).

A 35-bbl sepiolite mud sweep was circulated, and a wiper trip was made to 80 mbsf to condition the hole for logging. A maximum overpull of 40,000 lb was encountered pulling out of the hole, with a maximum drag of 40,000 lb at 578 mbsf running in. The hole was reamed from 565 to 660 mbsf with no fill on the bottom. No sticking tendency was noted. The hole was displaced with sepiolite/seawater mud. The pipe was pulled back to 103 mbsf, and the conical side-entry sub (CSES) was rigged up. Following a downhole tool failure, a DITE/SDT/HLD/NGT/LDEO-TLT log was run in 13 hr to 747.4 mbsf with the CSES.

The WHOI triaxial VSP tool was run in the pipe with the CSES to 690 mbsf. The tool stopped at 314 mbsf and had to be pumped out of the pipe with 800 psi of pressure. A zero-offset VSP survey was conducted in 13.25 hr, with the tool clamped at 8-m intervals from 714 mbsf. The 300-in³ water gun failed, so the survey was run with an air gun only. The LDEO-SST tool was run, but the tool failed and the Gearhart Owens head was replaced. The tool was run with the CSES to 660.8 mbsf and was pumped out of the drill string. The LDEO-SST log was run in 6.25 hr from 660.8 mbsf. The GLT was run next, followed by the Formation MicroScanner. Following the logging runs, another ZO-VSP was run using the WHOI triaxial VSP tool and both air and water guns.

Table 1. Coring summary for Site 997.

Core	Date (Dec. 1995)	Time (UTC)	Depth (mbsf)	Length cored (m)	Length recovered (m)	Recovery (%)	Core	Date (Dec. 1995)	Time (UTC)	Depth (mbsf)	Length cored (m)	Length recovered (m)	Recovery (%)
164-997A-							164-997B-						
1H	6	2340	0.0-2.9	2.9	2.94	101.0	1X	10	1420	318.5-328.1	9.6	3.34	34.8
2H	7	0045	2.9-12.4	9.5	9.35	98.4	2X	10	1530	328.1-337.7	9.6	3.84	40.0
3H	7	0140	12.4-21.9	9.5	9.94	104.0	3X	10	1640	337.7-347.3	9.6	5.39	56.1
4H	7	0245	21.9-31.4	9.5	9.82	103.0	4X	10	2045	414.2-423.8	9.6	1.97	20.5
5H	7	0330	31.4-40.9	9.5	9.84	103.0	5X	10	2155	423.8-433.4	9.6	4.43	46.1
6H	7	0440	40.9-50.4	9.5	10.12	106.5	6P	10	2255	433.4-434.4	1.0	0.24	24.0
7H	7	0700	50.4-52.9	2.5	2.53	101.0	7X	11	0025	434.4-443.0	8.6	0.00	0.0
8H	7	0800	52.9-61.4	8.5	8.30	97.6	8X	11	0210	443.0-452.6	9.6	9.58	99.8
9H	7	0900	61.4-70.9	9.5	10.07	106.0	9X	11	0330	452.6-462.2	9.6	0.13	1.4
10H	7	1005	70.9-80.4	9.5	10.03	105.6	10P	11	0430	462.2-463.2	1.0	0.14	14.0
11H	7	1205	80.4-89.9	9.5	10.00	105.2	11X	11	0600	463.2-471.8	8.6	7.15	83.1
12H	7	1250	89.9-99.4	9.5	8.94	94.1	12X	11	0725	471.8-481.5	9.7	5.40	55.7
13H	7	1355	99.4-108.9	9.5	10.76	113.2	13X	11	0845	481.5-491.1	9.6	5.41	56.3
14H	7	1555	108.9-118.4	9.5	10.34	108.8	14X	11	1000	491.1-500.8	9.7	5.15	53.1
15H	7	1755	118.4-127.9	9.5	10.10	106.3	15P	11	1100	500.8-501.8	1.0	0.30	30.0
16H	7	1910	127.9-137.4	9.5	10.12	106.5	16X	11	1225	501.8-510.4	8.6	9.74	113.0
17H	7	2115	137.4-146.9	9.5	9.67	102.0	17X	11	1350	510.4-520.0	9.6	2.11	22.0
18P	7	2210	146.9-147.9	1.0	0.42	42.0	18X	11	1515	520.0-529.6	9.6	9.47	98.6
19H	8	0015	147.9-157.4	9.5	10.94	115.1	19X	11	1640	529.6-539.2	9.6	7.03	73.2
20H	8	0130	157.4-166.9	9.5	10.00	105.2	20X	11	1815	539.2-548.8	9.6	6.23	64.9
21X	8	0235	166.9-173.5	6.6	3.54	53.6	21P	11	1915	548.8-549.8	1.0	0.94	94.0
22X	8	0445	173.5-183.2	9.7	8.20	84.5	22X	11	2050	549.8-558.4	8.6	8.84	103.0
23X	8	0545	183.2-192.8	9.6	0.00	0.0	23X	11	2220	558.4-568.0	9.6	9.59	99.9
24X	8	0630	192.8-202.4	9.6	0.00	0.0	24X	11	2355	568.0-577.6	9.6	7.53	78.4
25P	8	0745	202.4-203.4	1.0	0.88	88.0	25P	12	0100	577.6-578.6	1.0	0.00	0.0
26X	8	1000	203.4-212.0	8.6	7.28	84.6	26X	12	0250	578.6-587.2	8.6	5.12	59.5
27X	8	1050	212.0-221.6	9.6	8.81	91.8	27X	12	0435	587.2-596.9	9.7	9.09	93.7
28X	8	1145	221.6-231.3	9.7	3.81	39.3	28X	12	0610	596.9-606.5	9.6	6.26	65.2
29P	8	1230	231.3-232.3	1.0	0.00	0.0	29X	12	0845	606.5-616.1	9.6	8.28	86.2
30X	8	1320	232.3-240.9	8.6	4.31	50.1	30X	12	1015	616.1-625.7	9.6	4.47	46.5
31X	8	1545	240.9-250.5	9.6	7.91	82.4	31X	12	1205	625.7-635.3	9.6	10.00	104.1
32X	8	1650	250.5-260.1	9.6	8.22	85.6	32P	12	1300	635.3-636.3	1.0	0.00	0.0
33P	8	1740	260.1-261.1	1.0	0.00	0.0	33X	12	1435	636.3-644.9	8.6	8.08	93.9
34X	8	1855	261.1-269.7	8.6	7.18	83.5	34X	12	1625	644.9-654.5	9.6	1.56	16.2
35X	8	2010	269.7-279.3	9.6	6.42	66.9	35X	12	1810	654.5-664.1	9.6	9.06	94.4
36X	8	2230	279.3-288.9	9.6	6.30	65.6	36P	12	1920	664.1-665.1	1.0	0.00	0.0
37X	8	2335	288.9-298.5	9.6	8.84	92.1	37X	12	2055	665.1-673.8	8.7	8.59	98.7
38X	9	0045	298.5-308.1	9.6	7.75	80.7	38X	12	2220	673.8-683.4	9.6	9.81	102.0
39X	9	0200	308.1-317.7	9.6	8.67	90.3	39X	12	2350	683.4-693.0	9.6	9.11	94.9
40P	9	0255	317.7-318.7	1.0	0.00	0.0	40P	13	0105	693.0-694.0	1.0	0.00	0.0
41X	9	0535	318.7-327.4	8.7	7.78	89.4	41X	13	0245	694.0-702.6	8.6	1.17	13.6
42X	9	0645	327.4-337.0	9.6	3.87	40.3	42X	13	0430	702.6-712.2	9.6	4.09	42.6
43X	9	0750	337.0-346.7	9.7	5.11	52.7	43X	13	0610	712.2-721.8	9.6	8.57	89.3
44X	9	1010	346.7-356.3	9.6	9.27	96.5	44P	13	0715	721.8-722.8	1.0	0.00	0.0
45X	9	1110	356.3-365.9	9.6	0.00	0.0	45X	13	0855	722.8-731.4	8.6	8.07	93.8
46X	9	1205	365.9-375.6	9.7	9.08	93.6	46X	13	1050	731.4-741.1	9.7	8.75	90.2
47X	9	1315	375.6-385.3	9.7	4.61	47.5	47X	13	1235	741.1-750.0	8.9	8.72	98.0
48X	9	1600	385.3-394.9	9.6	8.78	91.4							
49P	9	1655	394.9-395.9	1.0	0.64	64.0							
50X	9	1825	395.9-404.5	8.6	3.87	45.0							
51P	9	1920	404.5-405.5	1.0	0.47	47.0							
52X	9	2040	405.5-414.1	8.6	9.19	107.0							
53X	9	2310	414.1-423.7	9.6	0.03	0.3							
54X	10	0030	423.7-433.3	9.6	7.22	75.2							
55P	10	0130	433.3-434.3	1.0	0.50	50.0							
Coring totals				434.3	342.77	78.9					364.6	242.75	66.6

Notes: UTC = Universal Time Coordinated. An expanded version of this coring summary table that includes lengths and depths of sections, sampling comments, and locations of water-sampling temperature probe (WSTP) measurements is included on CD-ROM in the back pocket of this volume.

Hole 997B was then terminated, with the bit clearing the rotary table at ~0725 hr on 17 December.

Transit to Miami

The ship was under way for Miami, Florida, at 0815 hr on 17 December. Leg 164 officially ended with the first mooring line in the port of Miami at 0530 hr on 19 December.

LITHOSTRATIGRAPHY

Introduction

The 750-m sedimentary section recovered at Site 997 is a composite section of Holocene to upper Miocene sediments and sedimentary rocks recovered from Holes 997A and 997B (Fig. 3). Hole 997A was continuously cored to 433.3 mbsf, and a nearly complete Holocene to lower Pliocene section was recovered. Approximately 370 m of lower Pliocene to upper Miocene sediments was recovered in Hole 997B. Three lithostratigraphic units are recognized in Hole

997A on the basis of sediment composition, primarily variations in the nannofossil, diatom, and total carbonate contents. Color-reflectance measurements (VIS 400-700 nm) also exhibit changes corresponding to unit boundaries (Fig. 3). These units are quite similar to units previously recognized at Sites 994 and 995, and the extent of lithologic variability is very limited.

Unit I

Interval: 164-997A-1H-1, 0 cm, through 2H-3, 30 cm
Age: Holocene to late Pleistocene
Depth: 0-6.20 mbsf

Unit I consists of light greenish gray to light gray (5GY 6/1 to 7/1) foraminifer-bearing nannofossil-rich clay interbedded with gray to greenish gray (5Y 5/1 to 5GY 5/1) foraminifer-bearing nannofossil-rich clay and nannofossil-rich clay. The calcareous biogenic constituents consist of a mixture of pteropod shells (2%-10%), nannofossils (15%-35%) and foraminifers (5%-15%) (Fig. 4). Siliceous fossils are present as diatoms and sponge spicules. The base of Unit I is marked

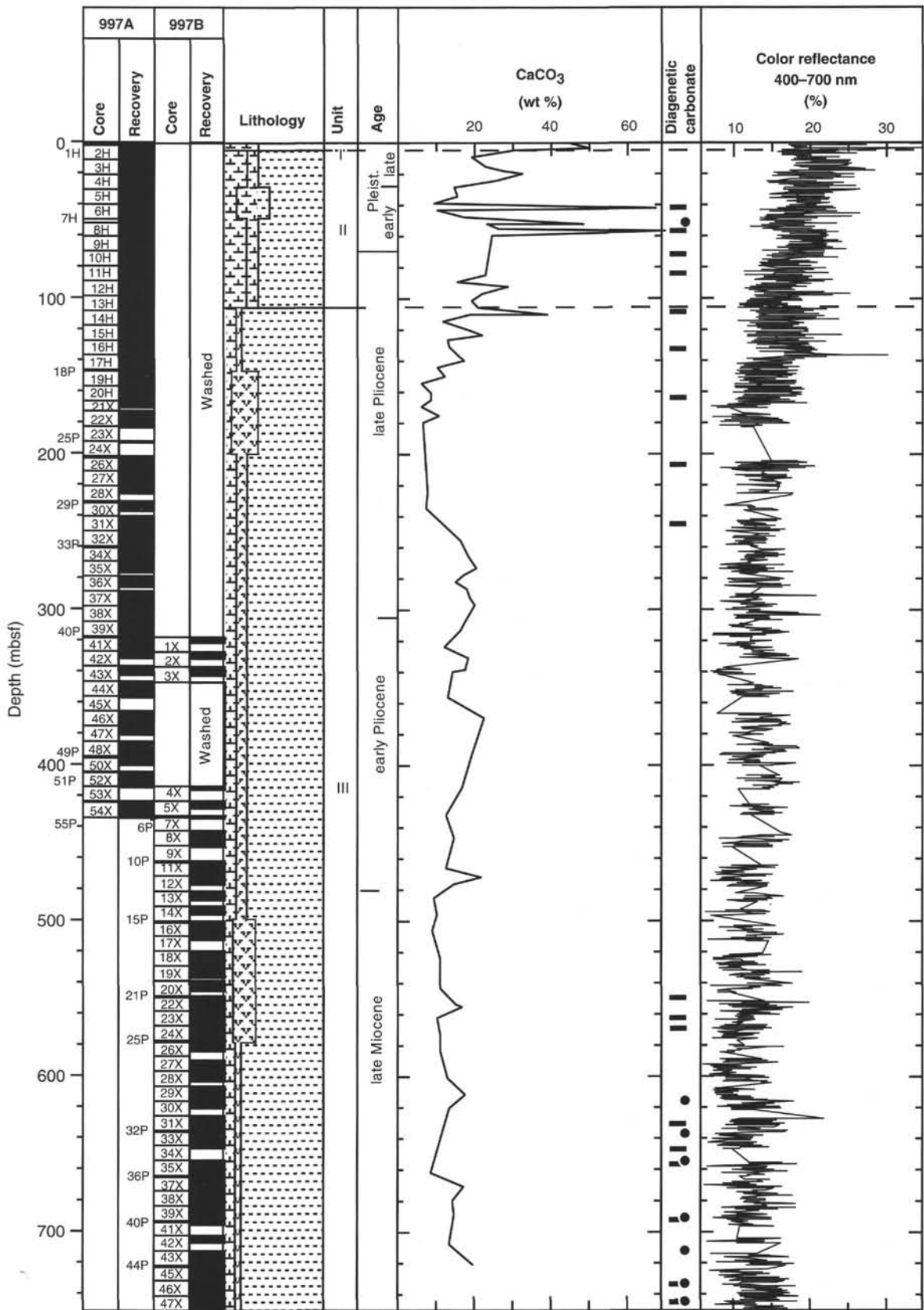


Figure 3. Composite stratigraphic section for Site 997 showing core recovery, a simplified summary of lithology, lithologic unit boundaries, and age. Also shown are total carbonate contents expressed as CaCO₃ weight percentage (see "Organic Geochemistry" section, this chapter), occurrences of diagenetic carbonates, and color reflectance of sediments across the visible spectrum (VIS 400-700 nm). In the diagenetic carbonates column, solid circles represent nodules; thick lines, concentrated beds. Lithologic symbols are explained in Figure 2 of the "Explanatory Notes" chapter (this volume).

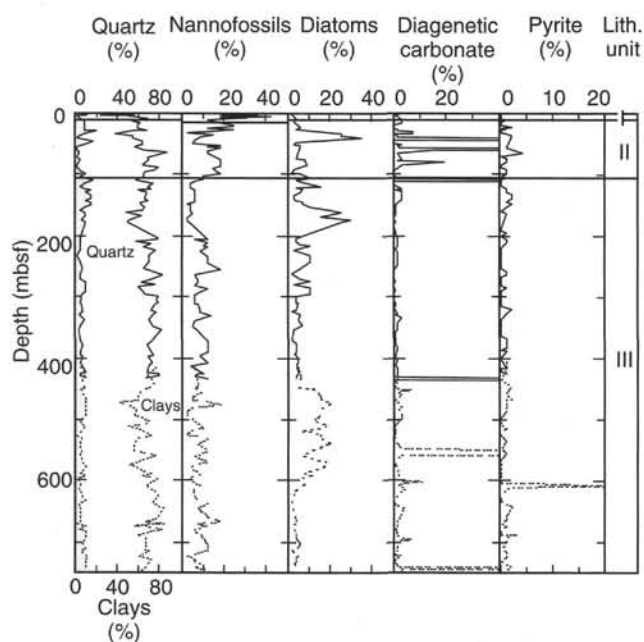


Figure 4. Downhole variation of the major sediment constituents, based on visual estimates from smear slides.

by the lowest occurrence of greenish gray (5G 4/2) foraminifer-bearing nannofossil-rich clay with interbedded glauconite-rich beds. Unit I is subdivided into two subunits on the basis of overall color and sediment composition.

Subunit IA

The uppermost 19 cm (interval 164-997A-1H, 0–19 cm; 0–0.19 mbsf) consists of grayish brown (10YR 5/2) bioturbated foraminifer-bearing nannofossil-rich clay. The lower boundary of Subunit IA is marked by a sharp color change to light greenish gray sediment of Subunit IB. Subunit IA in Hole 997A is equivalent to Subunit IA at Holes 994A, 994B, 994C, and 995A (see “Lithostratigraphy” sections in the “Site 994” and “Site 995” chapters, this volume).

Subunit IB

Subunit IB extends from 0.19 to 6.2 mbsf (interval 164-997A-1H-1, 19 cm, through 2H-3, 30 cm) and consists of alternating beds of two types of clay with slightly different colors, compositions, and degrees of bioturbation. Light greenish gray to light gray (5GY 7/1 to 5Y 6/1) foraminifer-bearing nannofossil-rich clay comprises 45- to 60-cm-thick beds. Intense bioturbation is common, and burrows often contain disseminated glauconite. Darker colored, mottled, gray to greenish gray (5Y 5/1 to 5GY 5/1) foraminifer-bearing nannofossil-rich clay and nannofossil-rich clay beds 80–100 cm thick are interbedded with the lighter colored clays. Total carbonate content, expressed as weight percentage CaCO_3 , ranges from 31 wt% in the darker beds to 50 wt% in the lighter beds (see Fig. 3 and “Organic Chemistry” section, this chapter).

Gray (7.5 YR 5/0) foraminifer-rich nannofossil-rich clay beds, as much as 3 cm thick, occur in intervals 164-997A-1H-2, 59–61 and 69–72 cm (2.09–2.11 and 2.19–2.22 mbsf, respectively). These beds also contain disseminated tests and fragments of pteropods. Several thin grayish green (5G 5/2) nannofossil-rich clay beds enriched in glauconite occur in the basal portion of Subunit IB (see Table 2).

Table 2. List of glauconite and foraminifer beds and representative occurrences of specific diagenetic minerals in Site 997 samples.

Unit	Lithology	Hole, core, section	Position (cm)	Depth (mbsf)	
I	Glauconite beds	997A-2H-1	89–90	3.79	
		997A-2H-1	111–112	4.01	
		997A-2H-1	119–120	4.09	
		997A-2H-2	117–119	5.57	
		997A-2H-2	130–131	5.70	
		997A-2H-3	10–12	6.00	
II	Foraminifer beds	997A-5H-1	105–106	32.05	
		997A-5H-1	114–121	32.24	
		997A-5H-1	125–127	32.31	
		997A-5H-2	110–112	34.05	
		997A-5H-3	108–109	35.53	
		997A-7H-1	125–130	54.65	
	Dolomite beds	997A-12H-6	49–54	88.82	
		997A-5H-CC	18–21	40.85	
		997A-10H-3	139–145	75.19	
	Dolomite nodule Pyrite nodules	997A-11H-5	81–82	87.21	
		997A-8H-3	14–18	56.04	
		997A-8H-1	34–35	53.24	
		997A-8H-1	75–76	53.69	
		997A-8H-1	79–80	53.69	
		997A-8H-1	108–109	53.98	
III	Foraminifer beds	997A-9H-4	119–120	54.09	
		997A-9H-4	84–85	66.74	
		997A-9H-6	39–40	69.29	
		997A-15H-3	100–127	122.40	
		997A-37X-1	31–37	289.20	
		997B-12X-3	113–114	473.11	
		Dolomite bed	997A-13X-8	67–74	108.53
			997A-16H-6	61–66	135.81
		Siderite beds	997A-26X-2	50	204.50
			997A-26X-2	58	205.48
			997A-26X-2	62	205.52
			997A-31X-2	111	638.08
997B-22X-1	120		549.92		
997B-22X-1	125		549.95		
997B-23X-3	59		561.99		
997B-23X-3	120		562.60		
997B-23X-4	21		563.49		
997B-31X-4	39		630.52		
997B-31X-4	43		630.56		
997B-31X-4	49		630.62		
997B-31X-4	59		630.72		
997B-35X-4	17		657.94		
997B-35X-4	29		658.06		
997B-35X-4	37		658.14		
997B-35X-4	46		658.23		
997B-35X-4	60		658.37		
997B-35X-4	63		658.40		
997B-35X-4	70		658.47		
997B-35X-4	87		658.64		
997B-35X-5	10		658.80		
997B-35X-5	26		659.12		
997B-35X-5	31		659.49		
997B-35X-5	40		659.95		
997B-35X-5	54		660.55		
997B-35X-5	79		661.40		
997B-35X-5	101		662.47		
997B-35X-5	118		663.71		
997B-39X-6	73		691.63		
997B-39X-6	141	692.31			
997B-39X-6	144	692.33			
997B-46X-2	127	733.01			
997B-47X-2	45	743.05			
Siderite nodules	997B-29X-4	20	611.20		
	997B-29X-4	23	611.23		
	997B-33X-2	12	637.09		
	997B-33X-2	33	637.30		
	997B-33X-2	49	637.46		
	997B-35X-3	89	657.16		
	997B-39X-6	90	691.80		
	997B-43X-1	117	713.37		
	997B-46X-3	120	734.44		
	997B-47X-2	63	743.22		
	997B-47X-2	80	743.39		
	997B-47X-2	104	743.63		
997B-47X-2	110	743.69			
997B-47X-2	116	743.75			
997B-46X-4	10	734.84			
997B-46X-4	106	735.80			
997B-47X-3	15	744.25			

Unit II

Interval: 164-997A-2H-3, 30 cm, through 13H-7, 35 cm
 Age: late Pleistocene to late Pliocene
 Depth: 6.20–107.83 mbsf

The top of Unit II is marked by a notable decrease in nannofossil abundance (generally less than 20%) and by the appearance of diatoms. Total carbonate content decreases from >30 wt% in Unit I to <30 wt% in Unit II, except in the diagenetic carbonate beds (Fig. 3 and "Organic Geochemistry" section, this chapter). Color-reflectance values also change at the Unit I/Unit II boundary (Fig. 3).

The sediment of Unit II consists of intensely burrowed light greenish gray to gray (5GY 6/1 to 5Y 6/1) nannofossil-rich clay with varying amounts (less than 10%) of foraminifers, interbedded with bioturbated greenish gray (5GY 5/1 to 5Y 5/1) nannofossil-rich clay and nannofossil-bearing clay. Beds are decimeters to meters in thickness. Sediments in interval 164-997A-5H-1, 0 cm, to 6H-4, 150 cm (31.4–46.9 mbsf), are enriched in diatoms (35% in maximum) and consist of interbedded, decimeter- to meter-thick greenish gray to bluish gray (5BG 6/1 to 5B 6/1 and 5GY 5/1) nannofossil-rich diatom-rich clay, and greenish gray to gray (5GY 5/1 to 5Y 5/1) nannofossil-bearing diatom-rich clay. Nannofossil abundances reach 20% but drop to less than 10% in the dolomite-rich sediments and in the diatom-rich interval. Except for this diatom-rich interval, diatom abundances remain below 10%. Siliceous sponge spicules are generally present as a minor component (1% on average) of the sediments. Silt-sized carbonate fragments, mostly consisting of shell debris, make up a few percent of the bulk sediment. Bioturbation varies from slight to moderate throughout this unit.

Seven beds of moderately burrowed greenish gray (5BG 6/1 to 5GY 5/1) foraminifer-rich nannofossil-rich clay, ranging in thickness from 1 to 7 cm, occur as listed in Table 2 and are recognized as distinct lighter colored beds with sharp bases. In contrast to equivalent stratigraphic levels at Sites 994 and 995, neither graded bedding nor reddish colored sediments was observed in these beds at this site. Centimeter-sized pyrite nodules and pyritized burrows are rare (see Table 2). Disseminated sulfides are common below 78.70 mbsf. The highest carbonate contents (as much as 70 wt%) occur in the dolomite beds (representative beds listed in Table 2). Irregularly shaped gray (5Y 6/1) dolomite nodules, as much as 2 cm in diameter, occur in interval 164-997A-8H-3, 14–18 cm (56.04–56.08 mbsf).

The sediments in intervals 164-997A-5H-3, 115 cm, to 5H-6, 150 cm (36.7–41.2 mbsf), 6H-7, 0–73 cm (49.9–50.63 mbsf), and 10H-5, 45–65 cm (77.2–77.4 mbsf), exhibit mousse-like fabric and have been homogenized by drilling. Numerous voids and horizontal cracks appear to have been caused by degassing disturbance in the cores recovered from below 30.9 mbsf (Sections 164-997A-4H-7 and below). The bottom boundary of Unit II (164-997A-13H-7, 35 cm; 107.25 mbsf) is defined as the base of the last occurrence of a lighter colored, mottled nannofossil-bearing clay bed.

Unit III

Intervals: 164-997A-13H-7, 35 cm, through 55P-1, 40 cm; 164-997B-1X-1, 0 cm, through 47X-CC, 18 cm
 Age: late Pliocene to late Miocene
 Depth: 107.83–434.3 mbsf (Hole 997A) and 318.5–750.0 mbsf (Hole 997B)

The upper boundary of Unit III is marked by a decrease in total carbonate content to values <20 wt% (see Fig. 3 and "Organic Geochemistry" section, this chapter). Decreases in nannofossil abundance to <10% also occur across this boundary. Color-reflectance values show a small but systematic shift at this boundary, although the values tend to fluctuate in the upper part of Unit III (Fig. 3).

Unit III is a thick succession of homogeneous dark greenish gray to greenish gray (5GY 4/1 to 5GY 5/1), diatom-bearing nannofossil-bearing clay and claystone and nannofossil-bearing diatom-rich clay and claystone. Total carbonate content ranges from 8 to 24 wt% (Fig. 3; see "Organic Geochemistry" section, this chapter) except for the diagenetic carbonate beds in which the content is as much as 40 wt% (e.g., interval 164-997A-13H-8, 72–73 cm). Nannofossils and diatoms are the major biogenic components with minor associations of sponge spicules, carbonate fragments including shell debris, and foraminifers. The degree of bioturbation fluctuates from slight to moderate or intense across 1.5- to 3-m intervals throughout this unit.

Sediments in the intervals between 146.9 and 183.2 mbsf and between 452.6 and 587.2 mbsf consist of nannofossil-bearing diatom-rich clay and diatom-rich clay with diatom contents as high as 30%. Total carbonate content in these intervals ranges from 8 to 18 wt%, and nannofossil abundances generally fall below 10%. In interval 164-997A-46X-3, 0–62 cm (368.9–369.52 mbsf), dark greenish gray (5GY 4/1) nannofossil-bearing clay containing very dark gray (5Y 3/1) thin lamina and beds is marked by intense bioturbation with burrows containing disseminated foraminifer tests. Some of these laminae and beds exhibit truncated, gently dipping stratification, resembling cross-lamination.

Additional thin parallel laminae occur in intervals 164-997B-39X-2 through 39X-6 (684.9–692.4 mbsf), 43X-2 through 43X-6 (713.7–721.5 mbsf), and 45X-4, 4 cm, through 46X-5, 150 cm (722.84–730.16 mbsf) (Fig. 5). These intervals consist of repetitions of millimeter-thick, very dark gray (5Y 3/1) and light greenish gray (5GY 6/1) laminae. The light-colored laminae tend to be slightly enriched in authigenic carbonate silt-sized crystals (estimated to be 5% by smear-slide observation) but contain less abundant detrital constituents (e.g., quartz and clays) than the darker laminae.

Foraminifers are concentrated in greenish gray (5GY 6/1) to olive gray (5Y 4/2) possibly winnowed beds in intervals from 122.4 to 122.67 mbsf, from 289.21 to 289.26 mbsf, and from 473.11 to 473.12 mbsf (Table 2). These winnowed beds are probably similar in origin to the foraminifer-rich beds found in Subunit IB and Unit II. Disseminated foraminifers are common in the olive (5Y 4/2 to 5/3) foraminifer-bearing silty clay that fills the burrows of the intensely bioturbated intervals. White spherical patches of sponge spicules, 2–9 mm in size, are rare to common in Sections 164-997A-14H-4 through 20H-7 (112.2–166.7 mbsf), whereas similar spherical patches with concentrations of detrital quartz silt are rare in Sections 164-997A-19H-3 through 19H-7 (150.13–157.63 mbsf).

Light greenish gray (5G 7/1) to pale olive (5Y 6/3) clay-rich carbonate-rich beds, laminae, and nodules occur in some intervals of Unit III (e.g., 108.53–205.52 and 549.92–744.25 mbsf; see Table 2). Nodules are generally lens-shaped and as much as 1 cm in diameter (Fig. 6).

The sediment starts to exhibit a distinct fissile structure in Section 164-997A-43X-3 (338.94 mbsf) and becomes more fissile and increasingly lithified downhole. High-angle to vertical fractures first appear in Section 164-997A-22X-2 (174.18 mbsf) and are rare to common to the base of Hole 997A and throughout Hole 997B.

Sediment Composition Based on Smear-Slide and XRD Analyses

The dominant mineral components of Unit I are clay minerals, calcite, and quartz. Feldspars, aragonite, and dolomite are minor components (Table 3; Fig. 7). The clay-sized fraction is made up mostly of clay minerals and nannofossils. The silt-sized fraction is dominated by quartz and feldspars; the estimated quartz abundance based on XRD data never exceeds 10 wt% (Fig. 7). Disseminated dolomite rhombs (15–30 μ m in diameter) make up a few percent of the bulk mineralogy (Fig. 7). Glauconite occurs in trace amounts, but it is locally more abundant within burrows.

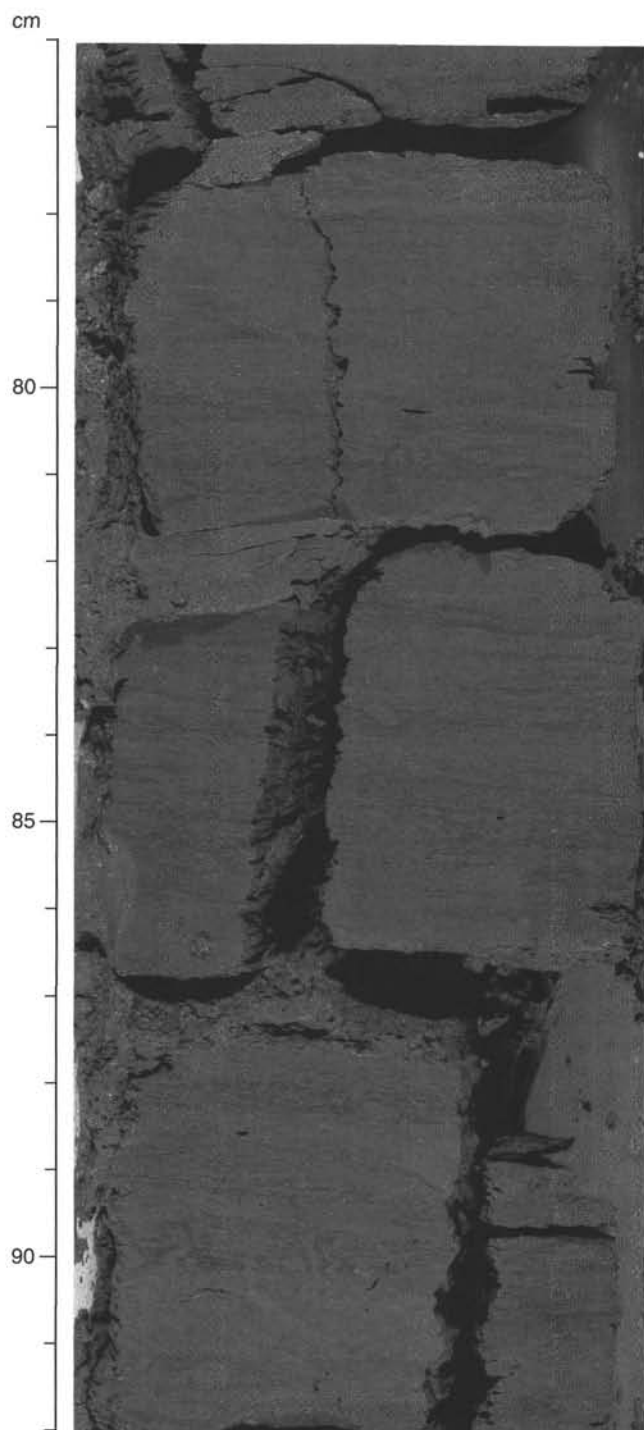


Figure 5. Intensely bioturbated dark greenish gray (5GY 4/1) claystone with burrows filled with lighter greenish gray to gray (5GY 4/1 to 5Y 4/1) sediment. Some of the original light-dark parallel laminations are preserved (interval 164-997B-45X-5, 76–92 cm; 729.42–729.58 mbsf).

In Unit II, clay minerals, calcite, and quartz also are the dominant mineral components (Fig. 7; Table 3). Feldspars, dolomite, and pyrite are minor components, although dolomite becomes dominant in the nodules and thin layers as listed in Table 2. The clay-sized fraction is dominated by clay minerals and nannofossils but also includes quartz and feldspars. As in Unit I, quartz and feldspars mostly occur in the silt-sized fraction; the quartz abundances are estimated to range from

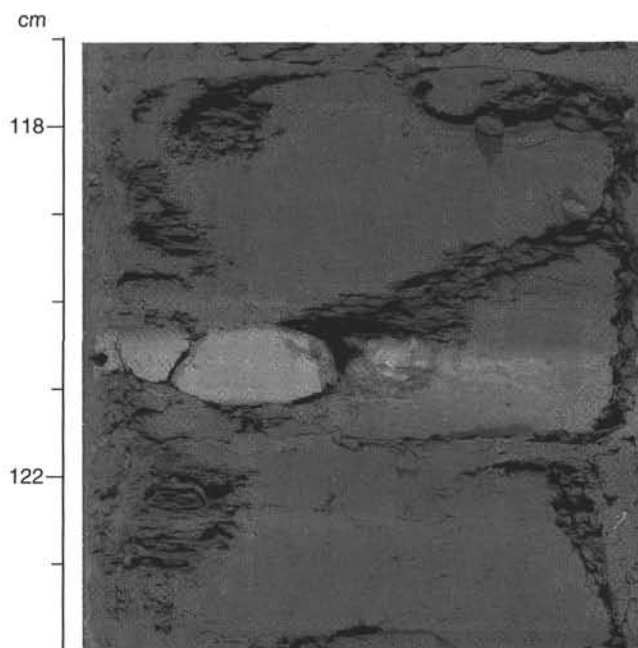


Figure 6. Light gray carbonate nodule with laterally decreasing carbonate cementation. The host sediment is weakly bioturbated greenish gray (5GY 4/1) nannofossil-bearing claystone (interval 164-997B-46X-3, 117–124 cm; 734.41–734.48 mbsf).

6 to 14 wt% and generally increase downhole to the base of Unit II. The maximum abundance of feldspars occurs between the top of Unit II and 47.40 mbsf; feldspars decrease downhole to the base of Unit II. Dolomite rhombs, 5–15 μm in diameter, are widely disseminated but are only from 1 to 3 wt% of the bulk sediment composition. According to the d-spacing of the (104) and (116) diffraction peaks (2.897–2.899 \AA and 1.792–1.796 \AA , respectively), the dolomite is a ferroan dolomite. A downward increase in the d-spacing of the (104) peak from 2.888 to 2.904 \AA probably indicates a general increase in iron, rather than in calcium content, of the dolomite with depth (Table 3). In the dolomite-rich intervals, micrometer-sized particles are associated with larger subhedral crystals of 10–20 μm in length. Pyrite first occurs in Sample 164-997A-2H-5, 50 cm (4.9 mbsf), as an infilling of foraminifer chambers and as isolated framboids. Pyrite is only a minor component (1%–3%, Fig. 4) of Unit II.

In Unit III, clay minerals, calcite, and quartz represent major mineral components, whereas dolomite, siderite, pyrite, and feldspars occur in minor amounts (Figs. 3, 4; Table 3). Clay minerals and nannofossils make up most of the clay-sized fraction. Quartz abundances average 13 wt% of the bulk sediment based on XRD analyses. Diagenetic carbonate rhombs, similar in shape to those observed in Unit II, are widely disseminated throughout the sediment; their abundances range from 1% to 10%, according to smear-slide estimates (Fig. 4). The XRD analyses indicate that the diagenetic carbonates are composed of dolomite and siderite; the downhole decrease in dolomite content to less than 1 wt% below ~110 mbsf is generally compensated by the increase in siderite (Fig. 7). Variable dolomite composition is exhibited by shifts in the d-spacing of the (104) peak, which ranges from 2.884 to 2.905 \AA ; there is, however, no significant downhole trend in this d-space variation (Table 3). In the dolomite-rich bed from interval 164-997A-13H-8, 68–74 cm (108.14–108.20 mbsf), the d-spacing values of the (104) and (116) peaks (2.896 and 1.796 \AA respectively) are characteristic of ferroan dolomite. Siderite-rich layers and nodules are rare downhole to ~600 m. Below ~600 m, siderite becomes more common and is concentrated in individual millimeter-

Table 3. Main diffraction peak areas, d-values, and weight percentage proportions for minerals identified in samples from Site 997.

Core, section, interval (cm)	Depth (mbsf)	Quartz	Clays	Calcite	Calcite	Dolomite	Dolomite	Feldspars	Aragonite	Pyrite	Siderite	Quartz*	Calcite*	Dolomite*
		(101) peak area	4.4–4.6 Å peak area	(104) d-value (Å)	(104) peak area	(104) d-value (Å)	(104) peak area	3.26–3.18 Å peak area	(111) peak area	(311) peak area	(104) peak area			
164-997A-														
1H-1, 35–36	0.35	8,936	2,461	3,034	15,669	2.89	1,400	3,823	3,008			7	34	1
2H-1, 71–72	3.61	6,528	2,156	3,036	22,762	2.887	2,527	3,403	2,022			5	62	3
2H-2, 50–51	4.90	9,765	2,647	3,036	17,111	2.889	1,257	3,752	476			7	39	1
2H-5, 50–51	9.40	10,476	2,561	3,037	10,807	2.892	1,841	6,477		945		8	20	2
3H-2, 49–50	14.39	10,738	2,351	3,036	11,233	2.889	3,345	6,610	501	1,283		8	21	3
3H-4, 63–64	17.53	13,581	2,403	3,034	12,161	2.888	5,009	10,071		880		10	23	5
3H-5, 49–50	18.89	9,973	2,665	3,035	14,570	2.891	852	4,387	1,459	1,206		7	31	1
4H-2, 49–50	23.89	12,824	2,413	3,035	12,993	2.894	2,339	3,976	633	1,163		9	26	2
4H-5, 49–50	28.39	13,030	2,504	3,036	7,922	2.893	2,167	7,243		899		10	13	2
5H-2, 49–50	33.39	10,408	2,192	3,034	10,000	2.896	885	7,771	502	1,255		8	18	1

Notes: * = percentages (wt%) for quartz, calcite, and dolomite are calculated using the calibration curves described in the "Lithostratigraphy" section in the "Explanatory Notes" chapter (this volume).

Only part of this table is produced here. The entire table appears on the CD-ROM (back pocket).

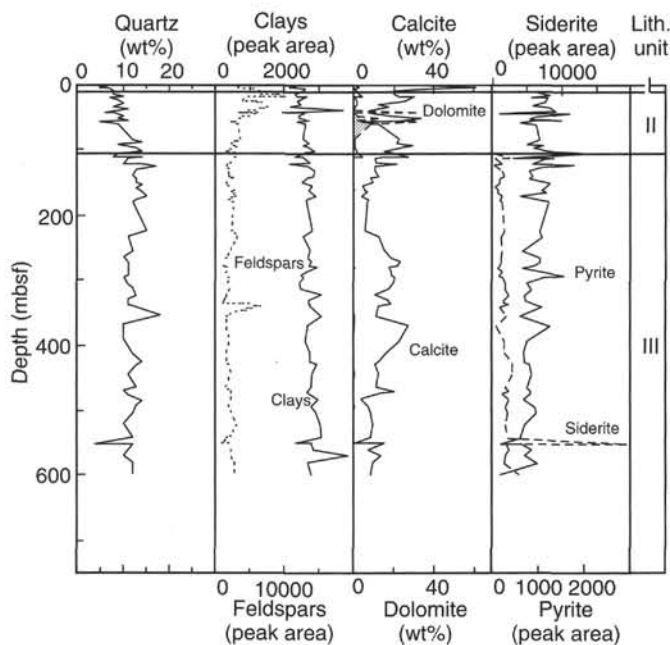


Figure 7. Downhole variation of the major mineral constituents of the sediments, based on XRD analysis. Quartz, calcite, and dolomite contents are expressed in weight percentage (see "Explanatory Notes" chapter, this volume). The relative abundances of clays, feldspars, pyrite, and siderite are given as integrated peak areas.

thick layers and in millimeter- to centimeter-sized nodules (Table 2). Siderite crystals display their typical rhomb-shaped morphology and range in size from 10 to 30 μm . On the basis of smear-slide estimates, pyrite makes up ~1% to 3% of the bulk sediment. The XRD analyses confirm that pyrite concentrations are low and tend to decrease downhole.

Discussion

Site 997 is located on the crest of the Blake Ridge 9.6 and 6.7 km from Sites 994 and 995, respectively (see "Background and Objectives" section, this chapter). As expected, sediments and lithologic units at this site are very similar to those of Sites 994 and 995 (see "Lithostratigraphy" sections, "Site 994" and "Site 995" chapters, this volume). Deposition is dominated by hemipelagic accumulation of biogenic and terrigenous sediments. At Sites 994 and 995, long-

distance transport of sediment is clearly indicated by the reddish gray (5YR 6/1) nanofossil-rich clays of Unit II that were possibly derived from Carboniferous red beds in eastern Canada and transported southward by the Western Boundary Undercurrent (WBUC) (Heezen et al., 1966; Needham et al., 1969). These reddish sediments are not observed at Site 997. However, the greenish gray foraminifer-rich nanofossil-rich clay beds in Units II and III might be their diluted equivalents (see "Lithostratigraphy" sections, "Site 994" and "Site 995" chapters, this volume).

Contourite deposition in the Miocene (See "Biostratigraphy" section, this chapter) is evidenced by a foraminifer-rich graded bed (interval 164-997B-39X-6, 73–74 cm; 722.23–723.24 mbsf) in Unit III. This is the deepest occurrence of such a graded bed at any of the three sites. Intervals of thin parallel lamination in the clays and claystones of Unit III (368.9–369.5, 684.9–692.4, 713.7–721.5, and 722.8–730.2 mbsf) also suggest contour-current activity. If these sedimentary features in Unit III originated from WBUC activity, they are the only evidence of contour-current activity during the late Miocene observed in the Leg 164 holes.

High sedimentation rates of 200–340 m/m.y. (see "Biostratigraphy" sections of the "Site 994," "Site 995," and "Site 997" chapters, this volume) are always associated with moderate concentrations of organic carbon (1.2%–1.8%; see "Organic Geochemistry" sections of the "Site 994," "Site 995," and "Site 997" chapters, this volume). Two intervals of diatom-rich sediments in Unit III from all three sites (160–232 and 430–660 mbsf at Site 994, 131.9–252.3 and 464.2–656.0 mbsf at Site 995, and 146.9–183.2 and 452.6–587 mbsf at Site 997) occur at depths corresponding to ages between 5.8 and 5.0 Ma and between 3.0 and 2.6 Ma within zones of higher sedimentation rates (see "Biostratigraphy" sections of the "Site 994," "Site 995," and "Site 997" chapters, this volume). Increased sedimentation rates could be explained by either elevated in situ diatom productivity and/or enhanced deposition of reworked, penecontemporaneous diatomaceous sediments by the WBUC in this region of the Atlantic.

GAS HYDRATE

One large, solid piece of gas hydrate was recovered from ~331 mbsf at Site 997. However, the presence of dispersed gas hydrate was inferred over a zone that extends from ~180 to ~450 mbsf.

Initial Core Inspection

All cores were inspected on the catwalk for indications of gas hydrate, such as the presence of white nodules, fizzing materials, or unusually cold spots. The following cores are the only cores in which

the presence of gas hydrate was suspected on the basis of these initial inspections.

Hole 997A

Sections 164-997A-27X-1 and 2 (231.30–234.30 mbsf) were determined to be cold upon arrival. After initial temperature-probe measurements as low as 0.7°C were made on the catwalk, Sections 164-997A-27X-1 and 2 were quickly split open. The surface of the core was noted to be firm and dry. A transect of temperature measurements made along the freshly cut surfaces showed one distinctly cooler zone that extended from the lower 30 cm of Section 164-997A-27X-1 to the upper 30 cm of Section 2 (~232.50–233.10 mbsf). The temperature variations were concentrated in a ~40-cm-thick zone (Fig. 8). However, neither bubbling nor gas hydrate was observed.

Section 164-997A-32X-4 (255.00–256.50 mbsf) was determined to be cool. The lowest temperature reading taken on the catwalk was 5.3°C at 70 cm in Section 164-997A-32X-4, whose liner was immediately opened without splitting the core itself. The exterior sections were mousse-like, but the core material itself was firm and lithologically typical of the surrounding section. No bubbling or gas hydrate was observed. A transect of temperature measurements was made along the core (Fig. 8). The same spot that had the lowest reading on the catwalk only produced a 7.6°C reading along this temperature transect.

Massive gas hydrate was recovered from Section 164-997A-42X-3 at 330.03–331.17 mbsf. Core 164-997A-42X was generally cold to the touch upon core recovery. A white and actively bubbling area was initially observed in a soupy sediment layer between the core liner and the sediment at the top of Section 164-997A-42X-3. The upper ~20 cm of this section was cut off. About 10–15 angular fragments of white, actively fizzing gas hydrate that were 3–10 cm³ in volume and floating in soupy sediments were poured out from this section of the liner. The next interval of Section 164-997A-42X-3 (~20–55 cm) also was cut off, and the core liner was split so that the unsplit whole-round sediments could be inspected. Beneath a veneer of soupy sediments lay solid, white gas hydrate nodules that were 4–6 cm in diameter (Fig. 9). The massive gas hydrate-bearing horizon in Section 164-997A-42X-3 (~20–55 cm) consisted of three pieces that were 5, 7, and 13–15 cm long from top to bottom (see Fig. 2 in Section 2, this volume). Because of disturbance by drilling and/or hydrate dissociation, the boundary between the gas hydrate and host sediments was not preserved, and there were internal gaps (~1–2 cm wide) separating the major pieces of hydrate. The top surface of the upper piece was inclined to the core liner by ~20°. The middle sample was partly coated by thin (~1 mm), transparent shiny layers of water-ice. The next ~20 cm contained several rectangular plates (~4 cm × 3 cm and a few millimeters thick) of gas hydrate that are similar to the vein-filling hydrate observed at Site 996. The orientation of these plates of gas hydrate appeared to be random and indicated that the plates were in disturbed sediments. The rest of Section 164-997A-42X-3 was a void. The sediments in the cored sections above (164-997A-41X and 42X-1) and below (164-997A-43X) the gas hydrate-bearing Core 164-997A-42X were typical of lithologic Unit III (see “Lithostratigraphy” section, this chapter).

Hole 997B

In Hole 997B, three spot cores were taken that corresponded with the zone where solid gas hydrate was detected in Section 164-997A-42X-3. When the core catchers for Cores 164-997B-1X and 2X were being taken off, water sprayed out of the core barrel for ~20 s. Core 164-997B-1X showed no indications of gas hydrate. Section 164-997B-2X-2 (from the interval between 328.1 and 337.7 mbsf) had a temperature of –0.8°C on the premarked sample for the interstitial-water analysis. The core liner was split open, but gas hydrate was not observed. The liner of Section 164-997B-2X-4 (directly below the

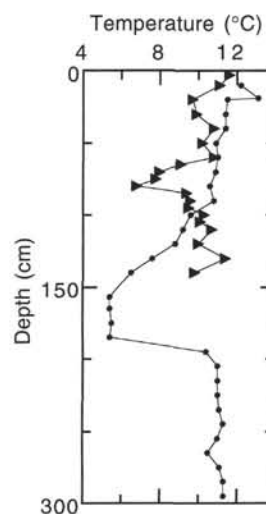


Figure 8. Temperatures along Sections 164-997A-27X-1 and 2 (solid circles) and 32X-4 (solid triangles) soon after they were split to examine for the possible presence of gas hydrate.

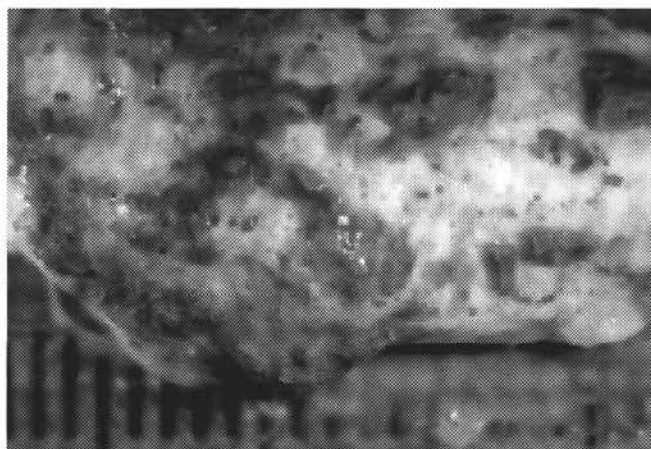


Figure 9. Photograph of massive gas hydrate 4–6 cm in diameter and 15 cm long from Section 164-997A-42X-3.

interstitial-water sample) also was opened without splitting the core itself. No gas hydrate was observed in this section either.

Anomalously low temperature sections were observed in Sections 164-997B-11X-1 (462.2–463.7 mbsf) and 12X-2 (472.61–474.11 mbsf); the temperature readings were –0.8° and –2.1°C, respectively. Both cores were immediately opened for closer inspection but were not observed to contain gas hydrate. Section 164-997B-12X-2 (472.61–474.11 mbsf) was, however, observed to include transparent shiny crystals (water-ice) infilling freshly broken foraminifer tests. These crystals were gone within a few minutes, but no bubbling was observed, suggesting that the shiny crystals were not gas hydrate but water-ice. Analyses of the downhole-logging data suggest that Section 164-997B-12X-2 (472.61–474.11 mbsf) was from a stratigraphic interval containing free gas (see “Downhole Logging” section, this chapter). It is thought that adiabatic gas expansion cooled the core during recovery and froze the interstitial pore waters in Section 164-997B-12X-2.

Composition of Gas Hydrate

A 10-cm³ broken fragment from Section 164-997A-42X-3 was placed into a gas hydrate dissociation chamber to analyze the gas and

water after decomposition (see "Explanatory Notes" chapter, this volume). The ratio of evolved gas volume to water volume was 138.7. The chloride concentration (187 mM) of the water collected from the dissociation chamber indicates that the sample was a mixture of ~30% pore water with 70% freshwater derived from gas hydrate dissociation. The evolved gas was 98.43% CH₄ and 1.57% CO₂. These data indicate structure I gas hydrate similar to that recovered from Sites 994 and 996. Ethane and propane were at 196 and 3.8 ppmv levels, so the C₁/C₂ ratio was 4936, which falls within the range of the C₁/C₂ ratios of headspace gas (1880) and free gas (6748) taken from the same core (see "Organic Geochemistry" section, this chapter).

Catwalk Temperature Measurements

Extensive through-the-liner temperature measurements on almost all cores from Holes 997A and 997B were conducted in an attempt to detect gas hydrate and to establish the thermal signature of recently recovered sediments. Data acquisition through Core 164-997A-16H was with 30 individual temperature probes that were monitored with a computer (see "Gas Hydrate Sampling" section, "Explanatory Notes" chapter, and Frontispiece, this volume). Upon recovery of these cores, small holes were drilled through core liner at 30-cm intervals, and thin temperature probes were inserted into the sediment cores on the catwalk. However, electronic failure in the data logger occurred after Core 164-997A-16H. Subsequently, temperature measurements were made with a high-precision handheld digital thermometer. Voids were consciously avoided. A total of 1326 measurements were made on 42 cores from Hole 997A and 33 cores from Hole 997B (Table 4; Fig. 10A).

Core temperatures are typically lower at the top and rise toward the bottom of an individual core (Fig. 10B). For example, the measured catwalk temperatures of Core 164-997A-26X were ~8°C at the top and 13°C at the bottom, which is typical of cores shallower than 175 mbsf. This pattern is unexplained but may involve the thermal expansion of the gases that evolved within the cores, especially if gases preferentially exit through the top of the core during recovery.

Spiky low-temperature anomalies were also observed within cores between ~206 mbsf (Core 164-997A-26X) and ~510 mbsf (Core 164-997B-16X) (Fig. 10C). For example, Cores 164-997A-26X, 27X, and 28X also contain several localized low-temperature anomalies, with minimum temperatures of ~1°C in Sections 164-997A-27X-2 and 3. Spiky low-temperature anomalies are concentrated in individual beds of 0.1 m to 4.0 m in thickness. The low core temperature anomalies within the zone of gas hydrate occurrence may either indicate areas where gas hydrate had recently decomposed or areas where the effects of adiabatic gas expansion were concentrated during core recovery.

Distinct low-temperature anomalies (0.5°–2.0°C) also were observed in Cores 164-997B-11X (463–472 mbsf), 12X (472–482 mbsf), 13X (482–491 mbsf), and 16X (501–510 mbsf). Although these cores were collected during the passage of a cold front and the exterior temperatures dipped from 20° to 12°C for a few hours, the origin of localized low-temperature anomalies cannot be attributed to the weather. The interstitial-water chloride concentrations, downhole-logging data, and VSP acoustic measurements indicate that the lower limit of gas hydrate is at or above 460 mbsf. However, the downhole logs and VSP and PCS data show that this zone contains free gas. Thus, these low-temperature anomalies are solely attributed to the adiabatic expansion of gas.

Gas-Collection Chambers

The volumes of gas that evolved from sediments while they warmed to room temperature were measured by placing 1.5-m whole-core sections into sealed chambers, referred to as gas-collection chambers (see "Gas Hydrate Sampling" section, "Explanatory Notes" chapter, this volume). Table 5 gives the total measured

Table 4. Average and minimum temperatures of cores from Holes 997A and 997B as measured on the catwalk immediately after recovery.

Core	Temperature		
	Maximum (°C)	Minimum (°C)	Average (°C)
164-997A-			
2H	14.9	13.9	14.2
3H	12.8	9.9	11.4
4H	12.7	10.2	11.3
5H	12.9	10.9	11.7
6H	13.9	12.2	12.7
7H	12.1	9.9	11.3
8H	12.5	9.8	11.0
9H	16.5	13.0	13.7
10H	15.0	13.2	14.0
11H	12.8	10.3	11.9
12H	11.7	11.6	12.1
13H	15.0	13.2	13.9
14H	17.0	14.9	15.9
15H	15.9	14.4	15.0
16H	14.3	12.5	13.6
17H	17.9	13.2	15.3
19H	15.5	14.1	14.8
20H	13.8	13.4	13.8
21X	17.2	13.8	15.0
22X	13.0	11.3	12.0
26X	7.7	6.4	9.4
27X	11.4	0.7	8.8
28X	12.3	6.2	10.5
30X	12.3	2.5	9.6
31X	12.3	4.5	9.5
32X	16.8	6.0	10.1
34X	9.4	8.1	10.7
35X	13.1	4.9	9.2
36X	14.1	4.4	11.9
37X	13.3	8.2	11.2
38X	14.0	7.6	11.6
39X	12.8	5.8	10.1
41X	14.7	5.5	10.5
43X	14.2	10.0	12.3
44X	13.2	4.7	10.6
46X	14.5	1.0	11.6
47X	13.2	6.6	11.2
48X	15.6	4.4	11.3
50X	16.7	10.2	13.0
52X	13.6	4.8	10.1
54X	15.0	1.0	11.9
164-997B-			
1X	11.6	7.9	10.0
2X	11.3	-1.0	10.0
3X	9.7	5.8	8.4
4X	9.6	5.9	7.6
5X	11.3	5.5	8.6
8X	11.6	10.5	11.1
11X	7.7	-0.8	4.4
12X	8.5	-2.1	4.9
13X	10.0	4.7	8.6
14X	11.5	8.8	9.9
16X	10.0	0.3	6.6
17X	10.1	6.8	8.2
18X	13.9	6.5	10.2
19X	11.8	6.9	9.7
20X	12.2	9.7	11.4
22X	14.7	8.4	11.7
23X	13.3	8.9	12.0
24X	12.4	9.7	11.3
26X	12.4	9.7	10.9
27X	12.6	7.1	10.9
28X	13.4	11.4	10.9
29X	13.2	9.1	11.8
30X	13.2	8.6	10.8
31X	12.7	10.2	11.3
35X	16.6	11.0	14.0
37X	15.0	13.3	12.5
38X	14.7	11.0	12.9
39X	13.8	9.6	12.3
42X	13.7	8.7	11.2
43X	15.1	11.4	13.5
45X	15.0	10.6	13.2
46X	16.4	14.6	15.8
47X	15.3	11.6	14.0

volume of gas evolved from individual core sections and the calculated volumes of gas that were evolved per liter of interstitial water based on measured porosities (see "Physical Properties" section, this chapter).

Measurable volumes of evolved gas first occur in core sections that come from below the base of the sulfate reduction zone (~23

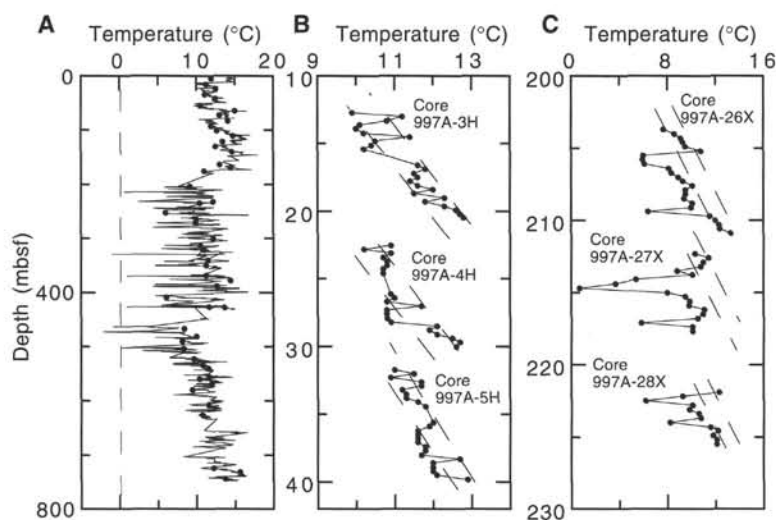


Figure 10. A. Temperatures of sediments shortly after they were recovered from Site 997 are shown vs. the recovery depth. Solid line = temperatures measured through the liner on the catwalk. Solid circles = initial temperatures when the core sections were placed into gas-collection chambers. B. Temperature variations of Cores 164-997A-3H, 4H, and 5H, ranging in depth from 12.4 to 40.9 mbsf. Core temperatures measured on the catwalk are usually lower in the core top than the core bottom by $\sim 2^{\circ}$ – 3° C. Broken lines = general temperature profiles. C. Temperature variations of Cores 164-997A-26X, 27X, and 28X (203.4–231.3 mbsf) showing anomalously low temperatures that deviate from the general temperature profile.

Table 5. Volumes of gas collected from 1.5-m whole-core sections as they warmed to room temperature inside the gas-collection chambers.

Core, section	Depth to top of section (mbsf)	Insertion temperature ($^{\circ}$ C)	Gas evolved (mL)	Gas/pore water ratio (mL/L)
164-997A-				
2H-3	5	11.9	0	0
3H-3	15	11.3	0	0
4H-3	24	12.5	150	27
5H-3	34	11.1	530	98
6H-3	43	12.4	920	171
8H-3	55	10.5	980	183
9H-3	64	15.0	1304	245
10H-3	73	13.0	760	143
11H-3	83	14.1	1412	267
12H-3	92	11.9	780	148
13H-3	101	12.7	1029	196
14H-3	110	14.8	530	101
15H-3	121	13.4	400	76
16H-3	130	12.5	2580	497
17H-3	140	14.6	320	61
20H-3	164	13.0	265	51
21X-3	169	14.4	0	0
22X-4	176	11.0	90	17
26X-2	204	9.2	0	0
30X-2	232	12.2	0	0
31X-3	235	10.4	170	34
32X-2	252	6.0	120	24
34X-3	264	10.0	240	48
35X-3	272	9.9	220	44
36X-3	281	—	180	36
38X-3	301	12.2	130	26
39X-4	313	10.5	190	39
41X-3	322	11.0	180	37
43X-3	340	11.5	250	52
44X-3	350	11.3	370	78
46X-3	369	11.3	180	38
47X-3	378	14.4	175	37
48X-3	388	12.7	275	59
52X-3	408	6.1	225	48
54X-3	428	13.7	130	28
164-997B-				
3X-1	338	—	200	42
5X-3	427	11.7	110	24
11X-4	467	8.4	290	64
13X-1	481	10.0	19	4
14X-1	491	8.2	0	0
16X-2	503	8.3	150	33
18X-3	523	9.7	250	57
19X-4	534	10.8	395	90
20X-2	541	11.6	106	24
22X-5	556	11.7	0	0
23X-2	560	10.4	160	37
24X-2	570	12.0	280	65
26X-2	580	9.5	190	44
29X-2	608	11.6	250	59
31X-2	627	10.8	150	35
45X-2	724	12.3	240	60
46X-2	732	15.7	120	30
47X-3	744	13.8	190	48

Note: — = not available.

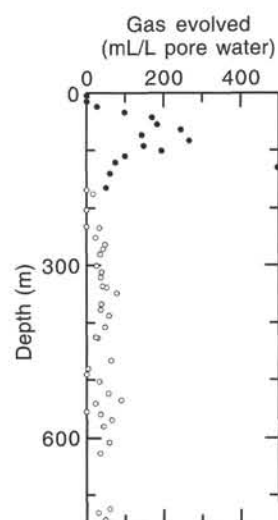


Figure 11. Plot of volume of gas evolved per liter of pore water from 1.5-m whole-core sections as they warmed to room temperature in gas-collection chambers. The total amount of gas was corrected by the porosity of the cores to give 1 mL of pore water. Solid circles = measurements on APC cores. Open circles = XCB core measurements.

mbsf; see “Inorganic Geochemistry” section, this chapter). Although the values rise erratically, the general pattern is an increase in gas volume downward throughout the APC cores (Fig. 11). These are minimum values for the cores, which expanded considerably before they were received on the catwalk and were observed to release gas before they could be placed in the chambers. However, the volume of gas evolved from XCB cores is consistently low (i.e., Core 164-997A-21X). The data suggest that the decreasing gas concentration below 166.9 mbsf is an artifact of the XCB coring process. However, the amounts of gas that are measured in the upper 144 mbsf with the gas-collection tubes are small in comparison with the amount of methane that is required to saturate the waters under in situ conditions (see Fig. 22, “Site 994” chapter, this volume).

Gas Hydrate Occurrence

The occurrence of one zone of massive gas hydrate at Site 997 indicates that conditions appropriate for the formation of massive gas hydrate exist in this section. However, this massive hydrate may not be typical of most of the gas hydrate that is distributed throughout this sedimentary sequence. We suspect that the massive gas hydrate oc-

curred within a small fault plain. Small, near-vertical faults are common in this area (Rowe and Gettrust, 1993). Temperature observations, interstitial-water chloride contents, and velocity and electrical resistivity log data indicate that disseminated gas hydrate also occurs throughout the sedimentary section between ~180 and ~450 mbsf. It is inferred that gas hydrate occurs within the available pore spaces of these porous sediments (see "Physical Properties" section, this chapter).

BIOSTRATIGRAPHY

Nannofossil biostratigraphy was studied in Holes 997A and 997B. Cores from Hole 997B that duplicated depth intervals from Hole 997A were not examined. Therefore, shipboard biostratigraphy was conducted for the remaining 46 cores (18 APC and 28 XCB) and 35 cores (all XCB) of Holes 997A and 997B, respectively, for which there was recovery. Core-catcher samples were routinely examined, but where it was necessary to refine zonal boundaries additional core samples were examined.

A continuous sequence of nannofossil zones and subzones was observed from the Holocene to the upper Miocene in Holes 997A and 997B, similar to the previous observations at other Blake Ridge sites (994 and 995). However, sedimentation at this site is more discontinuous than at the other sites, and two short hiatuses were detected in the lower Pleistocene (Subzone CN13a) and lower Pliocene (Subzones CN11a–CN10d). Another short hiatus is likely in the uppermost Miocene (Subzone CN9b).

Nannofossils are abundant throughout the examined samples, except for two cores (164-997A-9H and 997B-12X) in which moderately preserved nannofossils are only common.

Preservation of nannofossils is uniformly good only in the upper 30 m and varies from good to moderate down to Sample 164-997A-26X-CC (210.68 mbsf). Preservation then remains moderate to the bottom of Hole 997B, and weak dissolution was observed in most of the moderately preserved nannoflora. Below Sample 164-997A-44X-CC (356.0 mbsf), slight overgrowths are typical. Moderately heavy recrystallization was observed only in Sample 164-997A-44X-CC (356.0 mbsf).

Reworked Cretaceous to Paleogene nannofossils as well as ascidian spicules that have moved downslope occur routinely in many samples, but their occurrences are relatively minor (as in Holes 994C and 995A). Reworking of Neogene nannofossils at this site is less severe than at Hole 995A, but detailed identification of zones and subzones was difficult for some intervals (Fig. 12).

Hole 997A

Pleistocene

The upper nine cores of Hole 997A yielded Pleistocene nannofloras. The dominant presence of *Emiliania huxleyi* in Samples 164-997A-1H-1, 0–1 cm, and 1H-CC (2.90 mbsf) indicates a Holocene or latest Pleistocene age (<0.085 Ma). In Sample 164-997A-2H-1, 0–1 cm (2.90 mbsf), however, *E. huxleyi* is only a common member of the flora; the next sample examined (164-997A-2H-1, 114–116 cm) contains no *E. huxleyi*. Thus, a significant coring gap or a hiatus exists between Cores 164-997A-1H and 2H. The interval between Samples 164-997A-2H-1, 114–116 cm, and 2H-CC belongs to upper Pleistocene Subzone CN14b.

Samples 164-997A-3H-1, 0–1 cm, through 5H-7, 39–41 cm, are assignable to Subzone CN14a. The last occurrence (LO) of *Reticulofenestra asanoi* (0.88 Ma) was observed in Sample 164-997A-5H-3, 39–41 cm, and the lower/upper Pleistocene boundary (0.78 Ma) is located within the upper sections of Core 164-997A-5H (31.40–34.40 mbsf).

Samples 164-997A-6H-1, 39–41 cm (41.30 mbsf), and 6H-4, 39–41 cm (45.80 mbsf), belong to the "small *Gephyrocapsa* Zone" that

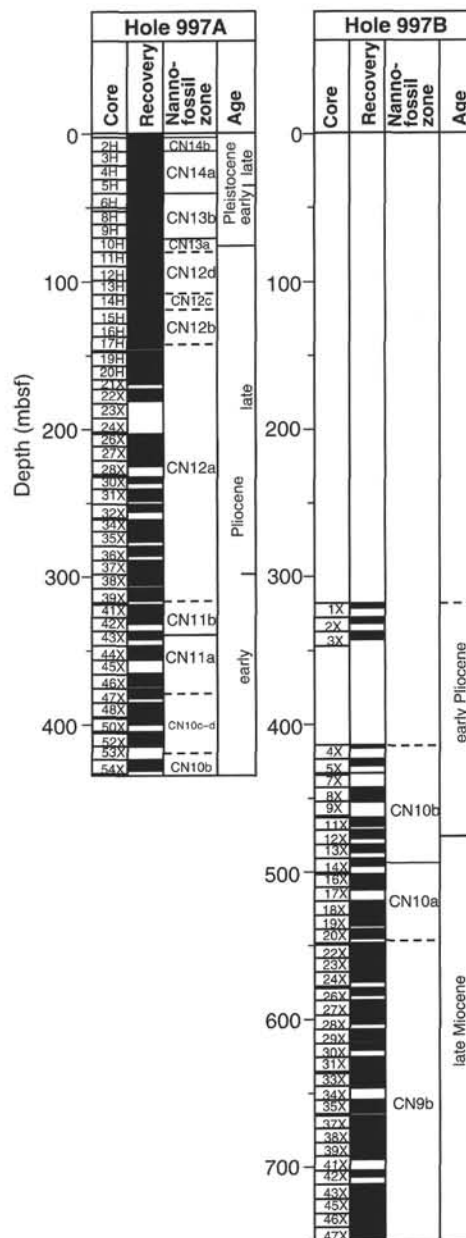


Figure 12. Biostratigraphic summaries of Holes 997A and 997B. Dashed lines indicate that the zonal boundaries are ambiguous because of reworking.

corresponds to the upper part of lower Pleistocene Subzone CN13b. The next deeper sample (164-997A-6H-5, 39–41 cm; 47.30 mbsf) contains frequent specimens of *Helicosphaera sellii*, whose LO is a time-transgressive event with the youngest documented age of 1.26 Ma. Because the LO of *Calcidiscus macintyreii* (1.60–1.64 Ma) is in Sample 164-997A-9H-3, 49–51 cm (64.90 mbsf), the interval identifiable between the LO of *H. sellii* and the beginning of the "small *Gephyrocapsa* Zone" (minimum time span of 0.16 m.y.) seems too short. Therefore, a short hiatus is suspected within the lower part of Core 164-997A-6H.

The first occurrence (FO) of *Gephyrocapsa caribbeanica* (1.8 Ma) is in Sample 164-997A-9H-CC (71.47 mbsf). The Pliocene/Pleistocene boundary at Hole 997A, therefore, lies between this sample and Sample 164-997A-10H-CC (80.88 mbsf). This is the shallowest occurrence of the boundary among the three sites drilled at the Blake Ridge (Fig. 13).

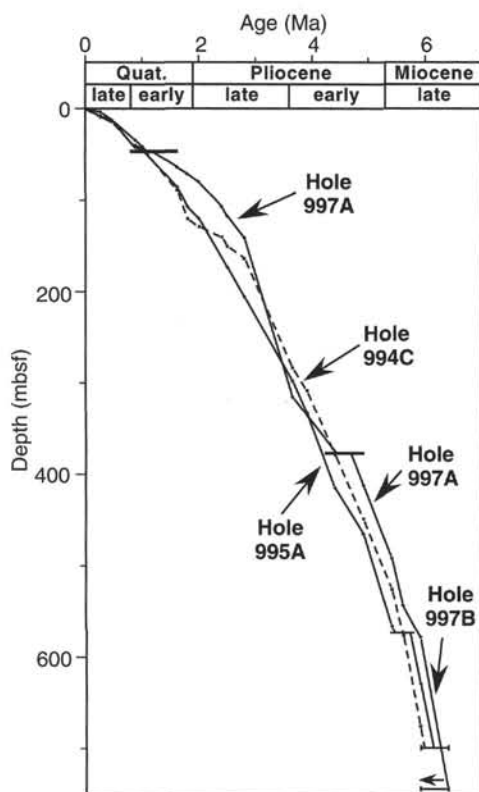


Figure 13. Age-depth relationships of biostratigraphic markers of calcareous nannofossils at Sites 997, 995, and 994. Horizontal bars at the bottom of the figure indicate the range of *Amaurolithus amplificus*.

Pliocene

Samples 164-997A-11H-1, 49–51 cm, through 39X-CC belong to upper Pliocene Zone CN12. Because of the lack of significant reworking, the LOs of the key discoasters defining the subzones of Zone CN12 were easy to identify. The LOs of *Discoaster brouweri* (top of Subzone CN12d), *Discoaster pentaradiatus* (top of CN12c), *Discoaster surculus* (top of CN12b), and *Discoaster tamalis* (top of CN12a) were observed in Samples 164-997A-11H-1, 49–51 cm (80.90 mbsf), 13H-7, 114–116 cm (108.63 mbsf), 14H-7, 114–116 cm (118.55 mbsf), and 17H-5, 49–51 cm (143.90 mbsf), respectively.

The very rare occurrence of *Reticulofenestra pseudumbilica* in Samples 164-997A-38X-CC and 39X-CC was regarded as reworked, and the LO of this taxon (top of Zone CN11: 3.65 Ma) is in Sample 164-995A-41X-1, 30–31 cm. The interval between this sample (319.0 mbsf) and Sample 164-997A-43X-1, 30–32 cm (337.31 mbsf), is assignable to lower Pliocene Subzone CN11b. The LO of *Amaurolithus tricorniculatus* was tentatively identified at Sample 164-997A-47X-CC, and the interval between Samples 164-997A-43X-2, 26–28 cm (338.70 mbsf), and 47X-3, 30–32 cm (378.90 mbsf), belongs to Subzone CN11a. Rare specimens of *Amaurolithus delicatus* observed in some samples of Cores 997A-43X through 46X were regarded as reworked.

The FO of small *Gephyrocapsa*, observed to occur within the upper part of Subzone CN11a at Sites 994 and 995, was recognized in Sample 164-997A-44X-CC (355.97 mbsf). Compared with observations made at Holes 994C and 995A, the interval for the middle to lower portions of this subzone below the FO of small *Gephyrocapsa* (13.5 m) is much shorter than that of the upper part of this subzone (28.1 m) above this event. Therefore, a hiatus, corresponding to the middle and/or lower parts of Subzone CN11a, is suspected within the lower sections of Hole 997A.

Samples 164-997A-47X-CC (380.21 mbsf) through 53X-CC (414.13 mbsf) were assigned to Subzones CN10c–10d.

Rare specimens of *Ceratolithus acutus* were found in Sample 164-997A-54X-1, 28–30 cm (423.99 mbsf), which thus marks the top of Subzone CN10b at this hole.

Hole 997B

The uppermost sample examined at Hole 997B (164-997B-4X-1, 0–1 cm; 414.20 mbsf) contains no *C. acutus*, but the taxon is present from the next examined Sample 997B-4X-CC (416.17 mbsf) downward. The LO of *C. acutus* (top of Subzone CN10b), therefore, is placed between these samples, and it is concordant with the observation at Hole 997A in which the event was placed between 414.13 and 423.99 mbsf.

Samples 164-997B-4X-CC through 14X-3, 31–33 cm (494.13 mbsf), belong to Subzone CN10b, and the Miocene/Pliocene boundary is probably located within Cores 164-997B-12X or 13X. Although very rare, the occurrence of the key species, *C. acutus*, is consistent in this subzone.

The interval between Samples 164-997B-14X-4, 29–31 cm, and 20X-CC contains nannoflora of Subzone CN10a. Because *Discoaster berggrenii* and *Discoaster quinqueramus* are common to abundant in Sample 164-997B-22X-1, 40–41 cm, downward and the lowest sample of this hole (164-997B-47X-CC) contains *Amaurolithus* spp., Cores 164-997B-22X through 47X belong to upper Miocene Subzone CN9b. The LO of *Amaurolithus amplificus* (5.9 Ma) was observed in Sample 164-997B-26X-4, 30–32 cm (583.72 mbsf), and the taxon is present almost continuously down to the bottom of this hole. The LO of *Triquetrorhabdulus farnsworthii* coincides with that of *A. amplificus*. This could be another useful biostratigraphic marker to supplement the presence of *A. amplificus*, which is generally very rare in middle-latitude regions.

Sedimentation Rate

Although the presence of hiatuses and possible winnowings interrupts the general trend, sedimentation rates calculated from nannofossil datum events increase downhole, as was observed in Holes 994C and 995A (Fig. 13). The sedimentation rate for the last 0.46 m.y. is 27 m/m.y., which is slightly lower than at Hole 994C (30 m/m.y.) and at Hole 995A (29 m/m.y.). The coring gap or hiatus recognized between Cores 164-997A-1H and 2H, therefore, may represent a relatively short interval. Because of the short hiatus in the upper lower Quaternary sequence, the sedimentation rate calculated for the entire Quaternary is 40 m/m.y.—significantly lower than at Hole 994C (68 m/m.y.) and at Hole 995A (60 m/m.y.).

The sedimentation rate for the upper Pliocene sequence of Hole 997A is the highest (133 m/m.y.) among the three Blake Ridge sites (Fig. 13). The big contrast between the upper upper and lower upper Pliocene (72 vs. 205 m/m.y.) may partly be due to the reworking of key discoasters whose LOs define the upper boundaries of the late Pliocene subzones. The sedimentation rate (80 m/m.y.) for the upper lower Pliocene above the detected hiatus (between 378.90 and 380.00 mbsf) seems too low compared with that of the immediately overlying sequence as well as with the trends observed at Sites 994 and 995. Therefore, another hiatus or a combination of short hiatuses is suspected within the upper lower Pliocene sequence (Fig. 13). The sedimentation rate is 160 m/m.y. for the lower lower Pliocene sequence.

The sedimentation rate for the upper Miocene sequence (between 5.4 and 6.4 Ma) is more than 256 m/m.y. However, the rate drops to 116 m/m.y. between 5.6 and 5.9 Ma, and another short hiatus is suspected between 550.20 and 583.72 mbsf at Hole 997B. This suspected hiatus partly overlaps with the hiatus detected at Hole 995A (Fig. 13).

Because coring stopped above the FO of *A. amplificus* (6.4 Ma), a sedimentation rate cannot be estimated for the lowest sequence of

Hole 997B. The minimum rate calculated for the lowest 170-m sequence at Hole 997B (below 583.40 mbsf) is 340 m/m.y. This is close to the value for the uppermost Miocene sequence at Hole 994C (303 m/m.y.). Therefore, the bottom age at Hole 997B is likely to be very close to the FO of *A. amplificus* (6.4 Ma).

PALEOMAGNETISM

Magnetostratigraphy

Paleomagnetic measurements at Hole 997A were carried out with the pass-through cryogenic magnetometer, following the procedures outlined in the “Explanatory Notes” chapter (this volume). We measured the NRM on the cores taken with the APC (Cores 164-997A-1H through 20H) and demagnetized them under an AF of 15 mT to determine the direction of the stable component of remanence. Routine measurement of remanence was abandoned for the subsequent XCB cores (164-997A-21X through 54X) because they were highly biscuitized during drilling. To supplement magnetostratigraphic results from the routine demagnetization, 21 discrete samples were AF demagnetized in 5-mT steps up to 45 mT.

The intensity of NRM fluctuates between 100 and 0.1 mA/m through the APC-cored interval (Fig. 14). Each peak in NRM intensity occurs at the top of a core, suggesting that the fluctuations are a result of contamination from drill pipe rust. The NRM declination is frequently near 0° (360°) with scattered measurements, and the inclination is generally steeply downward (near +90°), suggesting that a core barrel overprint was acquired during coring.

After demagnetization at 15 mT, intensity is generally between 1 and 0.1 mA/m (Fig. 15). The inclination after 15-mT demagnetization shifts toward lower inclinations and shows negative and positive intervals. The decrease in intensity and inclination suggests that the demagnetization has removed the core-barrel overprint. The declination after 15-mT demagnetization is less scattered than that of NRM. Before Tensor tool orientation, demagnetized declinations are generally grouped around 180°, relative to the x-axis direction defined by the double-line fiducial mark in the center of the core liner on the archive half of the cores. Orientation of declination relative to geographic north (see “Paleomagnetism” section, “Explanatory Notes” chapter, this volume) produces a distinct break at the top of each core (Fig. 16); this may be explained by a bias in the relative responses of the x- and y-axis sensors in the cryogenic magnetometer to the very weak remanence surviving after demagnetization (see “Paleomagnetism” section, “Explanatory Notes” chapter, this volume).

Progressive AF demagnetization of the discrete samples shows that the steeply downward-inclined drilling-induced components can be removed from most samples, leaving a stable component of remanence at 5 mT (Fig. 17A). After the removal of the overprint, progressive demagnetization up to 45 mT typically follows a linear demagnetization path that converges on the origin of the Zijderveld plot. Some samples display removal of a positive inclination component of remanence from a stable negative inclination component, which converges on the origin of the Zijderveld plot between 10 and 40 mT (Fig. 17B). We interpret the soft components as a viscous remanent magnetization (VRM) and the more stable component as a primary remanence, indicating reverse polarity. The stepwise demagnetization analysis of the discrete samples suggests that a magnetostratigraphy can be constructed for the APC-cored interval in Hole 997A.

Polarities determined from analysis of the discrete samples correlate well with the inclination data obtained from the 15-mT demagnetization of the continuous core sections in the cryogenic magnetometer (Fig. 18). Based on the inclination and polarity data with the constraint of the nannofossil datums (see “Biostratigraphy” section, this chapter), polarity chron boundaries were determined for the APC-cored interval. The lower boundary of the C1r.1n subchron (Jaramillo normal chron) is at 52 mbsf; the upper and lower bound-

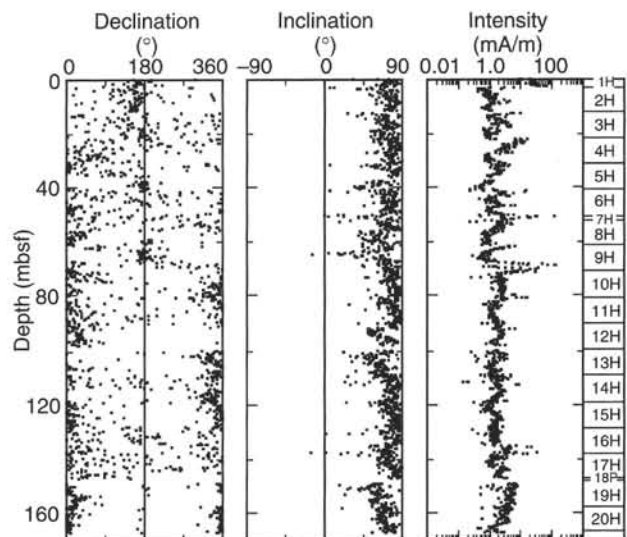


Figure 14. NRM declination (referred to arbitrary core coordinates), inclination, and intensity for Hole 997A.

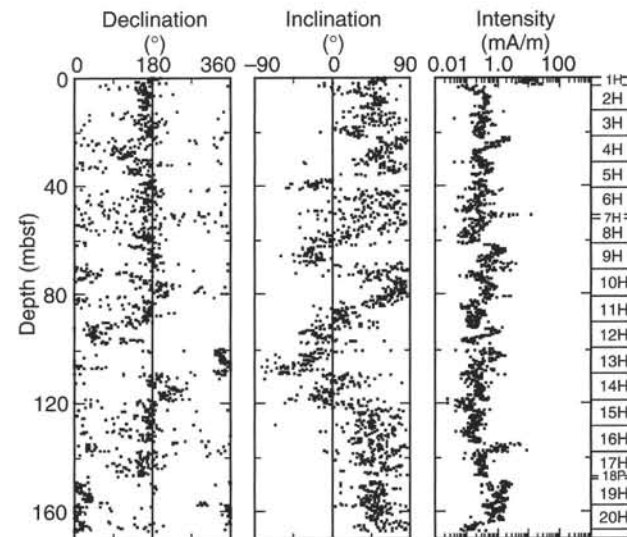


Figure 15. Declination (core coordinates), inclination, and intensity after 15-mT demagnetization for Hole 997A.

aries of the C2n (Olduvai normal chron) are at 72 and 84 mbsf, respectively; and the C2An/C2r boundary (Gauss/Matuyama boundary) is at 122 mbsf. The C1n/C1r boundary (Brunhes/Matuyama boundary) and the upper boundary of the C1r.1n (top of Jaramillo normal chron) is tentatively defined at 36 and 41 mbsf, respectively, based on the cryogenic magnetometer record (Fig. 18).

Sample 164-997A-3H-4, 48–50 cm (17.39 mbsf), appears to indicate reverse polarity. Its stratigraphic position is too deep to correspond to the Blake event (e.g., Smith and Foster, 1969), which has been assigned an age of ~0.11 Ma, unless depositional rates during the late Pleistocene were very nonuniform. It is possible that this sample has recorded the proposed Biwa II excursion, reported in work on Japanese sediments and assigned an age of 0.292–0.298 Ma (Kawai et al., 1972). However, care should be exercised in identifying a polarity reversal on the basis of a single sample, given the possibility that this sample may have been inadvertently sampled with the uphole arrow inverted.

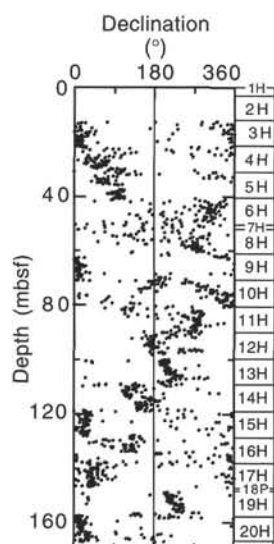


Figure 16. Declination data oriented to geographic coordinates with the Tensor tool after 15-mT demagnetization for Hole 997A.

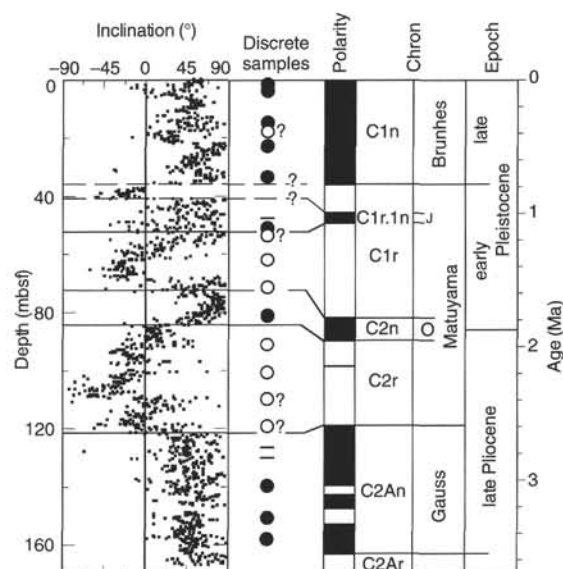


Figure 18. Inclination and polarity data determined from Zijderveld diagram analysis of discrete samples from Hole 997A, correlated to the revised geomagnetic polarity time scale of Cande and Kent (1995). Solid circles and zones = normal polarity, open circles and zones = reverse polarity, question marks (?) = less certain polarity, and bars = unsuccessful analyses. J = Jaramillo, and O = Olduvai.

increases from $\sim 6 \times 10^{-5}$ (all susceptibilities are in volume-normalized SI terms) at the mudline to $\sim 50 \times 10^{-5}$ at 2.5 mbsf, presumably reflecting bacterial authigenesis of magnetite (Fig. 19). There are a pair of local susceptibility maxima at 2.3 and 2.5 mbsf; these may correspond to the more clearly defined pair of maxima observed at Site 995. Susceptibility declines sharply below 2.5 mbsf to reach values of $\sim 6 \times 10^{-5}$ by 4 mbsf, probably as a result of bacterially mediated reduction of magnetite to iron sulfides.

Susceptibility declines downhole to a minimum of $\sim 4\text{--}5 \times 10^{-5}$ between ~ 45 and 55 mbsf. Susceptibility increases again to a local maximum of $\sim 10 \times 10^{-5}$ at 65 mbsf before returning to $\sim 6 \times 10^{-5}$ at ~ 80 mbsf. A similar local maximum was observed at 83 mbsf at Site 995; however, the increase in pyrite concentration corresponding to the susceptibility maximum noted at this depth at Site 995 is not evident in XRD analyses at Site 997. Another local maximum occurs at ~ 135 mbsf. Below this depth, susceptibility downhole maintains a background value of $\sim 8\text{--}10 \times 10^{-5}$, with small cyclic variations on a 1- to 5-m scale similar to those seen at Sites 994 and 995 (see "Paleomagnetism" section, "Site 994" and "Site 995" chapters, this volume).

The susceptibility record in Hole 997B is very noisy, and trends are difficult to discern. Susceptibility may increase slightly below ~ 540 mbsf in the upper Miocene part of the sequence, as it did at Sites 994 and 995.

Rock Magnetism

Saturation isothermal remanence normalized for susceptibility (SIRM/k) at Site 997 (Fig. 20) confirmed the downhole trends seen at Sites 994 and 995 (see "Paleomagnetism" section, "Site 994" and "Site 995" chapters, this volume), although there are some intriguing differences. Samples below 400 mbsf clearly define the same log-linear downhole trend in SIRM/k at Site 997 as was seen at Sites 994 and 995. Superimposed on this background is an interval of anomalously high SIRM/k, extending from ~ 30 mbsf to $\sim 240\text{--}300$ mbsf. This interval differs at Site 997 in that the trend defined by SIRM/k is smoother and more continuous than at Sites 994 or 995. Between

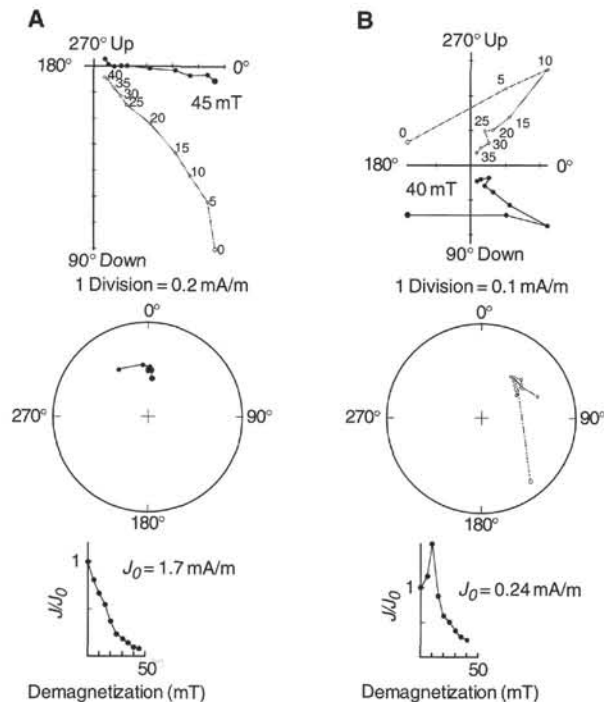


Figure 17. Representative Zijderveld, stereo, and intensity demagnetization plots for (A) Sample 164-997A-20H-1, 57-59 cm (157.97-157.99 mbsf), and (B) Sample 164-997A-12H-1, 64-66 cm (90.57-90.59 mbsf). Demagnetization increases in 5-mT steps to 45 mT for (A) and 40 mT for (B). Zijderveld plot: solid circles = projection on the horizontal plane; open circles = projection on the vertical plane. Stereo plot: solid circles = the lower hemisphere. Declination is with respect to core coordinates.

Magnetic Susceptibility

Measurement of magnetic susceptibility of whole-core sections from Holes 997A and 997B using the MST produced a similar record to those observed at Sites 994 and 995 (see "Paleomagnetism" section, "Site 994" and "Site 995" chapters, this volume). Susceptibility

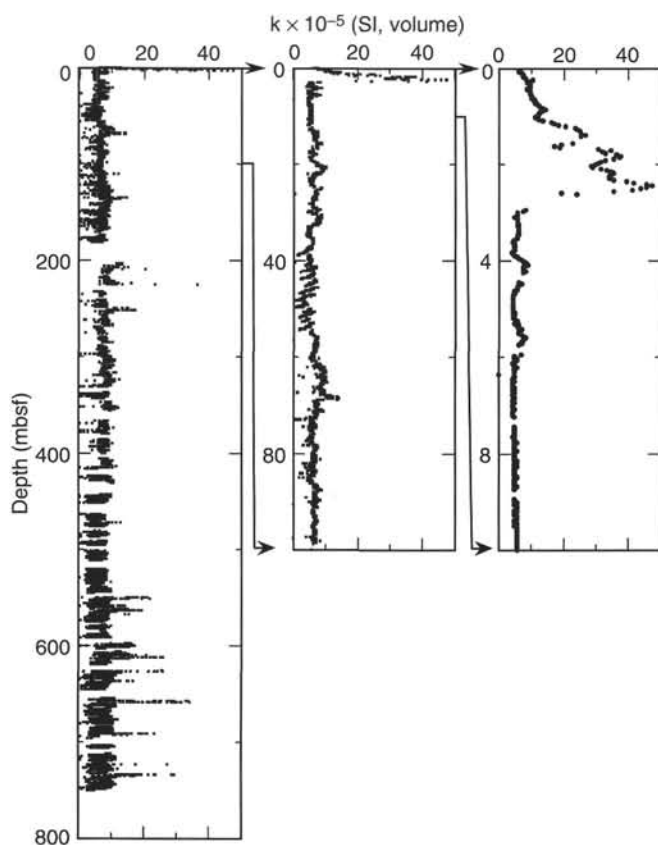


Figure 19. Susceptibility determined on the MST. Combined data for Holes 997A and 997B.

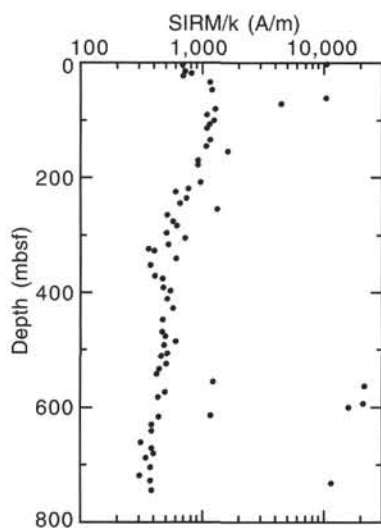


Figure 20. SIRM/k vs. sub-bottom depth. Combined data from Holes 997A and 997B.

~300 and 400 mbsf, there is an interval of anomalously low SIRM/k; similar values are not reached on the main log-linear trend of SIRM/k until below 600 mbsf.

Very high values of SIRM/k (>10 kA/m) characterize the high susceptibility interval above 4 mbsf. As at Sites 994 and 995, these presumably reflect the presence of a substantial proportion of SD grains. Sample 164-997A-1H-2, 48–50 cm (1.99 mbsf), the shallowest sample measured, has an $S_{-0.3T}$ ratio of 0.95 (Fig. 21), indicating a

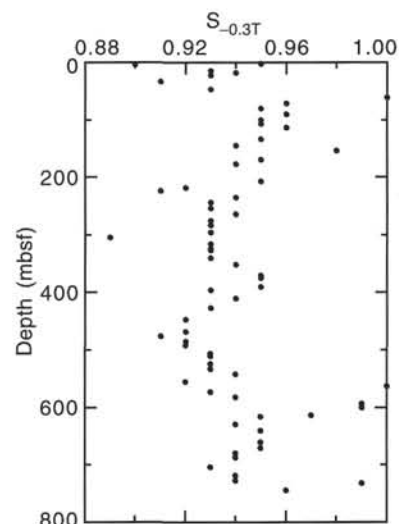


Figure 21. $S_{-0.3T}$ vs. sub-bottom depth. Combined data from Holes 997A and 997B.

significant proportion of a magnetic phase with coercivity higher than magnetite. It is likely that magnetic sulfide authigenesis has already commenced at this sub-bottom depth.

As at Sites 994 and 995, there is a series of samples in the upper Miocene sequence at Site 997 with SIRM/k values >10 kA/m and $S_{-0.3T}$ values ≥ 0.98 . These samples are dominated by SD magnetite (see “Paleomagnetism” section, “Site 994” chapter, this volume), and they probably represent a local interval of decreased reduction, resulting in less complete reduction of magnetite to iron sulfides.

Summary of Rock Magnetism and Susceptibility

Rock-magnetic analysis at Site 997 was limited by available time but confirms the pattern established at Sites 994 and 995. Initial detrital magnetite deposition is followed by authigenic (presumably microbial) generation of SD magnetite and magnetic sulfides within the first few meters below seafloor, by further reduction to remove most magnetite (and almost all magnetite in the fine-grained, SD range) below ~4 mbsf, and by an apparently highly uniform continued reduction of the magnetic iron sulfides toward pyrite downhole.

Superimposed on this trend is an interval of anomalously high SIRM/k between ~30 and 240–300 mbsf, which we interpret as the result of the development of a second generation of magnetic sulfides in the upper part of the gas hydrate stability zone. As at Sites 994 and 995, this interval corresponds to a zone of downhole-decreasing interstitial-water chloride content (see “Inorganic Geochemistry” section, this chapter), in a manner closely analogous to Leg 146 Sites 889 and 890 (Shipboard Scientific Party, 1994). The base of the high SIRM/k zone lies within an interval from ~200 to 300 mbsf marked by inflections in several interstitial-water profiles (see “Inorganic Geochemistry” section, this chapter).

Presumably, the growth of magnetic sulfides, both in the initial zone of magnetite reduction between 2.5 and 4 mbs, and within the interval from 30 to 240–300 mbsf, is mediated by bacteria flourishing in response to the availability of organic materials; within the lower interval, the feedstock is presumably methane hydrate (Housen and Musgrave, 1996). The log-linear background decline in SIRM/k can be explained by the inorganic conversion of greigite (and pyrrhotite?) to pyrite in response to the very small amounts of H_2S available below the sulfate reduction zone. Magnetic sulfides, although they make up a tiny proportion of the sediments, may indeed act as a buffer, consuming all available H_2S . The much larger proportions of magnetic sulfides present in the upper part of the hydrate zone evidently are able to survive further reduction to pyrite. However, below

Table 6. Description of PCS deployment at Site 997.

Core	Depth (mbsf)	Pressure			Cutting shoe	Core recovered (cm)	Manifold design	Total gas released (mL)
		Expected (psig)	Observed (psig)	Hydrostatic (%)				
164-997A-								
18P	146.90	4297	4289	100	Push-in	0.42	PCS-M4	450
25P	202.40	4378	4500	103	Push-in	0.88	PCS-M4	7485
29P	231.30	4421	4621	105	Push-in	0.00	Sed. only	Not taken
33P	260.10	4463	4783	107	Push-in	0.00†	PCS-M4	<305†
40P	317.70	4547	465	10	Push-in	0.00	PCS-M4	175
49P	394.90	4661	3666	79	Push-in	0.64	PCS-M4	7050
51P	404.50	4675	3987	85	Push-in	0.47	Sed. only	Not taken
55P	433.30	4717	750	16	Push-in	0.50	PCS-M4	6380
164-997B-								
6P	434.40	4718	0	0	Push-in	0.24	PCS-M4	Not taken
10P	462.20	4759	4460	94	Push-in	0.14	PCS-M4	5125
15P	501.80	4817	4485	93	Push-in	0.30	PCS-M4	3190
21P	549.90	4888	4578	94	Auger	0.94	PCS-M4	3455
25P	577.60	4929	0	0	Auger	0.00	PCS-M4	Not taken
29P*	606.50	4971	4834	97	(Auger)	0.00	PCS-M4	110
32P	635.30	5013	4750	95	Auger	0.00	PCS-M4	70
36P	664.10	5055	5122	101	Auger	0.00	PCS-M4	120
40P	693.00	5098	4947	97	Auger	0.00	PCS-M4	70
44P	721.80	5140	4808	94	Pilot bit	0.00	PCS-M4	80

Notes: The water depth at Site 997 is 2782 m. Expected pressure is the hydrostatic pressure assuming a pressure gradient of 1.467 psi/m. Observed pressure is that first recorded at the PCS sampling station. Sed. only = PCS run used only for collection of sediment. † = the reported volume of recovered core is too low or the total volume of gas released is too high. * = Core 164-997B-29P was deployed as blank (water) PCS run (see text). (Auger) = auger shoe was not applied.

300 mbsf, still within the hydrate zone, the proportion of magnetic sulfides declines sharply to the background values (and at Site 997 between 300 and 400 mbsf, to less than the background trend).

A possible explanation for both the survival of magnetic sulfides in the upper part of the hydrate zone and their sudden reduction below 260–300 mbsf is that although the availability of H₂S for inorganic reactions is normally restricted in the gas hydrate zone (perhaps because H₂S is taken up in the hydrate structure), hydrate melting accompanying a sudden upward shift in the base of the hydrate stability field at some time in the past has flushed the interval below ~300 mbsf with H₂S.

DOWNHOLE TOOLS AND SAMPLING

Pressure Core Sampler

The PCS was deployed 18 times at Site 997 (Table 6) with similar objectives and procedures as those at Sites 994 and 995 (see “Downhole Tools and Sampling” sections, “Site 994” and “Site 995” chapters, this volume). However, differences regarding PCS operations at Site 997 were (1) the PCS was used twice as a gas hydrate sampling chamber and (2) a specific depth was pre-targeted for a PCS core. Core 164-997B-10P (462.2 mbsf) was deployed to determine the volume and composition of gas immediately below a prominent BSR (see “Background and Objectives” section, this chapter). The BSR (see “Background and Objectives” section, this chapter) is inferred to occur at the depth (451 mbsf) marked by a sharp decrease in velocity on the sonic log (see “Downhole Logging” section, this chapter). In addition, the flappers of the core catcher for Core 164-997B-29P* (see Table 6 note) were reversed to examine the volume and composition of gas in a PCS run without a sediment core.

Gas and Core Description

Gas samples were not collected from the two PCS runs (Cores 164-997A-29P and 51P) designed to collect gas hydrate samples (see below). Gas samples also were not collected from Cores 164-997B-6P and 25P because these cores were recovered at atmospheric pressure (Table 6).

The amount of gas that evolved from the other 14 PCS cores at Site 997 (Table 6) ranges between 70 mL (Core 164-997B-32P and 40P) and 7485 mL (Core 164-997A-25P). These gas volumes prima-

rily are mixtures of He, air (N₂ and O₂), CH₄, and CO₂ (Table 7). Helium is used to purge the PCS-M, and it is present in the first few gas samples of any PCS run (<150 mL cumulative volume) or after the manifold has been taken apart to remove sediment clogs. The amount of air does not exceed 175 mL in any PCS run. The amount of CO₂ also is relatively small (Table 7). Therefore, large volumes of gas (>350 mL) that evolved from PCS runs are predominantly composed of CH₄. All gas samples collected below 450 mbsf also contain significant amounts of isobutane and *n*-heptane (Table 7).

Sediment cores from the PCS are similar in lithology to sediment cores recovered by APC and XCB at adjacent depths. The physical properties of sediment from the PCS cores (Table 8) are also similar to those from APC and XCB cores at the same depth (see “Physical Properties” section, this chapter). An exception is the high water content of mousse-like intervals from certain PCS cores (Samples 164-997A-25P, 76–78 cm; 49P, 38–40 cm; 51P, 7–9 cm; and 55P, 4–6 cm).

Sediment samples from selected PCS cores (between depths of 147.15 and 462.2 mbsf) were squeezed using conventional techniques to obtain interstitial water (see “Inorganic Geochemistry” section, “Explanatory Notes” chapter, this volume). Concentrations of various species in these waters (including Cl⁻ after correction for seawater contamination) are presented in Table 9.

Attempted Gas Hydrate Sampling Using the PCS

Cores 164-997A-29P and 51P were deployed to collect samples of gas hydrate. The PCS was opened as fast as possible after depressurization in both instances. Core 164-997A-29P (231.3 mbsf) had 105% of hydrostatic pressure after recovery (Table 6) but contained no sediment. Core 164-997A-51P (404.5 mbsf) had 85% of hydrostatic pressure after recovery (Table 6). The core contained 47 cm of greenish gray sediment and no observable gas hydrate. However, portions of the sediment core were mousse-like, which may indicate that gas hydrate was present before core recovery and depressurization.

Preliminary Interpretations

The best scientific use for the PCS has been a contentious issue (e.g., Pettigrew, 1992). It was decided early during Leg 164 that the PCS primarily should be used to sample gases collected at in situ

Table 7. Gas composition of samples from the PCS at Site 997.

Core	Sample	Volume (mL)		C ₁ (ppmv)	C ₂ (ppmv)	C ₃ (ppmv)	i-C ₄ (ppmv)	n-C ₄ (ppmv)	i-C ₅ (ppmv)	n-C ₅ (ppmv)	i-C ₆ (ppmv)	n-C ₆ (ppmv)	n-C ₇ (ppmv)	C ₁ /C ₂	C ₁ /C ₂₊	N ₂ (vol%)	O ₂ (vol%)	CO ₂ (ppmv)	
		Split	Cum.																
164-997A-18P	G ₁	30	30	12,964	14	0.3	0.3		0.6	0.1		0.3							494
	G ₃	95	270	173,055	9	5	20.3	11.4	2.5	0.4				9.8	20,123	2,989	14.3	3.4	16
	G ₄	180	450	581,537	23	12	26.7	7.2	6.9		0.1	0.3		25,846	7,682	0.3	0.0	7,630	
25P	G ₁	45	45	3,187			12	26.7	7.2	6.9						60	1.4	0.5	521
	G ₂	15	60	24,448			7	16.9	9.2	0.5	0.3								
	G ₃	660	750	954,449	117	10	14.7	10	3.9	0.3			36.8	8,151	4,940	0.2	0.0		
33P	G ₄	340	6,880	948,136	141	6	6.3	1.5	7.2	0.5	0.3			9.4	6,729	5,820	0.1	0.0	
	G ₅	125	7,005	941,170	140	6	7.2	2.1	7.5	0.6	0.4				6,723	5,425	0.1	0.1	
	G ₁	115	115	165,527	67	528	521	1134	29	1.5	0.3	0.2			2,471	73	13.8	3.0	3,903
	G ₂	110	265	252,934	30	528									8,574	454	4.1	1.0	2,035

Note: Cum. = cumulative volume. Gas samples taken from the PCS are designated (e.g., G₁) in the order in which they were collected. All samples analyzed by the NGA.

Only part of this table is produced here. The entire table appears on the CD-ROM (back pocket).

Table 8. Physical properties of sediment samples from the PCS, Hole 997A.

Core, interval (cm)	Depth (mbsf)	Water content (%)		Density (g/cm ³)			Porosity (%)	Void ratio
		Wet	Dry	Bulk	Grain	Dry		
164-997A-18P, 39-41	147.29	41.8	71.8	1.63	2.72	0.95	66.31	1.90
25P, 28-30	202.68	41.1	69.9	1.63	2.72	0.96	65.27	1.85
25P, 76-78.0	203.16	47.0	88.7	1.53	2.68	0.81	70.39	2.32
49P, 38-40	395.28	33.5	50.4	1.77	2.69	1.18	57.92	1.32
51P, 7-9	404.57	47.1	89.1	1.55	2.69	0.82	71.10	2.34
51P, 30-32	404.80	29.2	41.3	1.82	2.68	1.29	51.85	1.08
55P, 4-6	433.34	43.9	78.3	1.59	2.78	0.89	68.16	2.12
55P, 20-22	433.50	37.5	60.0	1.60	2.77	1.00	58.43	1.62

pressure rather than as a tool for collecting gas hydrate samples. This decision was made for two reasons after consideration of Leg 164 objectives and after examination of how the PCS actually works. First, in situ gas volumes had never been collected during ocean drilling operations, and yet they provide a fundamental constraint for all indirect methods of estimating gas and gas hydrate abundance. Second, there appeared to be no advantage of collecting gas hydrate specimens at in situ pressure in the PCS relative to the APC or XCB. The time to depressurize the PCS, open the tool, and remove a sample was approximately the same time (15 min) as the wireline trip for an APC or XCB core. Experience with Cores 164-997A-29P and 51P did not alter our view on how the PCS should best be used (at least as it currently is designed).

The general interpretation of gas variation during release from the PCS at Site 997 is the same as that given for Site 995 (see "Downhole Tools and Sampling" section, "Site 995" chapter, this volume). Of additional interest are the high concentrations of isobutane and *n*-heptane observed in most gas samples from PCS cores below the BSR (Table 7). Such high concentrations of these hydrocarbons do not reflect a contamination problem unique to the PCS because they also were observed in vacutainer samples from XCB cores (see "Organic Geochemistry" section, this chapter). Recent work (Hovland et al., 1995) has shown that a "pool" of heavy hydrocarbons also occurs near the BSR at ODP Site 892. Two possible explanations for these common enrichments of heavy hydrocarbons below the BSR include fractionation of light and heavy hydrocarbons during gas hydrate formation and entrapment of upward migrating gas.

Observations at Site 995 concerning the amount of gas in borehole water were duplicated at Site 997 (Tables 6, 7). Essentially all gas evolved from the PCS (other than air) comes from the sediment core in the PCS and not the surrounding borehole water.

Preliminary estimates concerning the amount of CH₄ in pore space of sediment at Site 997 can be made using sediment porosity (see "Physical Properties" section, this chapter), volumes of sediment

in the PCS, and the amount of CH₄ released from the PCS. These calculations indicate that sediment pore space in PCS cores contains between 45 and 2400 mM/L CH₄. The lowest value is from Core 164-997A-18P; the highest value is from Core 164-997B-10P. Interstitial water from Core 164-997B-10P is ~10 times oversaturated with CH₄ (see Duan et al., 1992).

The Cl⁻ concentrations (after correction) of interstitial water from Cores 164-997-25P (497 mM) and 55P (444 mM) suggest that these cores contained gas hydrate. This inference is consistent with the amount of gas evolved from the cores inasmuch as the total gas volume is greater than expected from saturation considerations.

The Cl⁻ concentration (514 mM after correction) of interstitial water from Core 164-997B-10P does not indicate freshening caused by gas hydrate decomposition. Thus, the tenfold oversaturation of CH₄ in Core 164-997B-10P results from free gas. Because Core 164-997B-10P was taken at a depth immediately below the BSR, the observation is the first direct evidence for significant quantities of free gas immediately below the BSR (see discussion on this topic in Bangs et al., 1993, and Katzman et al., 1994).

Water-Sampling Temperature Probe and Fisseler Water Sampler

The WSTP was deployed on 10 occasions at Site 997 at depths ranging from 80.4 to 385.3 mbsf (Table 10). In addition, the FWS was deployed once at 118.40 mbsf. Water samples from the tools contain various proportions of in situ interstitial water, borehole water (surface seawater pumped down the hole), and undisplaced water in the sampling coil. A primary objective was to determine the Cl⁻ concentration of the interstitial water (see "Inorganic Geochemistry" section, this chapter, and "Downhole Tools and Sampling" section, "Site 995" chapter, this volume, for a description of methods and correction procedures).

The water samples from the WSTP contain between 1.4% and 49.2% interstitial water; the water sample from the FWS contained 4.4% interstitial water (Table 11). Two observations concerning these samples are that (1) the proportion of interstitial water generally decreases with depth and (2) the estimated concentration of Cl⁻ in the interstitial water generally is similar (within 1 standard deviation) to the Cl⁻ measured on water squeezed from whole-round intervals from the same depth.

The Cl⁻ concentration of Sample 164-997A-17H-1 (550 mM; 137.4 mbsf) has a relatively low uncertainty and is significantly higher than that of interstitial water obtained from the squeezing of whole rounds (527 mM) from a similar depth (see "Inorganic Geochemistry" section, this volume). The pore space of sediment at 137.4 mbsf would have to have contained ~4% hydrate to the account for this apparent freshening. However, profiles of interstitial-water Cl⁻ and the

Table 9. Chemistry of water samples from the PCS at Site 997.

Core, interval (cm)	Depth (mbsf)	pH	Alk (mM)	Sal (g/kg)	Cl ⁻ (mM)	Cl ^{-*} (mM)	Mg ²⁺ (mM)	Ca ²⁺ (mM)	SO ₄ ²⁻ (mM)	PO ₄ ³⁻ (μM)	NH ₄ ⁺ (μM)	H ₄ SiO ₄ (μM)	K ⁺ (mM)	Sr ²⁺ (μM)
164-997A-18P, 25-39	147.15	7.60	71.4	33.5	527	518	22.7	2.5	4.2	167	13,030	109	14.2	75
25P, 8-28	202.48			34.0	531	497	28.5	4.2	12.3	58	10,630	653	14.1	81
25P, 64-74	203.04	7.97	52.9	34.0	535	503	27.7	3.3	12.4	82	11,120	608	15.1	73
55P, 10-34	433.40	7.51	72.7	31.5	476	444	17.1	2.5	7.1		17,470		14.9	68
164-997B-10P, 0-5	462.20			35.0	527	514	16.9	2.8	5.9	24	21,780	834	15.6	89

Notes: Alk = alkalinity, and Sal = salinity. * = values have been corrected for seawater contamination (see "Inorganic Geochemistry" section, "Site 994" chapter, this volume).

Table 10. Description of WSTP and FWS deployment at Site 997.

Core	Depth (mbsf)	Water type (mL)	
		Coil	Overflow
164-997A-11H	80.4	9	15
14H	108.9	10	20
15H*	118.4	NR	NR
17H	137.4	8	15
19H	147.9	8	14
26X	203.4	9	500
31X	240.9	11	31
36X	279.3	0	0
41X	318.7	11	265
44X	346.7	12	270
48X	385.3	0	0

Notes: * = Core 164-997A-15H is a run of the Fisseler tool. NR = not recorded.

downhole sonic log (see "Inorganic Geochemistry" and "Downhole Logging" sections, this chapter) indicate that such high concentrations of hydrate are unlikely above 190 mbsf.

The concentrations of Ca²⁺, Mg²⁺, and K⁺ (after correction for dilution by coil water) are intermediate between seawater and interstitial water (see "Inorganic Chemistry," section, this chapter). However, WSTP water samples are depleted in Ca²⁺ and Mg²⁺ relative to interstitial water squeezed from whole-round intervals. The depletion of these species likely reflects precipitation of carbonate between core recovery and analyses because of CO₂ degassing (see "Inorganic Geochemistry" section, "Site 995" chapter, this volume). Thus, the carbonate precipitation effect on pore-water concentrations appears to be more pronounced for WSTP samples than for squeezed whole rounds.

The most important result regarding the chemistry of WSTP water samples is that Cl⁻ concentrations (after correction for seawater contamination) generally are similar to that of interstitial waters squeezed from whole-round intervals. The implication of this observation is discussed in the "Inorganic Geochemistry" section, this chapter.

ORGANIC GEOCHEMISTRY

The shipboard organic geochemistry program at Site 997 included analyses of volatile hydrocarbons and carbon dioxide; determinations of inorganic carbon, total nitrogen, total carbon, and total sulfur in sediment; and Rock-Eval pyrolysis (for a description of methods, see "Explanatory Notes" chapter, this volume).

Volatile Hydrocarbons

Headspace Gas

Concentrations of methane (C₁) and ethane (C₂) were measured from every core using the standard ODP headspace-sampling technique. Concentrations of headspace gases increase from the base of the sulfate reduction zone (~21 mbsf) to a maximum value of 180,240 μL/kg at 50 mbsf. Below this level, the values decrease to ~150 mbsf

and then generally scatter between 4,000 and 20,000 μL/kg (with some higher and lower values) down to the deepest sample (744.1 mbsf) at Site 997 (Table 12; Fig. 22). Concentrations of C₂ are low (0–10 μL/kg) down to 370 mbsf and increase with considerable variability to a value of 151 μL/kg in the lowest sample (Table 12; Fig. 22). C₁/C₂ ratios are more than 10,000 between ~45 and ~100 mbsf. Between 100 and 400 mbsf, the C₁/C₂ ratios decrease to less than 500 and remain between 100 and 500 to the bottom of Hole 997B.

Free Gas

Concentrations of C₁, C₂, higher molecular weight hydrocarbons, and CO₂ in the free-gas samples show irregular variations caused by air contamination during sampling. Most samples have air contents <20% based on oxygen and nitrogen analyses (Fig. 23). The C₁/C₂ ratios are fairly constant at 25,000–36,000 from 50 to 153 mbsf (Table 13; Fig. 23). From 165 to 430 mbsf, the C₁/C₂ ratio rapidly decreases with depth to a value of ~1600. Superimposed on this trend are several decreases in the C₁/C₂ ratio that are caused by relatively high C₂ concentrations. The downhole C₁/C₂ profile for free gases is similar in shape to the C₁/C₂ profile of the headspace gases (Fig. 24).

Downcore profiles of three additional hydrocarbon ratios, C₁/C₃₊ (defined as C₁/Σ all isomers of C₃, C₄, C₅, and C₆), *i*-C₄/*n*-C₄, and *i*-C₅/*n*-C₅, are shown in Figure 24. More C₃ through C₆ hydrocarbons occur in greater concentration within the samples below 460 mbsf than within the samples from above 430 mbsf.

A distinct group of high molecular weight hydrocarbons (Fig. 25) occurs in gas from the PCS in considerably higher concentrations than in free-gas samples. The origin of these high molecular weight hydrocarbons is not yet understood, although contamination cannot be excluded.

Gas-Collection Chamber Samples

The C₁ concentrations in gas from the GCC are 1 to 2 orders of magnitude higher than corresponding C₁ headspace concentrations but less than in free-gas samples (Table 14). The C₁/C₂ ratio decreases with depth, as was observed for free gas.

Gas Hydrate Samples

Ratios of C₁/C₂ in decomposed gas hydrate samples are highly variable. Gas from a dissociated gas hydrate sample in Section 164-997A-42X-3 (330 mbsf) had a C₁/C₂ ratio of 4936. In comparison, the C₁/C₂ ratios of gas hydrate samples from Holes 996B and 996E were between 1000 and 1400 (see "Gas Hydrate" section, "Site 996" chapter, this volume) and 11,480 from Hole 994C (see "Gas Hydrate" section, "Site 994" chapter, this volume).

Visible Hydrocarbons

Visible oil was observed sporadically in microscopic porous features in the sediment from a depth from 491.1 to 644.9 mbsf. These features include foraminifers, and quartz sand pockets where oil res-

Table 11. Chemistry of water samples from the WSTP and proportion of seawater, coil water, and interstitial water, Hole 997A.

Core	Depth (mbsf)	Li ⁺ (ppm)	Iσ (%)	Cl ⁻ (mM)	Iσ (%)	SO ₄ ²⁻ (mM)	Iσ (%)	NH ₄ ⁺ (mM)	K ⁺ (mM)	Mg ²⁺ (mM)	Ca ²⁺ (mM)	Water type (%)			Cl ^{-*} (mM)	Iσ (%)
												Coil	Seawater	Interstitial		
164-997A-Coil water		1056	0.70	152	0.28											
11H	80.4	17	1.1	554	0.18	14.75	1.51	2.5	8.2	33.4	5.7	1.6	49.3	49.2	541	2.3
14H	108.9	18	1.2	555	0.18	15.44	1.73	4.7	11.1	38.6	6.0	1.7	51.6	46.8	542	2.9
15H*†	118.4	120	0.6	533	0.18	25.23	2.28	1.5	9.9	47.5	8.9	11.4	84.3	4.4	615	60.5
17H	137.4	32	1.0	560	0.18	22.08	0.66	4.4	11.4	46.6	8.0	3.0	73.7	23.2	550	3.3
19H	147.9	16	1.0	559	0.18	18.83	1.13	3.7	12.1	41.9	7.4	1.5	62.9	35.7	539	3.0
25P	202.4	3	1.2	562	0.18	27.03	1.09	4.7	12.8	49.2	9.4	0.3	90.3	9.5	402	18.9
31X	240.9	6	1.2	576	0.18	29.22	1.26	0.5	10.8	55.0	11.0	0.6	97.6	1.9	494	104.1
41X	318.7	7	1.3	579	0.18	29.34	1.18	0.5	10.7	55.4	10.6	0.6	98.0	1.4	706	109.6
44X	346.7	7	1.3	576	0.18	28.52	1.10	3.5	11.1	53.5	10.5	0.6	95.2	4.1	550	37.7
48X	385.3	5	1.2	577	0.18	28.56	2.65	3.9	11.1	53.6	10.4	0.5	95.4	4.2	556	88.2
Seawater		0		580	0.18	29.95	0.18	0.0	10.8	56.1	10.9					

Notes: The initial coil water is distilled water with ~1000 ppm LiCl. The seawater concentration for SO₄²⁻ is taken as 580 mM. * = Cl⁻ values have been corrected for dilution by seawater and coil water. † = Fisseler Water Sampler sample.

Table 12. Composition of headspace gas in sediment from Site 997.

Core, section	Depth (mbsf)	C ₁ (ppmv)	C ₂ (ppmv)	C ₁ /C ₂	C ₁	C ₂
					(μL/kg wet sediment)	(μL/kg wet sediment)
164-997A-						
1H-2	1.50	3.5	0.1	35	22	1
2H-4	7.40	10	0.1	100	37	0
3H-4	16.90	43.2	0.3	173	139	1
4H-4	26.40	9,800	1.0	9,850	31,500	3
5H-4	35.90	27,300	1.7	16,000	89,500	6
6H-4	45.40	39,000	2.4	16,300	93,300	6
7H-1	50.40	56,200	2.9	19,400	180,000	9
8H-2	54.40	30,400	1.8	16,900	98,600	6
9H-4	65.90	25,300	1.4	18,100	76,300	4
10H-4	75.25	31,700	2.2	14,400	96,600	7

Notes: C₁ through C₆ = the alkanes: methane, ethane, propane, butane, pentane, and hexane. C₁/C₂ = the methane/ethane ratio, and C₁/C₂₊₆ = the ratio of methane/Σ (C₂ through C₆).

Only part of this table is produced here. The entire table appears on the CD-ROM (back pocket).

idues are <1 mm in diameter. In addition, a strong aromatic odor accompanied each core. These observations suggest that small amounts of liquid hydrocarbons have migrated into these sediments.

The TOC content of sediment from 4.90 to 96.49 mbsf is typically below 1% and averages 0.82% (Table 15; Fig. 26). The average TOC content of sediment from 105.27 to 717.09 mbsf was 1.38%. A maximum value of 2.32% was measured at a depth of 232.90 mbsf. The C/N ratios generally are less than 10. The TOC and carbonate contents are quite uniform from a depth of 124.90 mbsf to the bottom of the hole. Hydrogen indices (HI) from Rock-Eval pyrolysis range from 68 to 152. Oxygen indices (OI) range from 77 to 251. The average T_{max} value is 422°C (Table 16). Total sulfur content varies from 0.25% to 2.11% (Table 15), with poor correlation to TOC content.

Discussion

The highest headspace C₁ concentrations occur between 35.93 and 65.93 mbsf (180,240 mL/kg), whereas headspace gas of sediment below this depth has lower C₁ concentrations. The increase in C₁ reflects methanogenesis below the SO₄²⁻ reduction zone. Comparable headspace concentration vs. depth profiles have been observed at other ODP sites (e.g., at Site 688 [Kvenvolden and Kastner, 1990]). The decline in C₁ below 50.50 mbsf also might be an artifact of the headspace-sampling technique (see "Organic Geochemistry" section, "Site 994" chapter, this volume).

The methane/ethane ratios (>10,000) in the gas samples above ~300 mbsf indicate that the gases are largely of a microbial origin. Deflections in gas-ratio profiles (Figs. 23, 24) roughly coincide with

the base of the gas hydrate-bearing zone. Below this depth, a proportion of the gas may be of a thermogenic origin.

The C₄ through C₆ hydrocarbons in free-gas samples below 460 mbsf are produced by thermogenesis. Because the bottom-hole temperature of 20°C (see "In Situ Temperature Measurements" section, this chapter) is not sufficient to generate C₄ through C₆ hydrocarbons, migration from below must occur. Because 464 mbsf is the approximate depth of the BSR (see "Synthesis and Significance" section, this chapter), gas hydrate may act as a seal for higher molecular weight hydrocarbons and liquid hydrocarbons.

Preliminary CNS analysis of organic matter from Site 997 sediment suggests a marine origin (C/N ratios less than 10). Low HI values (mean value of 97 mg/g of C) and high OI values (mean value of 149 mg/g of C) from Rock-Eval pyrolysis of samples from 18.89 to 429.77 mbsf suggest a type III kerogen. Because this is inconsistent with C/N results, the origin of organic matter cannot be evaluated without further data. The average T_{max} value of 422°C (without an outlier of 314°C) is indicative of low-maturity organic matter. A slight increase of the T_{max} values with depth from ~410° to ~425°C indicates an approach to the zone of thermogenesis. This stage of maturity cannot be explained with present-day bottom-hole temperatures, and substantial amounts of thermogenic hydrocarbons are not expected to be generated in situ from sediment drilled at Site 997.

INORGANIC GEOCHEMISTRY

Sediment at Site 997 was sampled for interstitial water in the same manner as at Sites 994 and 995 (see "Inorganic Geochemistry" sections, "Site 994" and "Site 995" chapters, this volume). At Site 997, 122 interstitial-water samples were analyzed (Table 17). Chemistry data for surface seawater, for nine WSTP runs, for one FWS run, and for the PCS are presented in the "Downhole Tools and Sampling" section (this chapter).

Interstitial-Water Chemistry Trends

Chloride concentration increases with depth from 559 mM at 1.45 mbsf to 562 mM at 10.30 mbsf. The Cl⁻ gradient in this depth range is ~0.30 mM/m. Chloride steadily decreases below 17.85 mbsf to a value of 518 mM at 179.57 mbsf. Between 179.57 mbsf and 451.65 mbsf, there is a zone of significant Cl⁻ variation. There is a baseline concentration of ~500 mM with superimposed Cl⁻ excursions to significantly lower values (to 391 mM). Chloride concentrations below 467.45 mbsf average ~512 mM.

Sulfate decreases from 26.8 mM at 1.45 mbsf to <0.2 mM at the base of the SO₄²⁻ reduction zone at ~23 mbsf (Fig. 27). Below this depth, SO₄²⁻ is considered to be contamination from borehole water.

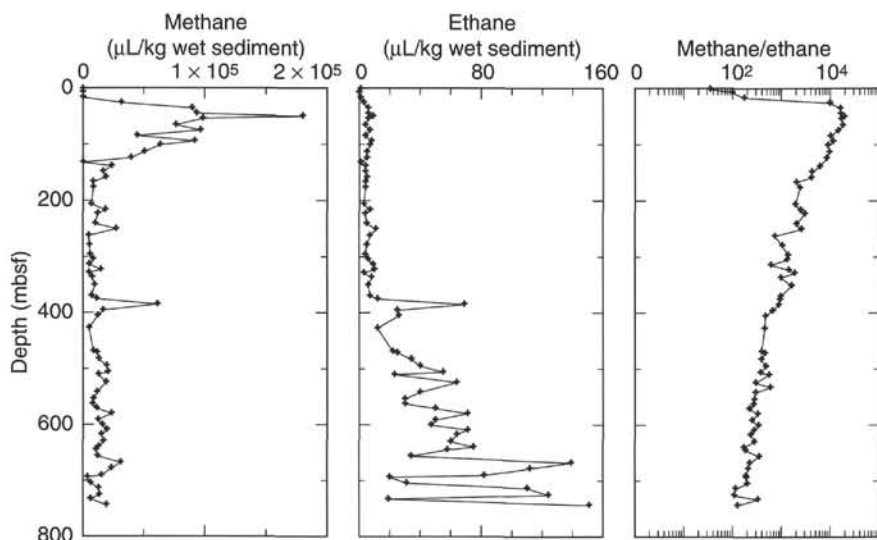


Figure 22. Headspace gas concentrations of C₁ and C₂, and C₁/C₂ ratios in sediment from Site 997.

Table 13. Composition of free gas collected in syringes from sediment from Site 997.

Core, section	Depth (mbsf)	O ₂ (ppmv)	N ₂ (ppmv)	CO ₂ (ppmv)	C ₁ (ppmv)	C ₂ (ppmv)	C ₃ (ppmv)	<i>i</i> -C ₄ (ppmv)	<i>n</i> -C ₄ (ppmv)	<i>i</i> -C ₅ (ppmv)	<i>n</i> -C ₅ (ppmv)	<i>i</i> -C ₆ (ppmv)	<i>n</i> -C ₆ (ppmv)	<i>n</i> -C ₇ (ppmv)	C ₁ /C ₂	C ₁ /C ₂₊
164-997A-																
6H-7	50.00	24,000	196,000	16,400	769,400	31.2	10.6	5.6	0.6	0.6					24,700	15,800
7H-1	50.50	13,000	79,000	23,100	868,900	34.3	10.6	5.2	0.3	0.4					25,300	17,100
8H-2	54.50	72,000	313,000	23,600	568,700	19.4	7.1	3.6	0.3	0.5					29,300	18,400
9H-1	61.50	2,000	23,000	27,100	926,700	35.7	13.1	7.2	0.9	1.0	0.2				26,000	16,000
10H-7	79.85	4,000	25,000	48,400	904,700	34.8	13.3	8.8	0.9	2.2	0.1	0.1			26,000	15,000
11H-3	83.50	80	8,000	32,600	949,900	32.3	12.1	7.9	0.9	2.2		0.1			29,400	17,100
12H-6	97.42	1,000	7,000	34,500	917,700	32.1	13.0	11.4	1.1	3.2	0.2	0.1			28,600	15,000
13H-7	107.58	80	2,000	47,600	910,600	34.3	17.5	15.0	1.6	7.3	0.2	0.1			26,500	12,000
14H-7	116.83	60	1,000	30,400	957,500	31.4	16.0	14.6	1.8	8.0	0.2	0.1			30,500	13,300
16H-5	134.00	8,000	29,000	34,700	760,300	27.0	18.6	12.5	1.2	7.9	0.5				28,200	11,200

Notes: Oxygen (O₂) and nitrogen (N₂) concentrations are included as a guide to the amount of air contamination in each sample. C₁ through C₇ = the alkanes: methane, ethane, propane, butane, pentane, hexane, and heptane. Iso- and normal configurations of butane, pentane, and hexane are designated with *i*- and *n*- prefixes. C₁/C₂ = the methane/ethane ratio, and C₁/C₂₊ = the ratio methane/Σ (C₂ through C₆).

Only part of this table is produced here. The entire table appears on the CD-ROM (back pocket).

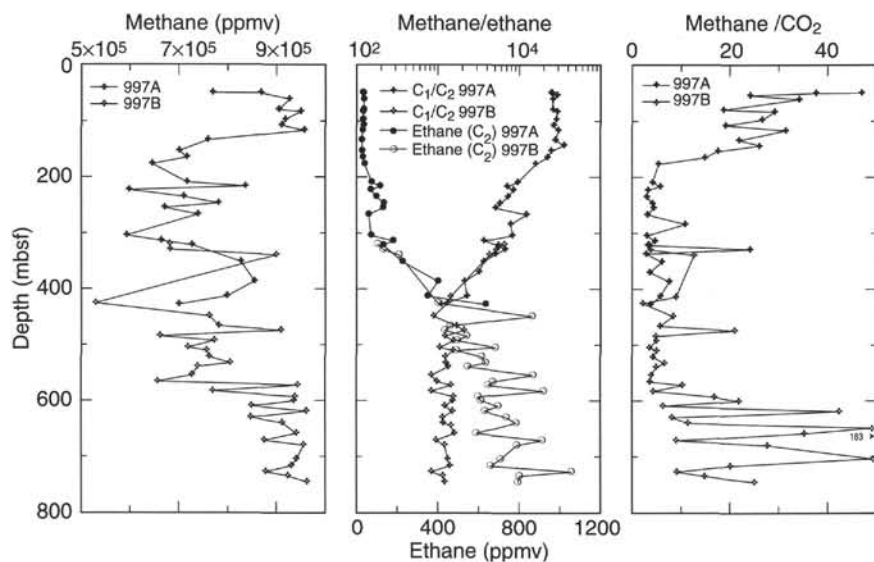


Figure 23. C₁ concentrations and C₁/C₂ and C₁/CO₂ ratios of free gas collected in syringes from Site 997.

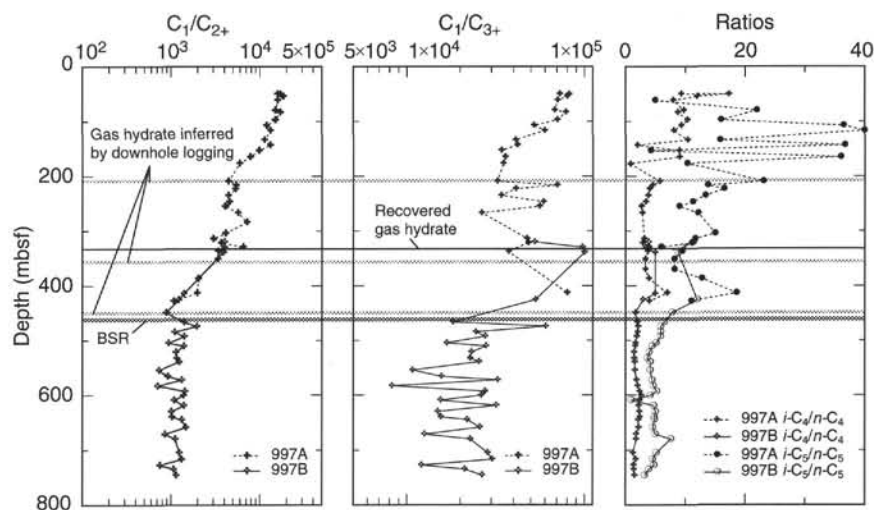


Figure 24. Ratios vs. depth profiles of iso-/n-butane, iso-/n-pentane, C_1 /sum of C_2 through C_6 , and C_1 /sum of C_3 through C_6 . Lines through the graphs denote accumulations of gas hydrate inferred by the downhole logging results, recovered gas hydrate, or the BSR as shown.

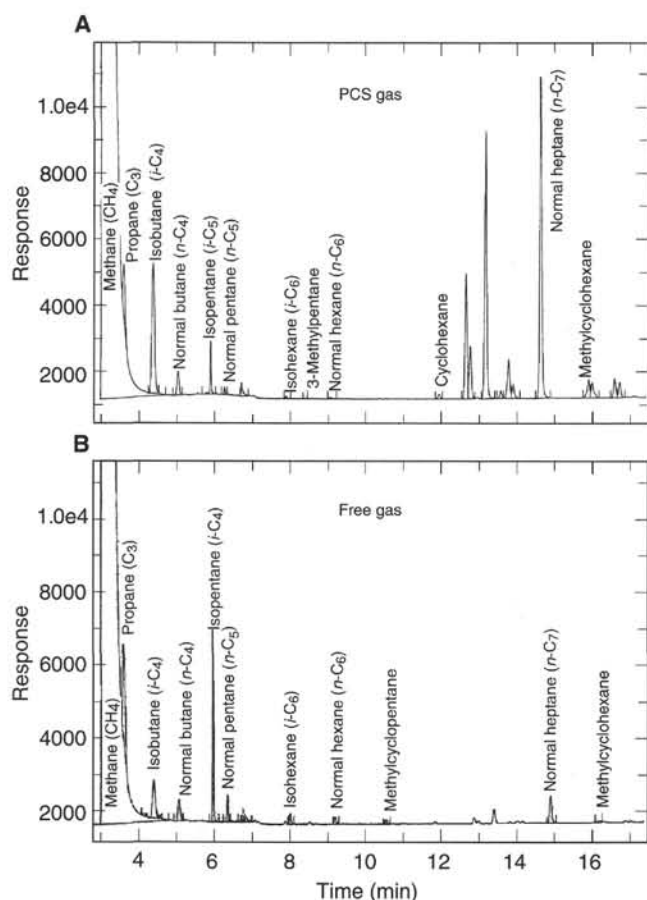


Figure 25. Gas chromatograms of a free gas collected (A) by the PCS (fourth withdrawal) at 462.7 mbsf and (B) in a vacutainer from 465.3 mbsf. Hydrocarbons from C_3 through C_7 are present in parts per million quantities in both gases, however, in very different concentrations.

Alkalinity steadily increases from 4.0 mM at 1.45 mbsf to 112.0 mM at 204.75 mbsf, with a slight change in rate at the base of the SO_4^{2-} reduction zone (Fig. 27). Alkalinity then increases more slowly with depth and reaches a maximum of 126 mM at 315.35 mbsf. From 300 to 450 mbsf, alkalinity values are more variable but generally decrease with depth. Below 480 mbsf, alkalinity decreases linearly from ~103 to 56.8 mM at 737.49 mbsf.

Ammonium increases linearly from 0.14 mM at 1.45 mbsf to 15.6 mM at 169.75 mbsf (Fig. 27). The values continue to increase with scatter from ~200 to 510 mbsf and reach a maximum value of 22.3 mM at 507.55 mbsf. Ammonium then decreases irregularly with depth to the bottom of the hole.

Potassium increases from 12.5 mM at 1.45 mbsf to 14.6 mM at 169.75 mbsf (Fig. 27). Values are more variable from 200 to 460 mbsf with a maximum of 15.4 mM at 473.86 mbsf (excepting the anomalous Sample 164-997B-3X-3, 125–150). Potassium decreases with depth below ~475 mbsf to a minimum value of 12 mM at 746.85 mbsf.

Calcium decreases from 10.3 mM near the sediment/water interface to 2 mM at 92.80 mbsf (Fig. 27). A Ca^{2+} maxima of 2.7 mM occurs at 153.08 mbsf. Below this depth, Ca^{2+} reaches baseline values of ~2 mM to 400 mbsf. Calcium increases with depth from 400 mbsf to 8.5 mM at 746.85 mbsf.

Concentrations of Mg^{2+} also decrease from the shallowest sample (50.2 mM; 1.45 mbsf) to reach 22.4 mM at 55.80 mbsf (Fig. 27). From this depth, Mg^{2+} decreases linearly to reach 13.6 mM at 426.31 mbsf. Magnesium ranges between 13.3 and 16.2 mM from 467.45 to 746.85 mbsf.

Strontium increases from 94 μM at 1.45 mbsf to 130 μM at 26.30 mbsf (Fig. 27). Concentrations then decrease to 79 μM at 121.31 mbsf and are scattered around a baseline value of ~80 μM between 121.31 and 426.31 mbsf. Below this depth, Sr^{2+} generally increases with depth to 175 μM at the bottom of the hole.

Phosphate increases in a roughly linear fashion from 11 μM at 1.45 mbsf to 215 μM at 179.57 mbsf (Fig. 27). Concentrations then decrease slowly with depth to 19 μM at 628.38 mbsf. Phosphate continues to decrease with depth to 5 mM at 746.86 mbsf.

Silica concentrations display more scatter than other pore-water species but generally increase with depth to ~600 mbsf (Fig. 27). The maximum value (1171 μM) occurs at 445.75 mbsf. A local minima in SiO_2 (911 μM) occurs at 737.49 mbsf.

Geochemical Similarity of Interstitial-Water Chemistries at the Blake Ridge Sites

Downhole profiles of all interstitial species (Figs. 27, 28) are similar to those observed at the other Blake Ridge sites. However, absolute concentrations of some species differ between sites.

The Cl^- gradient in uppermost samples at Site 997 is slightly lower than those observed at Sites 994 and 995. This may be an analytical artifact given the ~1% error in Cl^- measurements.

Chloride profiles at Sites 995 and 997 diverge from those at Site 994 toward lower Cl^- concentrations below ~40 mbsf. The Cl^- profile at Site 994 is nearly linear between ~40 and 180 mbsf; the profiles at

Table 14. Composition of gas collected in gas-collection chambers, Site 997.

Core, section	Sample	Depth (mbsf)	O ₂ (ppmv)	N ₂ (ppmv)	C ₁ (ppmv)	CO ₂ (ppmv)	C ₂ (ppmv)	C ₃ (ppmv)	<i>i</i> -C ₄ (ppmv)	<i>n</i> -C ₄ (ppmv)	<i>i</i> -C ₅ (ppmv)	<i>n</i> -C ₅ (ppmv)	<i>i</i> -C ₆ (ppmv)	<i>n</i> -C ₆ (ppmv)	C ₁ /C ₂	C ₁ /C ₂₊
164-997A-																
4H-3	50	25.40	136,000	588,000	219,000	5,400	10.8	4.0	2.0	0.2	0.4	0.3	0.1		20,300	12,300
4H-3	41	25.40	58,000	250,000	627,400	36,600	25.6	10.0	6.5	0.8	1.7	0.1	0.1		24,500	14,000
5H-3	65	34.90	161,000	684,000	120,600	3,200	5.1	2.0	1.0		0.1	0.2	0.1		23,600	14,200
5H-3	34	34.90	164,000	693,000	121,800	3,200	5.0	2.0	1.0		0.1	0.1			24,400	14,900
5H-3	19	34.90	131,000	569,000	238,500	5,800	11.9	4.6	2.2		0.1				20,000	12,700
6H-3	100	44.40	112,000	478,000	356,200	7,100	14.9	5.0	2.2	0.2	0.1	0.1			23,900	15,800
6H-3	2	44.40	115,000	499,000	241,900	5,500	10.0	5.0	0.9	0.1		0.3			24,200	14,800
6H-3	17	44.40	151,000	632,000	153,200	3,600	13.2	2.0	0.9		0.6	0.6			11,600	8,860
8H-3	67	56.40	122,000	510,000	306,800	7,300	30.5	4.0	2.2		0.5				10,100	8,250
8H-3	38	56.40	121,000	505,000	307,700	7,300	30.2	4.1	2.1	0.2	0.6	0.1	0.1		10,200	8,230

Notes: Oxygen (O₂) and nitrogen (N₂) concentrations are included as a guide to the amount of air contamination in each sample. C₁ through C₆ = the alkanes: methane, ethane, propane, butane, pentane, and hexane. Iso- and normal configurations of butane, pentane, and hexane are designated with *i*- and *n*- prefixes. C₁/C₂ = the methane/ethane ratio, and C₁/C₂₊ = the ratio of methane/Σ (C₂ through C₆).

Only part of this table is produced here. The entire table appears on the CD-ROM (back pocket).

Table 15. Carbonate, carbon, nitrogen, and sulfur contents in sediments from Site 997.

Core, section, interval (cm)	Depth (mbsf)	CaCO ₃ (wt%)	Organic carbon (wt%)	Total nitrogen (wt%)	C/N	Total sulfur (wt%)
164-997A-						
1H-1, 35–36	0.35	45.7	NA	NA	NA	NA
2H-1, 71–72	3.61	50.6	NA	NA	NA	NA
2H-2, 50–51	4.90	31.5	0.74	0.08	9.4	0.25
2H-5, 50–51	9.40	20.3	NA	NA	NA	NA
3H-2, 49–50	14.39	24.2	NA	NA	NA	NA
3H-4, 63–64	17.53	28.5	NA	NA	NA	NA
3H-5, 49–50	18.89	33.5	0.90	0.09	10.0	0.56
4H-2, 49–50	23.89	26.8	NA	NA	NA	NA
4H-5, 49–50	28.39	16.2	0.64	0.07	9.1	0.80
5H-2, 49–50	33.39	17.0	NA	NA	NA	NA

Note: NA = not analyzed.

Only part of this table is produced here. The entire table appears on the CD-ROM (back pocket).

Sites 995 and 997 show increasing amounts of curvature. From ~140 to 180 mbsf, the Cl⁻ trends for all three sites are similar.

Chloride values exhibit excursions toward less-saline values between ~220 and 460 mbsf at the three sites. These excursions represent intervals with anomalously high concentrations of hydrate (see “Inorganic Geochemistry” section, “Site 994” chapter, this volume). The uppermost excursion toward fresher Cl⁻ values occurs between 194.95 and 209.20 mbsf at Site 994, between 190.25 and 195.35 mbsf at Site 995, and between 179.57 and 204.75 mbsf at Site 997. The lowermost excursion in Cl⁻ occurs between 427.37 and 439.50 mbsf at Site 994, between 438.00 and 465.12 mbsf at Site 995, and between 451.65 and 467.45 mbsf at Site 997. Thus, the depth range with significant hydrate increases from Site 994 to Site 995 to Site 997. The amount of hydrate within this zone also appears to increase from Site 994 to Site 995 to 997 because the average magnitude of Cl⁻ excursions at these sites increases from 15 to 18 to 21 mM. The above interpretations are consistent with other proxies for gas hydrate occurrence (see “Synthesis and Significance” section, this chapter).

Below ~475 mbsf, the trends from all the Blake Ridge sites are similar, although Site 994 data tend to have slightly higher Cl⁻ values. Site 997 displays the lowest corrected Cl⁻ concentrations (508–511 mM) of the three sites below ~600 mbsf.

Alkalinity and PO₄³⁻ increase in concentration from the ridge flank to the ridge crest, whereas NH₄⁺ has an opposite trend. Maximum alkalinity at Site 997 (~128 mM) is ~6% and 18% higher than at Sites 995 and 994, respectively. Maximum PO₄³⁻ concentrations at Site 997 are ~5% and 30% greater than at Sites 995 and 994. Maximum NH₄⁺ levels at Site 994 are ~11% and 21% greater than at Sites

995 and 997, respectively. Calcium, Mg²⁺, and Sr²⁺ do not differ significantly between the Blake Ridge sites. Silica values generally are similar at each site, although the scatter of data is high. Strontium shows little variation in shallow sediment above 100 mbsf at each site. Strontium at 500 mbsf is higher at Site 995 than 997, but lower at Site 995 below ~540 mbsf.

WSTP Data

Corrected Cl⁻ concentrations in the WSTP water samples (see “Downhole Tools and Sampling” section, this chapter) are broadly consistent (within analytical uncertainty) with baseline concentrations of interstitial-water values from corresponding depths. WSTP samples from 75 to 150 mbsf have a tendency toward more saline values and plot off the Cl⁻ baseline. In the chloride excursion zone (218–460 mbsf), three of four WSTP Cl⁻ values plot on or near the Cl⁻ baseline.

Preliminary Interpretations

Chloride profiles have been used as a proxy of the amount of in situ gas hydrate, particularly within the chloride excursion zone (see “Inorganic Geochemistry” sections, “Site 994” and “Site 995” chapters, this volume). The Cl⁻ excursion zone occurs at approximately the same depths (~200–440 mbsf) over the ~10-km transect. Furthermore, the depth intervals showing the largest Cl⁻ excursions, at ~250, 320, and 400 mbsf, are depth correlative. Thus, the similarity of the Cl⁻ profiles at the ridge sites strongly suggests that gas hydrate is areally correlative over the expanse of the Blake Ridge. As pointed out in the “Site 995” chapter (this volume), these depth correlative zones occur despite the absence of a BSR at Site 994.

PHYSICAL PROPERTIES

Physical properties measurements were performed on both unsplit and split cores recovered at Site 997. The MST was used to measure GRAPE wet bulk density, magnetic susceptibility, and NGR activity at high resolution. Separation of sediments from the core liner made it impossible to obtain useful data from the PWL on cores recovered at depths greater than 30 mbsf. When possible, *P*-wave velocities were measured at discrete locations in split sections using the DSV. Undrained shear strength and unconfined compressive strength were determined using the vane shear apparatus and a pocket penetrometer, respectively. Index properties were measured using samples from two to three sections per core, including samples from the PCS. Because of instrument failure, thermal conductivity data could only be obtained in cores recovered at depths shallower than 150 mbsf. All

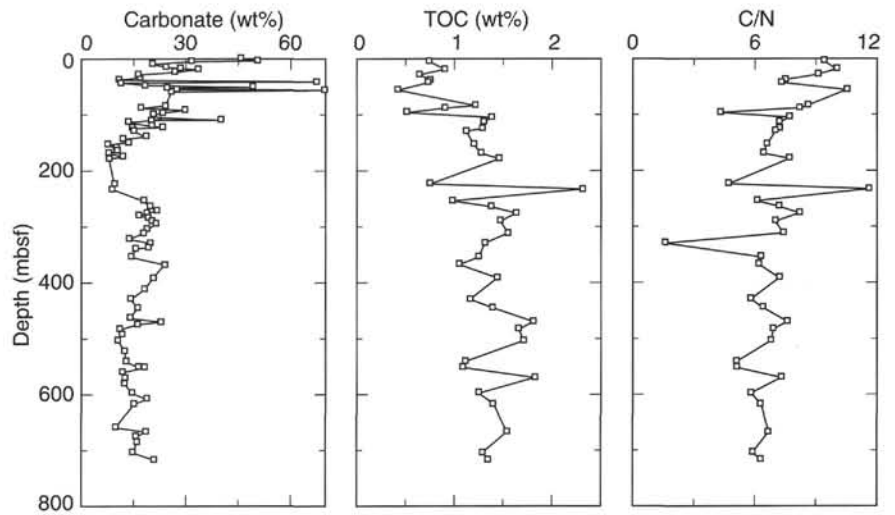


Figure 26. Content of carbonate and total organic carbon, and C/N ratios in sediment from Site 997. A C/N ratio of 10 or lower is indicative of marine organic matter; ratios higher than 20 are representative of terrestrial organic matter.

Table 16. Rock-Eval analysis of sediment from Site 997.

Core, section, interval (cm)	Depth (mbsf)	T _{max}	S ₁	S ₂	S ₃	PI	HI	OI
164-997A-								
3H-5, 49-50	18.89	402	0.22	0.83	2.26	0.21	92	251
5H-5, 49-50	37.89	314	0.22	0.77	1.34	0.22	102	178
7H-2, 50-51	52.40	411	0.31	0.99	2.23	0.24	72	163
11H-3, 70-71	84.10	422	0.10	0.83	1.86	0.11	68	153
13H-5, 79-80	105.27	427	0.13	1.45	2.02	0.08	105	146
14H-5, 50-51	114.23	408	0.19	1.33	2.07	0.12	102	159
16H-2, 50-51	129.90	423	0.03	0.52	1.65	0.06	46	147
19H-5, 50-51	153.73	421	0.09	1.10	1.65	0.08	91	137
22X-5, 50-51	178.72	424	0.11	1.39	1.84	0.07	95	126
30X-1, 60-61	232.90	425	0.09	1.82	1.81	0.05	78	77
34X-3, 39-40	264.42	425	0.06	1.29	2.06	0.04	94	150
35X-5, 50-51	275.95	430	0.07	1.68	2.04	0.04	103	125
37X-2, 40-41	290.80	421	0.06	1.51	2.77	0.04	102	188
39X-3, 70-71	311.80	431	0.14	2.37	1.89	0.06	152	121
44X-6, 39-40	354.62	430	0.04	1.18	1.59	0.03	94	127
48X-5, 39-40	391.69	418	0.18	2.17	2.23	0.08	150	154
54X-5, 39-40	429.77	427	0.10	1.22	1.52	0.08	105	131

Notes: T_{max} = temperature (°C) at which the maximum amount of hydrocarbons is generated from the kerogen during pyrolysis; S₁ = quantity of free hydrocarbons in the rock samples, in mg/g rock; S₂ = quantity of hydrocarbons produced by kerogen cracking, in mg/g rock; S₃ = quantity of organic CO₂ produced during pyrolysis of the rock, in mg/g rock; PI = production index, calculated as S₁/S₁+S₂; HI = hydrogen index, calculated as S₂/TOC; and OI = oxygen index, calculated as S₃/TOC.

Table 17. Interstitial-water chemistry data for Site 997.

Core, section, interval (cm)	Depth (mbsf)	pH	Alk (mM)	Sal (g/kg)	Cl ⁻ (mM)	Cl ⁻ (mM)	Mg ²⁺ (mM)	Ca ²⁺ (mM)	SO ₄ ²⁻ (mM)	NH ₄ ⁺ (μM)	PO ₄ ³⁻ (μM)	SiO ₂ (μM)	K ⁺ (μM)	Sr ²⁺ (μM)
164-997A-														
1H-1, 145-150	1.45	7.7	4.0	34.5	559	559	50.3	10.3	26.78	140	11	445	12.5	94
1H-1, 120-125	2.70	7.7	5.2	34.0	558	558	49.2	9.7	25.1	250	19	589	12.3	93
2H-1, 140-150	4.30	7.8	6.4	34.0	562	562	47.4	8.4	21.5	600	20	603	12.7	96
2H-2, 140-150	5.80	7.8	7.3	33.0	560	560	46.2	7.5	19.7	660	24	652	12.7	98
2H-3, 140-150	7.30	7.9	8.4	33.5	560	560	45.2	7.1	17.8	810	28	645	12.2	100
2H-4, 140-150	8.80	7.9	9.1	33.0	561	561	43.8	6.5	16.4	910	36	741	12.5	105
2H-5, 140-150	10.30	7.4	10.3	33.0	562	562	42.6	6.2	14.7	1,050	34	732	12.3	102
2H-6, 140-150	11.80	8.1	10.9	33.0	561	561	40.9	5.5	13.6	1,150	31	749	12.4	105
3H-1, 140-150	13.80	8.1	12.0	32.5	561	561	39.5	5.3	11.6	1,210	31	705	12.6	110
3H-2, 140-150	15.30	8.2	13.1	32.5	561	561	37.6	4.7	9.6	1,320	36	625	12.5	109

Notes: Alk = alkalinity, and Sal = salinity. Cl⁻ = values have been corrected for seawater contamination (see "Inorganic Geochemistry" section, "Site 994" chapter, this volume) All other concentrations are uncorrected.

Only part of this table is produced here. The entire table appears on the CD-ROM (back pocket).

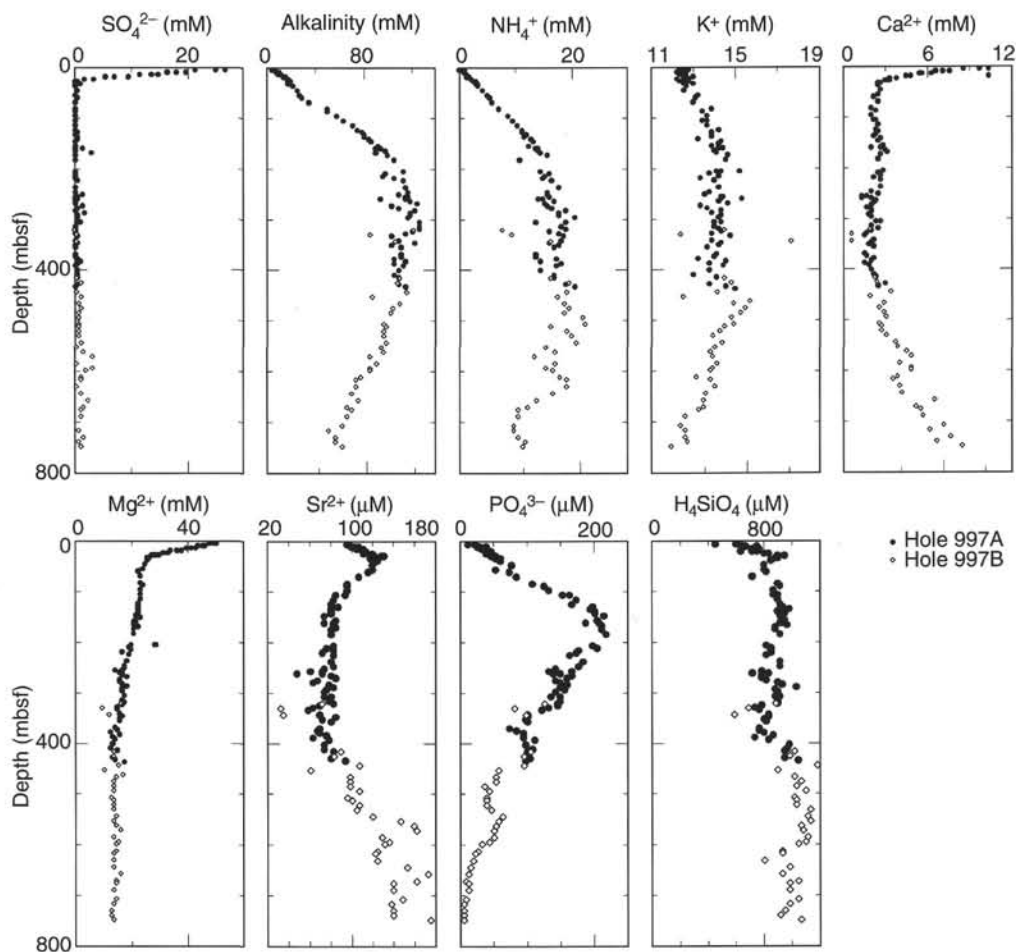


Figure 27. Concentration vs. depth profiles for various chemical species in interstitial waters at Site 997. Values have not been corrected for seawater contamination (see "Inorganic Geochemistry" section, "Site 994" chapter, this volume).

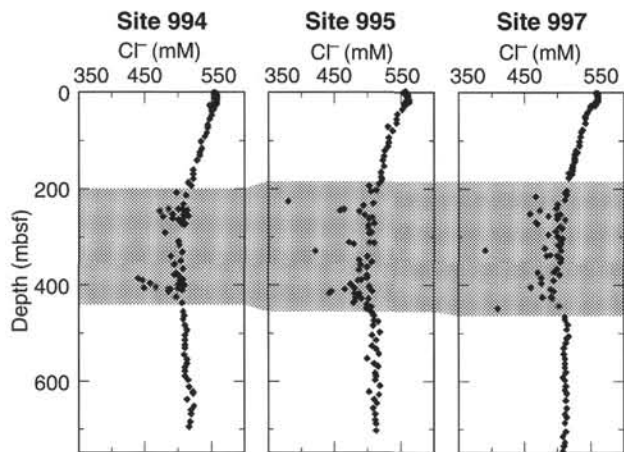


Figure 28. Chloride concentration profiles for interstitial waters. Note the similarity of the profiles. All Cl^- values have been corrected for seawater contamination (see "Inorganic Geochemistry" section, "Site 994" chapter, this volume).

index properties, thermal conductivity, strength, and DSV data for Site 997 are available on CD-ROM (back pocket).

Index Properties

Wet bulk density, porosity, and grain density (Fig. 29) determined from index properties are listed in Table 18. Wet bulk density in-

creases from $\sim 1.43 \text{ g/cm}^3$ near the seafloor to 2.01 g/cm^3 at the bottom of the hole, and the greatest variability in wet bulk density values occurs at depths shallower than 180 mbsf. Wet bulk density is nearly constant between 350 and 600 mbsf but increases with depth below 610 mbsf. The high-resolution GRAPE data yield wet bulk density values that closely match those obtained using gravimetric methods.

Water content measured using both wet and dry methods show a gradual change as a function of depth, with values generally decreasing linearly from 128% to 33% (dry) and from 56% to 25% (wet) with increasing depth. Water content increases from 61% to 73% (wet method) and from 38% to 42% (dry method) between 145 and 178 mbsf. Water content also increases with depth between 55 and 88 mbsf (dry method) and from 625 to 637 mbsf (wet and dry methods).

Porosity decreases from 78% near the top of the hole to 49% at the bottom. Grain density is nearly constant as a function of depth, averaging 2.73 g/cm^3 .

The index properties of sediments recovered from PCS cores were measured only with gravimetric methods. In general, the water content of PCS cores is higher than that of adjacent APC or XCB cores. The elevated water content in PCS cores likely reflects the mode of core recovery rather than the in situ conditions of the sediments. Table 18 lists selected index properties of sediments recovered from all cores at Site 997, but data for the PCS cores are omitted from the plots shown in Figure 29.

Acoustic Velocity

The PWL on the MST recorded realistic velocities only for cores recovered from the uppermost 30 m of Hole 997A. In the interval

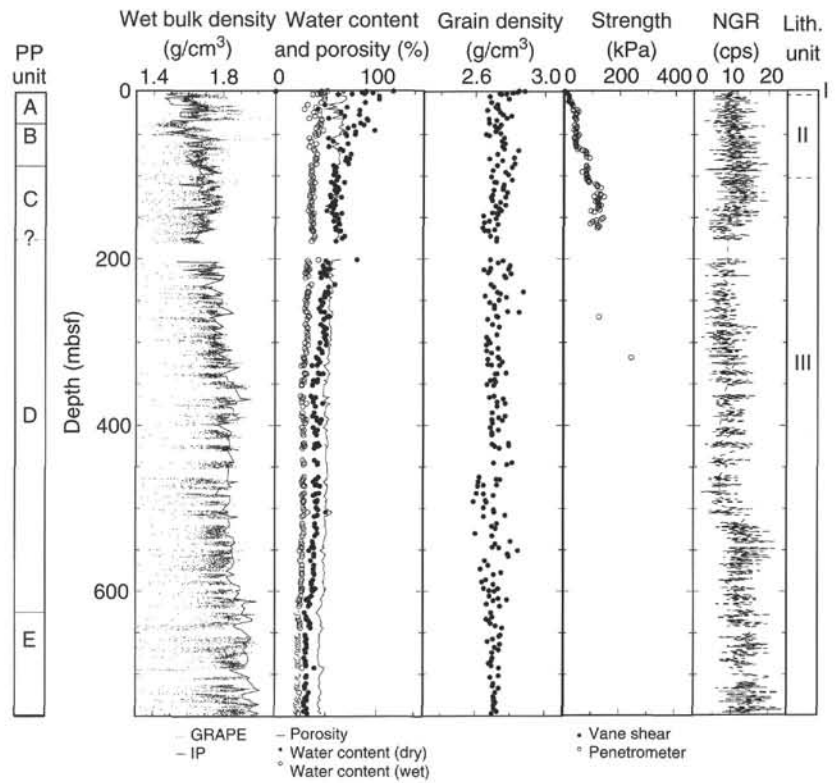


Figure 29. Physical properties data from Holes 997A and 997B. Most data from depths shallower than 433.5 mbsf were obtained in Hole 997A. All data deeper than 433.5 mbsf were collected in cores recovered from Hole 997B. IP = index properties. GRAPE = gamma-ray attenuation porosity evaluator data. The grain density data were calculated using the dry method (see “Physical Properties” section, “Explanatory Notes” chapter, this volume). NGR = natural gamma radiation in average counts per second. Physical properties units are shown on the left; lithostratigraphic units, on the right. The lower boundary of Unit C could be as shallow as 177 mbsf or as deep as 200 mbsf.

Table 18. Index properties of sediment samples from Site 997.

Core, section, interval (cm)	Depth (mbsf)	Water content (wet%)	Water content (dry%)	Density			Porosity (%)	Void ratio
				Bulk (g/cm ³)	Grain (g/cm ³)	Dry (g/cm ³)		
164-997A-								
1H-1, 11–13	0.11	56.07	127.64	1.43	2.85	0.63	78.31	3.55
1H-1, 55–57	0.55	49.50	98.02	1.51	2.88	0.76	72.72	2.76
1H-1, 133–135	1.33	48.30	93.43	1.52	2.84	0.79	71.59	2.59
1H-2, 73–75	2.23	51.28	105.27	1.48	2.81	0.72	74.12	2.89
2H-1, 33–35	3.23	49.10	96.47	1.52	2.73	0.77	72.65	2.58
2H-1, 71–73	3.61	45.23	82.59	1.57	2.77	0.86	69.15	2.24
2H-1, 125–127	4.15	40.38	67.72	1.66	2.74	0.99	65.54	1.81
2H-3, 64–66	6.54	52.90	112.29	1.47	2.68	0.69	75.69	2.94
2H-5, 73–75	9.63	52.94	112.50	1.49	2.79	0.70	76.86	3.06
3H-1, 121–123	13.61	49.28	97.16	1.50	2.69	0.76	71.94	2.55

Only part of this table is produced here. The entire table appears on the CD-ROM (back pocket).

from 0 to 5 mbsf, *P*-wave velocities increase with depth from 1.48 km/s at 1 mbsf to 1.52 km/s at 5 mbsf (Fig. 30). Velocity decreases to 1.48 km/s at 6 mbsf and increases gradually with depth to 22 mbsf, the last depth at which reliable data were obtained.

Acoustic velocities also were measured with the DSV frame on split sections of cores recovered between 0 and 33 mbsf. The DSV data closely match the PWL results in the uppermost 14 m but are scattered widely about the average PWL values even at depths at which the PWL data are reliable.

Undrained Shear Strength

Data obtained with a pocket penetrometer and the vane shear apparatus are consistent with a general increase in strength as a function of depth from 0 to 170 mbsf. The data indicate that strength is relatively constant between 30 and 70 mbsf (39 kPa), 80 and 105 mbsf

(69 kPa), and 120 and 165 mbsf (109 kPa), imparting the strength curve with a staircase pattern.

Natural Gamma Radiation

Because of frequent incomplete core recovery at Site 997, the NGR data were too discontinuous to permit filtering. The average NGR value increases from 9 to 14 cps with depth to ~120 mbsf. From 170 to 500 mbsf, NGR averages 7–10 cps. At 500 mbsf, NGR abruptly increases to an average value of 15 cps to the bottom of the hole.

Thermal Conductivity

Thermal conductivity varies between 0.81 and 1.21 W/(m·K) in APC cores recovered from Hole 997A (Fig. 31). The data are scattered, with the greatest local variability occurring shallower than 60

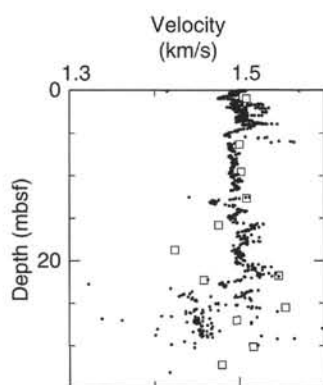


Figure 30. *P*-wave velocities recorded in sediments recovered from Hole 997A. Circles = high-resolution PWL data. Open squares = data obtained using the DSV apparatus. No reliable data were collected for sediments recovered deeper in Hole 997A.

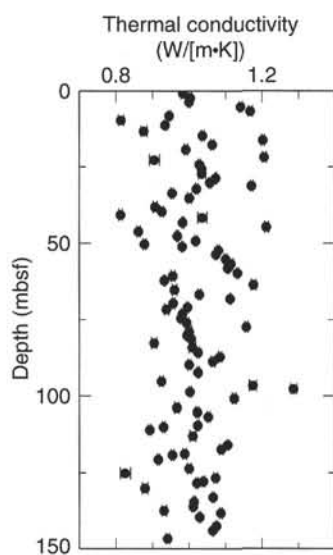


Figure 31. Thermal conductivity measurements obtained in sediments recovered in APC cores from Hole 997A. Error bars indicate analytical uncertainty. Because of instrument failure, data collected in cores recovered below 150 mbsf had to be discarded.

mbsf. Conductivity averages 1.01 W/(m·K), and the most consistent trend in the data occurs between 72 and 87 mbsf, where conductivity increases linearly with depth.

Physical Properties Units

The physical properties data were used to define five units at Site 997 (Fig. 29). Unit A, which extends from 0 to 37 mbsf, is characterized by wet bulk density that increases with depth to 20 mbsf and then decreases to the base of the unit. Porosity and water content vary widely within the unit but generally decrease with depth. The lower boundary of Unit A is marked by a minimum in wet bulk density values. Unit B (37–88 mbsf) has generally increasing wet bulk density with depth. Water content (wet method) decreases with depth in the uppermost 15 m of Unit B and increases with depth between 57 and 88. Unit C (88–177 mbsf) is distinguished from Unit B on the basis of an offset to lower water content and porosity values at 88 mbsf.

The precise location of the bottom of Unit C was arbitrarily defined to be at 177 mbsf. Within Unit C, water content and porosity are constant to 145 mbsf and increase between 145 and 177 mbsf. Unit D (177(?)–625 mbsf) has wet bulk density that increases gradually with depth, and porosity and water content that decrease with depth to 350 mbsf. At depths greater than 350 mbsf, porosity and water content are nearly constant. The top of Unit E (625–750 mbsf) is marked by a change in the slope of the wet bulk density curve and an interval of increasing water content with depth.

Discussion

Lithostratigraphic and physical properties units are not correlative at Site 997. However, localized variations in physical properties can in some cases be related to downhole changes in carbonate content and the abundance of diatoms. For example, a weak peak in GRAPE wet bulk density data between 52 and 57 mbsf correlates with a carbonate-rich layer, and the interval of increasing water content and porosity with depth in the bottom part of Unit C may reflect the higher diatom content of the sediments in this part of the hole. Other intervals of increasing water content with depth (50–88 mbsf and 625–637 mbsf) at Site 997 cannot be explained on the basis of systematic variations in mineralogy, lithology, or diatom content. The change from decreasing to constant water content as a function of depth at 350 mbsf within Unit D corresponds to a hiatus (see “Biostratigraphy” section, this chapter).

A sediment sample obtained adjacent to a gas hydrate nodule recovered at 331 mbsf in Hole 997A had significantly lower water content (40% using the dry method) than sediments in adjacent core sections (46%–52% using the dry method). The formation of the gas hydrate nodule may have resulted in dewatering of the surrounding sediment.

The physical properties of sediments at Site 997 are generally similar to those at Sites 994 and 995. Most notably, all three sites have intervals of increasing water content with depth in at least one 50-m-thick section between 50 and 200 mbsf. However, this interval is more pronounced at Sites 994 and 995 than at Site 997. Unit E also is remarkably consistent between the three sites, with its upper boundary defined at 610, 615, and 625 mbsf at Sites 994, 995, and 997, respectively. However, the increase in wet bulk density within Unit E is better defined at Site 994 than at the other sites. A major difference among the Blake Ridge sites is the degree of variability in physical properties within the uppermost 200 m of the sedimentary section. At Sites 994 and 995, step offsets in the wet bulk density curve at discrete depths make it possible to unambiguously delineate unit boundaries. In contrast, the wet bulk density in the uppermost 200 m of Hole 997A is relatively constant compared to Sites 994 and 995, and defining units is much more difficult.

GEOPHYSICS

Vertical Seismic Profile Experiment Design

ZO-VSP data were acquired in Hole 997B in two lowerings of the Geospace Model WLS-1100 three-component borehole seismometer (see “Operations” section, this chapter). During the first lowering, shots from the 300-in³ Bolt PAR1500 air gun were recorded at 68 stations at a nominal spacing of 8 m from 712 to 120 mbsf. During the second lowering, shots from both the air gun and the 400-in³ Seismic Systems P400 water gun were recorded at 64 stations from 684 to 164 mbsf; these stations were positioned between those from the first lowering to provide air gun records at 4-m spacing over most of the hole. Several stations were reoccupied during the second lowering to calibrate depths between the two lowerings.

Preliminary Results

A stacked air gun section shows clear downgoing first arrivals and an upgoing reflection from the BSR (Fig. 32). The depth of the BSR is defined by the intersection of its reflection with the downgoing arrival at 464 ± 8 mbsf.

A preliminary velocity-depth function was produced by inverting the air gun first-arrival times using a weighted, damped, least-squares inversion that weights mean traveltimes by the inverse of their standard error. The velocity-depth curve in Figure 33 was produced by assigning equal weight to fitting the traveltime data and to producing a smooth velocity-depth function. Above the BSR, velocities increase from 1550 m/s at 140 mbsf to 1800 m/s at 430 mbsf, with a peak of 1850 m/s at 360 mbsf. Beneath the BSR, velocities decrease rapidly to a minimum of 1400 m/s at 480 mbsf and remain lower than about 1650 m/s to the base of the hole.

Discussion

The caveats mentioned in the discussion of Site 995 results (see "Geophysics" section, "Site 995" chapter, this volume) also apply here: namely, that the result is an average velocity structure (Fig. 34) that does not include fine-scale structure and that rigorous error

analysis has not yet been carried out. Moreover, these results do not yet include the data from the second lowering, which are of comparable quality.

The principal features of the velocity model for Hole 997B are the sharp velocity decrease across the BSR and the thick underlying zone of low seismic velocities (1400–1650 m/s) from ~450 to 700 mbsf. These velocities provide clear evidence that several percent of the po-

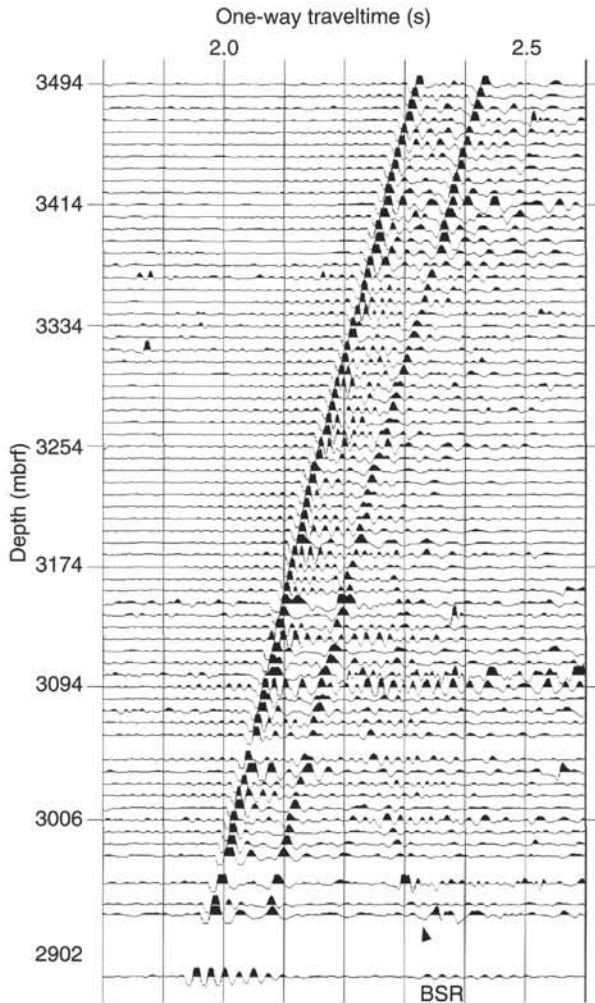


Figure 32. A stacked VSP section from the first lowering in Hole 997B. The reflected arrival from the BSR can be seen intersecting the direct arrival at 464 mbsf (3245 mbsf).

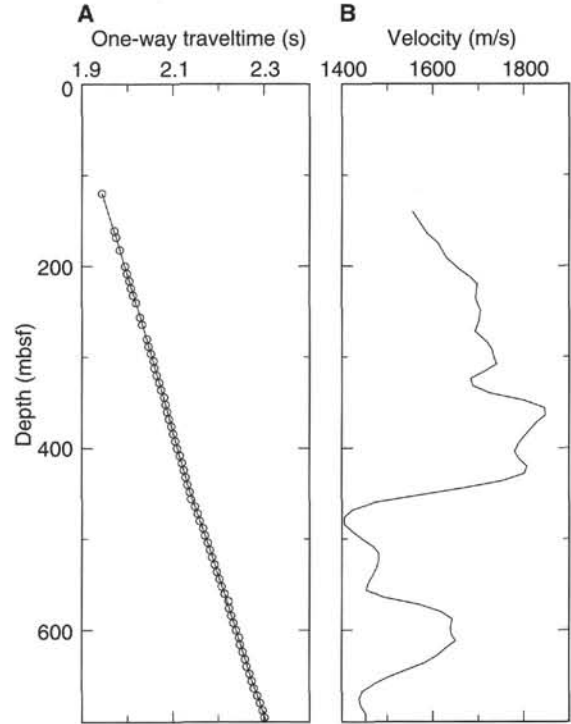


Figure 33. **A.** Plot of depth vs. arrival time for the data of Figure 32. **B.** The resulting velocity profile for Hole 997B. Note the extremely low velocity below the base of hydrate stability at 464 mbsf.

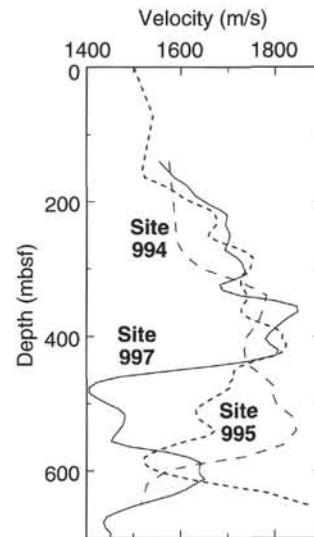


Figure 34. Velocity profiles from Sites 994, 995, and 997 from the flank of the Blake Ridge to the crest show similar, possibly slightly increasing velocities above the hydrate stability zone (~450 mbsf) and a significant decrease in velocity toward the crest below this zone.

rosity is filled with free gas at these depths. The variation of velocity from 1400 to 1650 m/s within this broad zone suggests that the concentration of free gas changes on the scale of 50–100 m. The velocity peak at 360 mbsf appears to be well resolved and may indicate a local concentration of gas hydrate.

Comparison of the velocity-depth functions derived for Sites 994, 995, and 997 shows a clear trend of decreasing sub-BSR velocities, implying that substantially more free gas is present beneath the crest of the Blake Ridge than beneath the flanks (Fig. 34). There is a similar, though less well-resolved, trend toward higher velocities above the BSR, suggesting a slight increase in gas hydrate concentration toward the crest of the ridge.

DOWNHOLE LOGGING

Introduction

The primary objective of the downhole logging program at Site 997 was to obtain in situ physical property and geochemical data from an area where a strong BSR exists. Site 997 was the third core site in a multihole transect (Sites 994, 995, and 997) designed to penetrate below the base of the gas hydrate stability zone within the same stratigraphic interval over a relatively short distance on the Blake Ridge. Site 997 is located at the crest of the Blake Ridge, an area characterized by a strong BSR.

At Site 997, Hole 997B was logged with four different tool strings: (1) the combined seismic stratigraphic and lithoporosity tool strings (Quad-combo), (2) the GLT, (3) the LDEO-SST, and the (4) Formation MicroScanner (for more detail on the logging runs, see “Operations” section, this chapter). The Schlumberger Quad-combo tool string (without the CNT-G) was run over the interval from 113.0 mbsf (base of drill pipe) to 715.0 mbsf, and the depth interval between 115.0 mbsf (base of drill pipe) to 683.0 mbsf was logged with the GLT. In addition to the normal acquisition of capture- τ neutron geochemical data, a series of 13 inelastic neutron geochemical measurements were made. The LDEO-SST also was deployed in Hole 997B, and the depth interval from 235.0 to 675.0 mbsf was successfully logged. The final borehole surveys in Hole 997B consisted of two runs of the Schlumberger Formation MicroScanner within the depth interval between 115.0 and 681.0 mbsf. Hole 997B penetrated a total of 750.0 m of sediment (total hole depth); borehole bridging prevented logging below 715.0 mbsf. The CSES was deployed before logging Hole 997B.

Log Quality

In general, the quality of the log measurements at Site 997 were significantly degraded by the size and rugosity of the borehole. The caliper log in Hole 997B (Fig. 35) shows borehole diameters greater than the 43.7-cm (17.2 in) maximum range of the caliper for a significant portion of the hole.

The NGT and HLDT tools are particularly susceptible to adverse effects from large and irregular hole diameters. The NGT logs from Hole 997B are highly degraded because of borehole size and rugosity, so their use has been limited to depth corrections between log runs and to interpret general lithologic trends. The HLDT, which is a centered device, has a caliper arm that forces the tool against the wall of the borehole. However, if the hole is larger than the maximum reach (43.7 cm) of the caliper arm, the density tool may lose contact with the formation. The density log was significantly degraded in Hole 997B because of poor tool contact with the borehole wall. Data from the density log has been used to assess general lithologic trends but not for porosity calculations. The sonic (SDT/LSS) and resistivity (DITE-SFL) logs provided useful information in Hole 997B; however, both of these devices are affected by the size of the hole and the presence of gas hydrate. The GLT provides useful information; how-

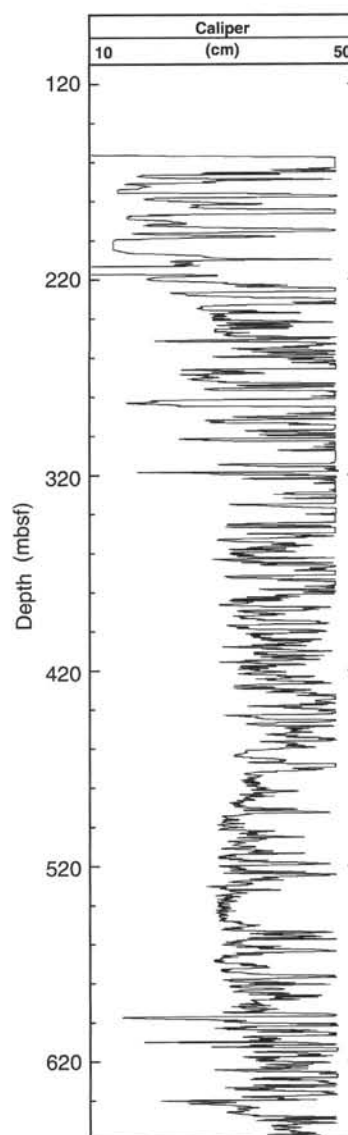


Figure 35. Caliper log recorded from the HLDT in Hole 997B.

ever, the GLT measurements also have been degraded by the enlarged borehole conditions. Data from the GLT have been used sparingly in our initial interpretation because of data quality concerns and the need for standard shore-based processing.

The Quad-combo tool string in Hole 997B was run at a cable speed of 275 m/hr, which yields high-resolution data, whereas the GLT was run at a cable speed of 183 m/hr. The LDEO-SST was recorded at a cable speed of 335 m/hr, and the Formation MicroScanner was run at a cable speed of 550 m/hr. A summary of the logging tool strings used during Leg 164 and discussion of their measurement principles is provided in the “Downhole Logging” section of the “Explanatory Notes” chapter (this volume).

Shipboard data editing was limited to depth shifting and the removal of some out-of-range data. Establishing consistent depths for each of the logs was accomplished by correlating the natural gamma-ray logs. The absolute depths, relative to seafloor, for all logs were fixed by identifying the gamma-ray signal associated with the seafloor and depth shifting the log data appropriately. The natural gamma-ray log pick for the seafloor in Hole 997B is 2775.0 mbrf, which is 6.6 m less than the water depth of 2781.6 mbrf (zero core depth)

determined by the drillers. Because the logs were measured from the dual elevator stool (DES), which is located 11.5-m above sea level, the actual log determined water depth at Hole 997B was 2763.5 mbsl. Out-of-range log measurements were removed from our working log database. These deletions were limited to data from within the drill pipe or near the bottom of the hole.

Logging Units

The description of the logged interval in Hole 997B is divided into three logging Units on the basis of obvious changes in the natural gamma-ray (NGT), bulk density (HLDT), sonic velocity (LSS/SDT), and electrical resistivity (DITE-SFL) measurements (Fig. 36). In Figure 36, both the far (DTLF) and near (DTLN) measuring acoustic velocity log are shown.

Log Unit 1 (113.0 mbsf [base of pipe] to 186.4 mbsf)

This interval between the base of the pipe (113.0 mbsf) and 186.4 mbsf is characterized by relatively low gamma-ray, density, velocity (DTLF), and resistivity log values. All of the recorded logs in Unit 1, however, are affected by the rugosity of the borehole. The gamma-

ray log shows an abrupt increase in value at the boundary between Unit 1 and Unit 2. The caliper log (Fig. 35) shows that the hole diameters are greatly reduced across the boundary from Unit 1 to Unit 2, which would contribute to the apparent change in recorded gamma-ray values. The resistivity log shows an upward step in value at the boundary between Units 1 and 2 (Fig. 36). The bulk density and acoustic velocity (DTLF) ramps up more gradually across the boundary between Units 1 and 2.

Log Unit 2 (186.4–450.9 mbsf)

Unit 2 is characterized by increasing velocities (DTLF) (1.5 km/s at the top of the unit to over 2.0 km/s at the bottom) with depth. The electrical resistivity log reveals a small increase of about 0.2 Ωm from the top to the bottom of Unit 2. The resistivity log also reveals three conspicuous high electrical resistivity intervals near 210, 365, and 440 mbsf. Both the acoustic velocity (DTLF) and resistivity logs are characterized by a distinct baseline shift to relatively higher values throughout Unit 2. At the base of Unit 2, across the boundary into Unit 3, the resistivity logs step down to lower values. In addition, the acoustic log (DTLF) shows a dramatic drop in velocity at the boundary between Units 2 and 3. In Figure 36, the acoustic log (DTLF) has

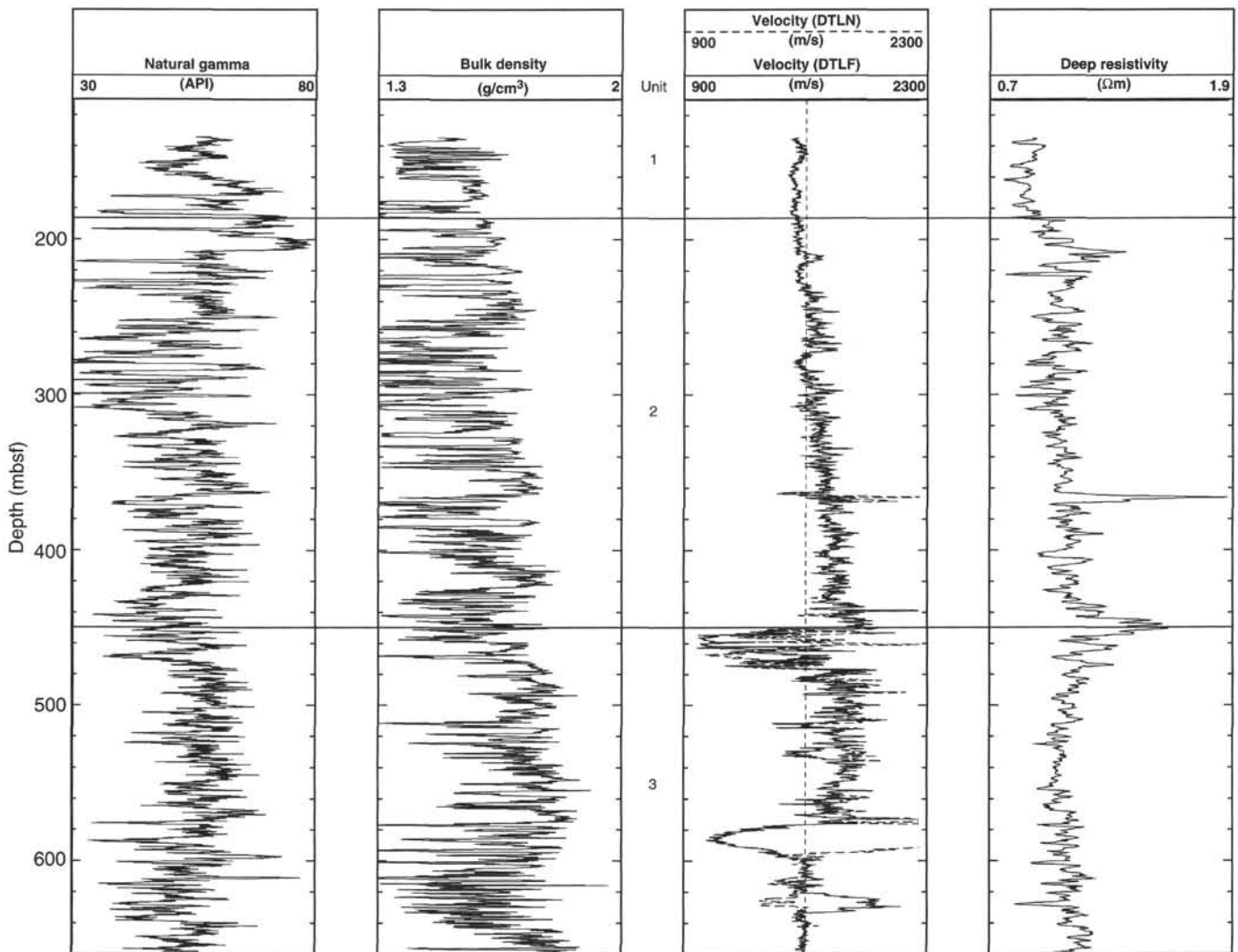


Figure 36. Log data from Hole 997B. Data shown include natural gamma-ray log data from the NGT, bulk density data from the HLDT, acoustic velocity data (DTLN [near] and DTLF [far] measurements) from the LSS, and deep-reading electrical resistivity data from the DITE. Also shown are the depths of logging Units 1, 2, and 3.

been used to select precisely a depth for the boundary between Units 1 and 2. This acoustic velocity (DTLF) boundary does not exactly match the apparent drop in resistivity observed near the base of Unit 2. This discrepancy of about 8 m will be a topic of further shore-based study. The natural gamma-ray and density logs are affected by significant changes in hole size throughout Unit 2. In general, however, the natural gamma-ray log is nearly constant throughout Unit 2, whereas the density log shows an increase in bulk density from $\sim 1.4 \text{ g/cm}^3$ at 186.4 mbsf to nearly 1.8 g/cm^3 at the base of Unit 2.

Log Unit 3 (450.9–715.0 mbsf [end of log run])

Unit 3 is characterized by consistently lower velocities (DTLF) and resistivities with respect to Unit 2. Numerous anomalous velocity intervals are seen in Unit 2 on the far-reading acoustic log (DTLF) (Fig. 36). Within the upper 26 m of Unit 3 (450.9–476.9 mbsf), the far reading acoustic log (DTLF) recorded very low velocities ($<1.1 \text{ km/s}$). A similar low (DTLF) velocity zone is observed within the depth interval between 573.0–597.0 mbsf. In general, the acoustic tool used in Hole 997B cannot measure velocities below the velocity of the fluids in the borehole, which are estimated to be $\sim 1.6 \text{ km/s}$. Therefore, the recorded velocities below 1.6 km/s indicate zones where the acoustic tool picked spurious transit times; however, these apparent “low velocities” coincide with low amplitude signals that indicate the presence of a highly attenuating material, probably free gas. A similar anomaly exists within the depth interval between 621.0 and 633.0 mbsf where the acoustic log (DTLF) indicates a conspicuous high velocity zone ($>2.0 \text{ km/s}$). Again, it is likely that the acoustic tool has incorrectly selected velocities from the recorded sonic waveforms. In fact, the near detectors (DTLN) on the acoustic log indicate that this anomalous zone is characterized by low velocities. The resistivity log in Hole 997B reveals higher values near the top of Unit 3 and decreasing values with depth. The higher resistivities, near the boundary between Units 2 and 3, may be due to the presence of free gas, which supports the acoustic log observations. The natural gamma-ray and density logs are nearly constant in Unit 3.

Gas Hydrate

Collett et al. (1984, 1988), Mathews (1986), and Prenskey (1995) have provided a comprehensive review of gas-hydrate well-log evaluation techniques. Confirmed natural gas hydrate occurrences are generally characterized by the release of unusually large concentrations of methane during drilling and an increase in log measured acoustic velocities and electrical resistivities. Gas hydrate-bearing stratigraphic sections exhibit relatively high electrical resistivities because some of the available pore space is filled with a solid nonconductor (i.e., gas hydrate) (Pearson et al., 1983). Because hydrates are electrical insulators, their presence in a stratigraphic section can be electrically detected and quantified. Gas hydrate-bearing horizons also exhibit anomalously high acoustic velocities because some volume of the pore space is occupied by solid gas hydrate that is characterized by acoustic velocities nearly twice that of water (reviewed by Prenskey, 1995). As discussed in the “Downhole Logging” section of the “Explanatory Notes” chapter (this volume), other well-log measurements, including bulk density, neutron porosity, and natural gamma ray, are not significantly affected by the presence of gas hydrate.

In comparison to logging Units 1 and 3 in Hole 997B, logging Unit 2 (186.4–450.9 mbsf) is characterized by a distinct stepwise increase in both electrical resistivity (increase of about $0.2 \text{ } \Omega\text{m}$) and acoustic velocity (increase of about 0.2 km/s) (Fig. 36). In addition, the deep-reading resistivity device (RILD) reveals three anomalously high resistivity units: near 210, 365, and 410 mbsf. For the purpose of this discussion, we have further subdivided logging Unit 2 into four additional Units: 2A, 2B, 2C, and 2D (Fig. 37). The three anomalously high resistivity units have been identified as logging Units

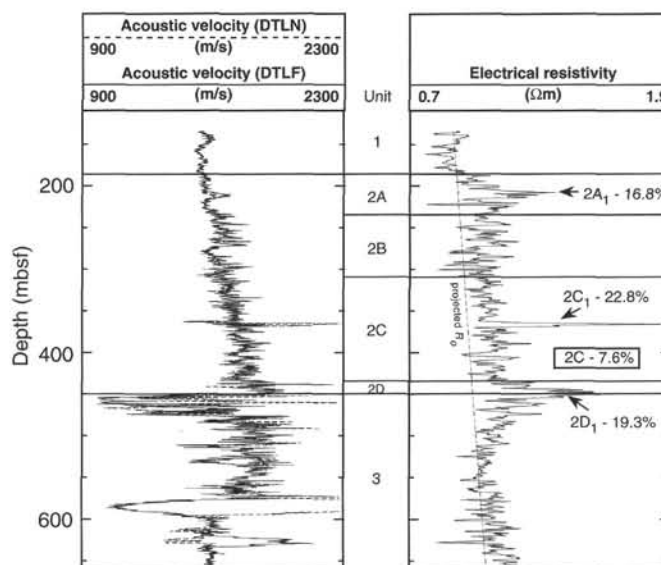


Figure 37. Log data used to calculate potential gas hydrate saturations in Hole 997B. Data shown include acoustic velocity data (both DTLN and DTLF measurements) from the LSS and deep-reading electrical resistivity data from the DITE. Also shown are the depths of logging Units 1, 2 (2A, 2A₁, 2B, 2C, 2C₁, 2D, and 2D₁), and 3. Listed beside the electrical resistivity log trace are the calculated gas hydrate saturations (percentage of pore space occupied by gas hydrate).

2A₁, 2C₁, and 2D₁ (Fig. 37). In comparison, the average resistivity log values are almost constant in logging Unit 2B, whereas the acoustic velocities increase with depth over the same interval. However, both the electrical resistivity and acoustic velocities increase with depth in Units 2C and 2D. Further comparisons show that the high electrical resistivity nature of Units 2A₁, 2C₁, and 2D₁ correlate to apparent velocity anomalies. Examination of the natural gamma-ray and bulk density logs (Fig. 36) reveals no apparent lithologic causes for the observed velocity and resistivity increases in Unit 2. The above observations are consistent with a material of increased resistivity and acoustic velocity, but similar density, that partially replaces some of the pore water in Unit 2. The depth of the boundary between Units 2 and 3 (450.9 mbsf) is in rough accord with the greatest depth at which methane hydrate probably occurs at Site 997 (see “Gas Hydrate” section, this chapter).

We assumed that the anomalously high resistivities and velocities measured in logging Unit 2 of Hole 997B are due to the presence of in situ gas hydrate, similar to our observations at Sites 994 and 995. Electrical resistivity log data can be used to quantify the amount of gas hydrate in a stratigraphic sequence (see “Downhole Logging” section, “Explanatory Notes” chapter, this volume). The DITE-SFL measurements of deep electrical resistivity (R_t) from Hole 997B (Fig. 37) were used to calculate water saturations (S_w) [gas hydrate saturation (S_h) is equal to $(1.0 - S_w)$] using the following modified Archie relationship: $R_t/R_o = S_w^{-n}$ (Schlumberger, 1989), where R_o is the resistivity of the sedimentary section if it contained only water ($S_w = 1.0$), R_t is the resistivity of the hydrocarbon-bearing intervals (log values), and n is an empirically derived parameter. This modified Archie relationship is based on the following logic: If the pore space of a sediment is 100% saturated with water, the deep-reading resistivity device will measure the resistivity of the 100% water-saturated sedimentary section (R_o). This measured R_o value is considered to be a relative baseline from which hydrocarbon saturations can be determined within nearby hydrocarbon-bearing intervals. To determine R_o for logging Unit 2 in Hole 997B, we have used the measured deep resistivities from Units 1 and 3 in Hole 995B, which are assumed not

to contain a significant amount of hydrocarbons ($S_w = 1.0$), to project a R_o trend line for Unit 2 in Hole 997B (Fig. 37). Laboratory experiments of different sediment types have yielded a pooled estimate for n of 1.9386 (reviewed by Pearson et al., 1983). Now knowing R_i , R_o , and n it is possible to use the modified Archie relationship to estimate gas hydrate saturation (S_h = fraction of the total pore space that is occupied by gas hydrate). Calculated S_h for Units 2A₁ and 2C₁ are about 16.8% and 22.8%, respectively (Fig. 37). The resistivity-derived S_h for Unit 2C averages 7.6%, which probably accounts for the baseline resistivity log shift observed throughout all of Unit 2. Logging Unit 2D is characterized by slightly higher resistivity log values, which suggest a relative increase in gas hydrate content. Resistivity log calculations do indicate higher S_h in Unit 2D₁ with an average value of 19.3%.

IN SITU TEMPERATURE MEASUREMENTS

The principal objective of the in situ temperature program at Site 997 was to determine the probable depth of the base of the gas hydrate stability zone and the thermal state within the stability field at a location with a strong BSR. Secondary goals included estimating heat flow for comparison with the results of traditional heat-flow surveys and constraining the amount of heat available for low-temperature diagenesis and microbial incubation.

Sampling Strategy

The Adara tool was used to measure in situ temperatures at a vertical resolution of 20–30 m in the upper 166.9 mbsf in Hole 997A. WSTP thermal measurements were attempted from 50.4 to 385.3 mbsf, with deployments spaced at 10–30 m at APC depths and 30–40 m at XCB depths. In situ temperature data also were obtained at depths of 173.5 and 414.1 mbsf with the prototype DVTP tool (see “In Situ Temperature Measurements” section, “Explanatory Notes” chapter, this volume). Table 19 summarizes the results of 20 Adara, WSTP, and DVTP measurements attempted at Site 997. Seventeen of the in situ measurements were successful.

APC Adara Measurements

The reference bottom-water temperature (BWT) of $2.7 \pm 0.5^\circ\text{C}$ for Hole 997A was measured using the Adara tool during a 10-min mudline stop before Core 164-997A-2H. The BWT at Site 997 is slightly lower than other BWT values measured on the Blake Ridge during Leg 164, but this observation is not surprising based on previously compiled evidence for significant spatial and temporal variations near the seafloor in this area (Ruppel et al., 1995). For the six downhole Adara deployments (Cores 164-997A-4H through 20H), mudline temperatures were measured for 5 min on both descent and ascent, and the probe remained in the bottom of the hole for 10 min.

The portions of the Adara records showing the mudline stops, penetration, and pullout are shown in Figure 38. The penetration record is, in all cases, associated with a frictional heating pulse ranging from 1.5° to 10°C above the equilibrium temperature values. All the Adara thermal equilibration records are of high quality and have smooth decay curves, except those obtained during recovery of Cores 164-997A-4H and 6H.

WSTP Measurements

The WSTP tool was used to measure in situ temperatures at both APC and XCB depths in Hole 997A. Although the WSTP generally yields equilibrium temperatures having greater uncertainties than the Adara data, the deployment of the WSTP at APC depths (shallower than 170 mbsf) made it possible to test the reproducibility of the temperature results obtained by the Adara tool.

The WSTP was always deployed in combined water sampling and temperature mode at Site 997. Mudline temperatures were measured for 5 min on both descent and ascent, and the probe remained in the bottom of the hole for 10 min before sampling of pore fluids commenced.

Figure 39 shows the mudline, penetration, and pullout records for WSTP deployments that did not crack the formation or result in thermistor failure. Although no frictional heating pulses were recorded, the pullout forces for all of the runs shown in Figure 39 were sufficiently high to infer that the probe was firmly implanted in the bottom of the hole during the equilibration interval.

Table 19. In situ temperature measurements in Hole 997A.

Core	Depth (mbsf)	Tool	Equil. T ^a (°C)	K ^b (W/(m-K))	Comments
2H	0	Adara	2.7 ± 0.5		Mudline temperature reading
4H	31.4	Adara	3.8 ± 0.5	1.03	Unsteady in-bottom record
6H	50.4	Adara	5.4 ± 0.25	0.97	
7H	50.4	WSTP			Thermistor flooded (#208)
10H	80.4	Adara	6.2 ± 0.10	1.04	
11H	80.4	WSTP	6.2 ± 0.25	1.04	New thermistor (#204)
13H	108.9	Adara	7.4 ± 0.10	1.06	
14H	108.9	WSTP	7.3 ± 0.25	1.06	
16H	137.4	Adara	8.7 ± 0.1	0.99	
17H	137.4	WSTP	9.7 ± 0.75	0.99	Poor in-bottom record; wiring pinched in instrument
19H	147.9	WSTP	8.8 ± 0.25	1.02	New thermistor (#201)
20H	166.9	Adara	9.6 ± 0.1	1.00	
22X	173.5	DVTP	9.9 ± 0.25	1.00	Switch to XCB coring; T2 reading low in bottom
26X	203.4	WSTP	10.9 ± 0.1	0.94	
31X	240.9	WSTP			In borehole water
36X	279.3	WSTP	13.6 ± 0.1	0.94	
41X	318.7	WSTP			In borehole water
44X	356.3	WSTP	16.3 ± 0.25	0.94	
48X	385.3	WSTP	17.4 ± 0.25	0.94	Shear pin broke; multiple penetrations
53X	414.1	DVTP	18.9 ± 0.5	0.94	T2 in borehole water?

Notes: Adara = Adara APC temperature shoe; WSTP = water-sampling temperature probe; and DVTP = Davis/Villinger Temperature Probe.

^a The equilibrium temperature was determined by trial-and-error minimization of the misfit between the synthetic equilibration curve and the recorded data in temperature vs. $F(\alpha, t)$ space. The assignment of errors is discussed in the text.

^b K indicates the average, uncorrected thermal conductivity value used to convert from depth to resistance. A thermal conductivity value of 0.94 W/(m-K) was adopted for all in situ temperatures measured deeper than 200 mbsf.

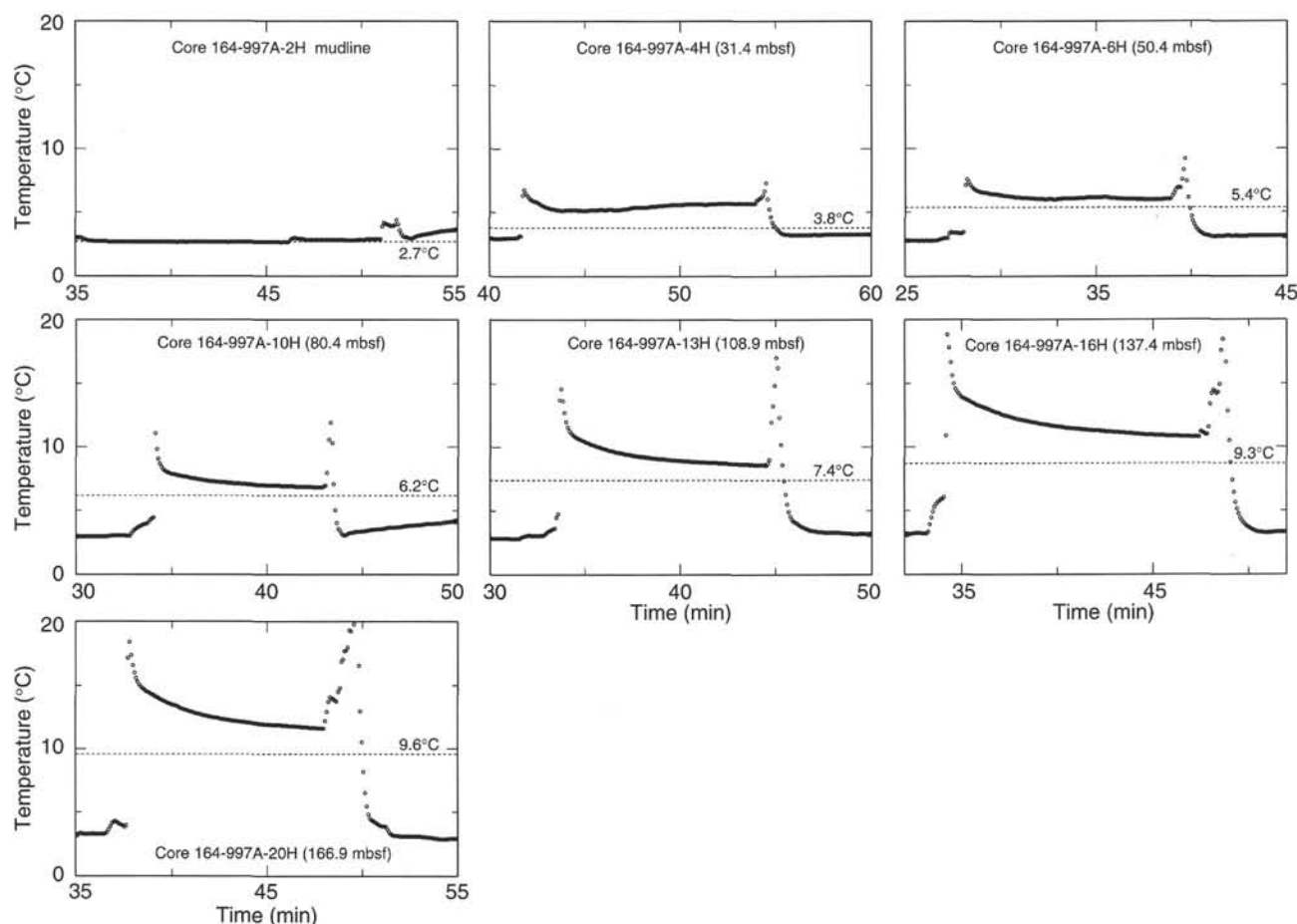


Figure 38. Raw temperature vs. time records from the Adara tool for the period between the descending and ascending mudline stops. Dashed lines = equilibrium temperature determined by fitting synthetic curves to the equilibration record, assuming thermal conductivity of 1 W/(m·K). The mudline temperature reading was taken before Core 164-997-2H.

DVTP Measurements

The prototype Davis/Villinger Temperature Probe was deployed just below the switch from APC to XCB operations (165.2 mbsf) and again at 414.1 mbsf, the greatest depth at which in situ temperature measurements were obtained during Leg 164. The DVTP runs included 5-min mudline stops on both ascent and descent and a 10-min equilibration interval in the bottom of the hole.

Figure 40 shows the temperatures recorded by the T1 (probe tip) thermistor at the mudline and in the bottom of the hole during the two deployments of the DVTP tool. Temperatures recorded by the T2 thermistor (12 cm above the probe's tip) are not shown because the T2 thermistor read slightly lower than T1 at the mudline and significantly lower (0.5°C for Core 164-997A-22X and 6°C lower for Core 164-997A-53X) than T1 in the bottom of the hole. It is possible that only the tip of the probe penetrated during the second deployment and that T2 remained in the borehole water.

Both deployments of the DVTP produced stable in-bottom records. The small temperature perturbation just after penetration at 414.1 mbsf (Core 164-997A-53X) may indicate that the tool sank slightly deeper under its own weight immediately following emplacement. Frictional heating recorded by T1 on pullout implies that

at least the probe tip was emplaced firmly in the bottom of the hole during both deployments.

Corrections

Compared to the in situ temperature data collected at Site 995, the DVTP, WSTP, and Adara measurements in Hole 997A are generally internally consistent, with mudline temperatures within 0.75°C of the BWT recorded by the Adara tool before Core 164-997A-2H. Thus, no corrections were applied to any of the temperature data for this preliminary analysis.

Equilibrium Temperatures

The Adara and WSTP data were processed using standard ODP software that fits synthetic temperature-time curves to the raw records and determines the equilibrium temperature value. The quality of the equilibrium temperature determination critically depends on the choice of the penetration record and the initial and final points in the equilibration record. The shape of the synthetic curves is relatively insensitive to the choice of a thermal conductivity value within the normal range for deep-ocean sediments (0.8–1.2 W/(m·K)). To

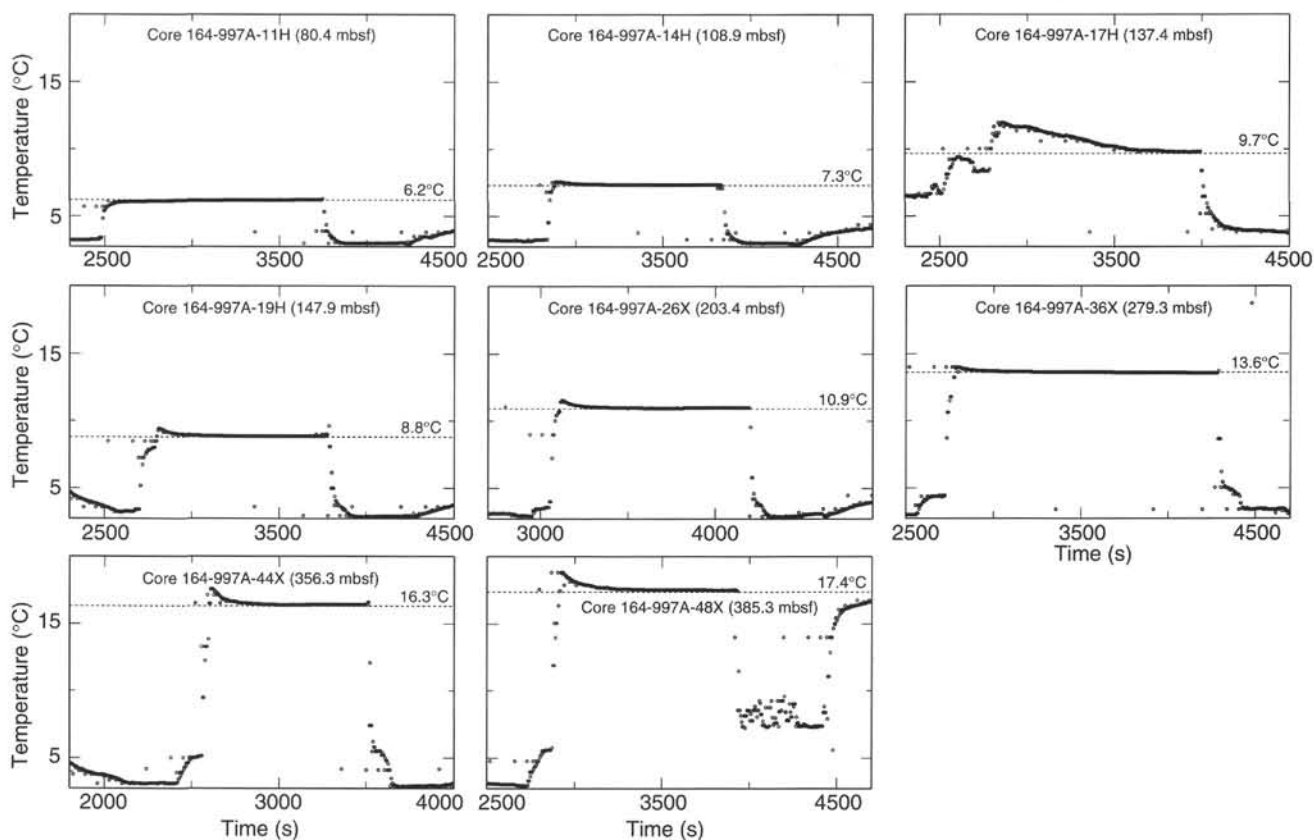


Figure 39. Temperature vs. time records from the WSTP for the period between the ascending and descending mudline stops. Dashed lines = equilibrium temperatures determined by fitting synthetic curves to the equilibration record, assuming thermal conductivity of 1 W/(m·K).

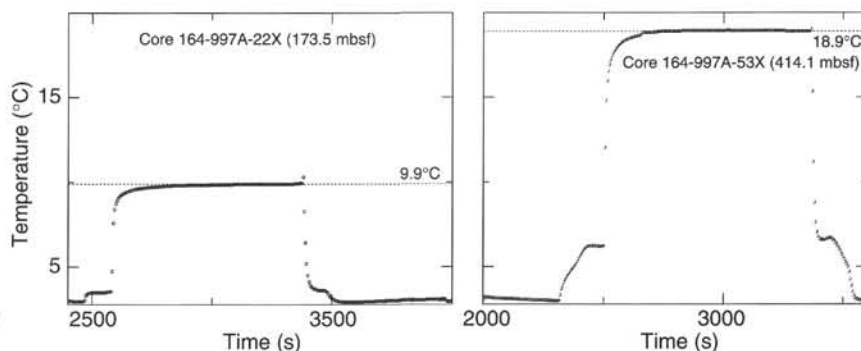


Figure 40. Corrected temperature vs. time data from the DVTP. Dashed lines = the estimated equilibrium temperatures.

make the analyses internally consistent, a thermal conductivity value of 1.0 W/(m·K) was assumed for all of the equilibrium temperature determinations at Site 997.

Equilibrium temperatures for the DVTP deployments were estimated by determining the temperature to which the equilibration records appeared to be asymptotic.

Figure 41A shows equilibrium temperatures as a function of depth in Hole 997A. Errors are estimated subjectively based on (1) the stability of the equilibration record, (2) the misfit between the equilibration curve and the best-fitting synthetic curve, (3) the degree of mismatch between the reference Adara mudline temperature and that recorded before a given in situ measurement, and (4) deployment-related factors such as fouling of thermistors by seawater.

The average geothermal gradient in Hole 997A is 36.8 ± 0.4 mK/m if the data are weighted in proportion to the inverse of the squared er-

ror. The regression equation corresponding to the best-fit line is $T(z) = (3.39 \pm 0.09^\circ\text{C}) + (0.0368^\circ \pm 0.004^\circ\text{C/m})z$, where z is depth in meters and T is temperature in $^\circ\text{C}$. The best-fitting line through the in situ measurements intercepts the seafloor at $3.39 \pm 0.09^\circ\text{C}$, indicating that the bottom water ($T = 2.68^\circ \pm 0.75^\circ\text{C}$) is not in thermal equilibrium with the underlying sediments.

Heat Flow

The in situ equilibrium temperature data were combined with laboratory thermal conductivity data collected from APC cores to estimate heat flow as a function of depth in Hole 997A. The laboratory thermal conductivity data (Fig. 31) were corrected to seafloor temperature and pressure (hydrostatic) conditions (Ratcliffe, 1960) and averaged over the depth intervals between the in situ temperature

measurements. Using the standard formulation of Bullard (1939), the temperature vs. depth data were recast in temperature vs. resistance space. The slope of the temperature vs. resistance curve yields a direct measure of heat flow, which averages 35.9 ± 0.4 mW/m² between the seafloor and 414.1 mbsf (Fig. 41B). A traditional heat-flow survey at the same location yielded a value of 46.0 ± 2.3 mW/m² (Ruppel et al., 1995), 20% higher than heat flow determined from the in situ temperature data.

Discussion

Site 997 is characterized by a geothermal gradient within 1 standard deviation of the estimated gradient at Site 994 (36.4 ± 1.3 mK/m) but 9% higher than the gradient at Site 995 (33.5 ± 0.9 mK/m). The cooler temperatures measured at Site 995 relative to Sites 994 and 997 are outside the estimated range of errors. The estimated temperatures at the BSR are 18.7°C (440 mbsf) at Site 995 and 20.0°C (450 mbsf) at Site 997. The temperature at a comparable depth (440 mbsf) at Site 994, where there is no BSR, is estimated at 20.1°C . Sediments overlying a BSR (at Sites 995 and 997) are not uniformly cooler than those at a comparable depth in an area with no BSR (Site 994), as would be expected if gas trapped below the BSR acted as an insulator and refracted heat to the region lacking a BSR. Thus, the lower thermal gradient observed at Site 995 may be more closely related to hydrologic processes than to any phenomenon associated with the presence of the BSR.

SYNTHESIS AND SIGNIFICANCE

Site 997 is located on the crest of the Blake Ridge 6.7 km northeast of Site 995 and 9.8 km northeast of Site 994. The results of Site 997, coupled with those obtained at Sites 994 and 995, enabled us to establish the lateral extent, vertical occurrence, amount, habitat, and composition of marine gas hydrate deposits and to assess the relation among the distribution of gas hydrate, the depth of the BSR, and the base of gas hydrate stability zone predicted from theoretical and experimental considerations.

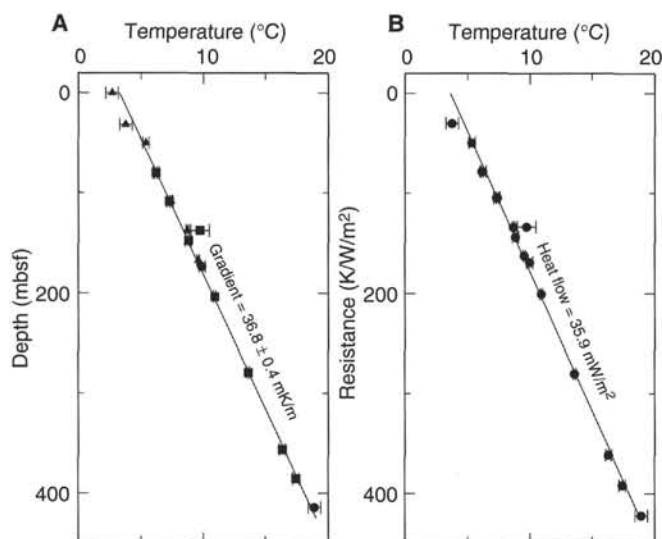


Figure 41. **A.** Equilibrium temperatures as a function of depth. Triangles = Adara data, squares = WSTP data, and circles = the results of DVTP measurements. **B.** Equilibrium temperature as a function of resistance. The slope of the curve is a direct measure of heat flow, and the data were weighted by the inverse of the squared errors to determine the average heat-flow value. The seafloor intercept for the line that best fits the data is $3.39^\circ \pm 0.09^\circ\text{C}$.

Sedimentation and Diagenesis

Lithology and Sedimentation Rates

The sedimentary section recovered at Site 997 is similar in lithologies and ages to those at Sites 994 and 995. The Pleistocene to uppermost Pliocene section (lithostratigraphic Units I and II; 0–108 mbsf) is characterized by greenish gray nannofossil-rich clay (~ 30 wt% CaCO_3) interbedded with light greenish gray nannofossil clay (~ 50 wt% CaCO_3). The Pliocene–Miocene section (lithostratigraphic Unit III; 108–750 mbsf) is composed of homogeneous dark greenish gray nannofossil-bearing clay and claystone. Total carbonate content is generally less than 25 wt% as CaCO_3 . No changes in lithology (see “Lithostratigraphy” section, this chapter) or physical properties (see “Physical Properties” section, this chapter) were identified in Unit III throughout the interval where the distinct BSR occurs (i.e., 464 ± 8 mbsf; see “Geophysics” section, this chapter).

The sedimentation rate curve for the Site 997 sediments (Fig. 13) is similar to that of Site 994 (Fig. 13, “Site 994” chapter, this volume). Pleistocene sediments are estimated to have accumulated at ~ 40 m/m.y.; however, the Pliocene sediments are characterized by higher sedimentation rates (~ 70 – 200 m/m.y.). A small hiatus occurs at ~ 380 mbsf. These high rates and the hiatus are thought to have been caused by contour-current reworking and redeposition. The upper Miocene terrigenous-rich section was deposited at a much higher rate (~ 260 m/m.y.) that is comparable with the rates measured for the Miocene sections at Sites 994 and 995.

Sediment Accumulation Rates

Mass accumulation rates (MARs) increase downhole at Site 997 (Fig. 42) primarily because of an increase in the noncarbonate fractions. Typical rates for the noncarbonate fractions are less than 5 g/cm² per 10^3 yr for Quaternary-age sediments. They increased to ~ 20 – 25 g/cm² per 10^3 yr in the Pliocene and to >30 g/cm² per 10^3 yr during the late Miocene. In general, the MARs at Site 997 are similar to the MARs at Sites 994 and 995 (Fig. 42); however, the rates are slightly greater in the upper Pliocene and less in the lower Pliocene and Miocene sections. The changes in the carbonate

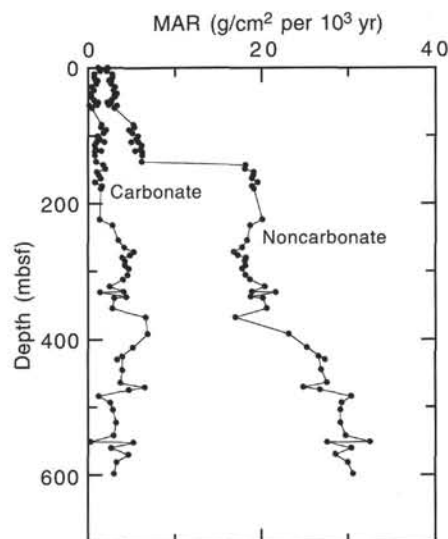


Figure 42. Mass accumulation rates for both carbonate and noncarbonate fractions calculated from the sedimentation rates, shipboard density, and porosity measurements for Site 997. Carbonate contents were determined from an XRD peak of calcite so that diagenetic dolomite and siderite were excluded from the carbonate fraction. The noncarbonate fraction appears to be composed mainly of terrigenous materials with subordinate diatoms.

MARs are more modest, suggesting that an increased supply rate of clastic material existed in pre-Quaternary times.

Organic carbon percentages are typically less than 1% for the Quaternary sediments and increase to ~1.4% for upper Miocene sediments (Fig. 43). The MAR of organic carbon increases downhole by about a factor of 10, tracking the MAR of the noncarbonate material.

Diagenetic Dolomite and Siderite

Both diagenetic dolomite and siderite occur at Site 997. Their occurrences and variations provide insight into the depositional and diagenetic environments of the Site 997 sediments. Concentrated dolomite beds and nodules, ranging in size from 1 to 6 cm, are restricted to the Pleistocene sediments. The first appearance of dolomite was at 40.85 mbsf, which is below the base of sulfate reduction zone (~21 mbsf) (see "Inorganic Geochemistry" section, this chapter) and in the zone where methane concentrations are increasing rapidly (see "Organic Geochemistry" section, this chapter). Although a high alkalinity peak was not observed at this level, abundant occurrences of pyrite nodules (~1 cm in diameter) strongly suggest that bacterial sulfate reduction and anaerobic methane oxidation had occurred in these sediments. Local increases in alkalinity and a dramatic decrease in Mg^{+2} and Ca^{+2} are focused at the base of the sulfate reduction zone (Borowski et al., 1995). We suspect that the dolomite may have been formed when the base of the sulfate reduction zone passed through this sediment horizon. Reduced rates of sedimentation in the Quaternary would have focused the diagenetic effect of anaerobic methane oxidation on these sediments. This pattern also is observed at Sites 102 (Lancelot et al., 1972), 533 (Matsumoto, 1983), 994, and 995 on the flank of the Blake Ridge, and it could be typical throughout the Blake Ridge area.

Dolomite occurs sporadically as disseminated crystals in Pliocene sediments. The overall decrease in the abundance of dolomite and the frequency of concentrated dolomite beds may suggest that dolomite was never formed in the pre-upper Pliocene section.

Siderite first appears at 100 m and exhibits a downhole increasing trend. Concentrated siderite beds and nodules were first found at 540 mbsf and are intermittent through the rest of the section. Concentrated laminae and nodules of siderite occur well below detected gas hydrate and roughly coincide with the sediments containing very high gas concentrations. The origin of siderite is not evident, but the association with high gas concentrations is intriguing (Matsumoto, 1989).

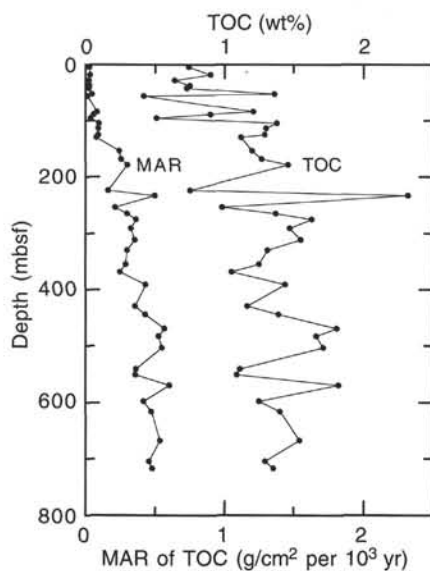


Figure 43. Total organic carbon content and mass accumulation rates for Site 997.

Shore-based mineralogical and isotopic study will provide data to assess their genetic relations.

Detection and Indications of the Presence of Gas Hydrate

Direct Sampling

Site 997 was intentionally drilled where a strong BSR occurs (see Fig. 1). One interval of massive gas hydrate was recovered from Site 997 (see "Gas Hydrate" section, this chapter). Volumetric calculations based on the controlled decomposition experiments on gas hydrate nodules from Core 164-997A-42X-3 (330.03 mbsf) indicated that this sample was composed of structure I (Sloan, 1990) methane hydrate with its cages largely occupied by CH_4 .

Proxy Measurements

The presence of gas hydrate within the Site 997 sediments is inferred on the basis of the following observations:

1. The cores from Site 997 were observed to evolve large amounts of gas in a similar fashion to what was observed at Sites 994 and 995 (see "Synthesis and Significance" sections, "Site 994" and "Site 995" chapters, this volume). Gas evolution from decomposing gas hydrate may have caused the low core recovery (Fig. 44).

2. PCS data (see "Downhole Tools and Sampling" section, this chapter) indicate that the sediments below 202.4 mbsf contain methane concentrations that are at or exceeding methane saturation in seawater. There is no acoustic indication that gas bubbles exist above 450 mbsf, and the only known additional source for methane (beyond what can be dissolved in seawater) is the decomposition of gas hydrate. Therefore, gas hydrate must have occurred in PCS Cores 164-997A-25P (202.4 mbsf) and 49P (394.90 mbsf). Moreover, the data from the PCS Core 164-997B-10P (462.20 mbsf) indicates that the concentration of methane in the interstitial waters is ~10 times the saturation values (see "Downhole Tools and Sampling" section, this chapter). The interstitial-water chemistry of Core 164-997B-10P

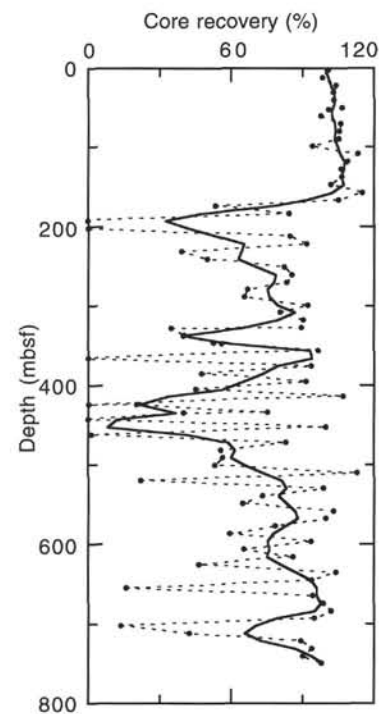


Figure 44. Plot showing the percentage recovery in individual cores (circles and dashed line) from Holes 997A and 997B smoothed with a five-point average (solid line).

(462.20 mbsf) shows a normal chloride concentration, indicating that gas hydrate decomposition did not occur within this sample. Thus, gaseous methane occurs in situ at this depth (which corresponds to the BSR; see “Geophysics” section, this chapter).

3. Acoustic data also indicate that free gas is present below ~450 mbsf. The ZO-VSP data from Site 997 indicate a trend of generally increasing velocity from 150 to 464 mbsf to average velocities >1800 m/s. Lower velocities at 322 mbsf and higher velocities at 365 mbsf are superimposed on this trend. Below 464 mbsf, velocities drop to a low of 1400 m/s at 480 mbsf (Fig. 34). VSP velocities never exceed 1650 m/s below 450 mbsf and are below 1500 m/s for more than half the interval between 450 and 700 mbsf. Sonic log velocities also increased downhole from about 1550 m/s at the base of the drill pipe (~113 mbsf) to a local maximum of ~2000 m/s at 450 mbsf. Between 450.9 and 476.9 mbsf, sonic velocities decrease to <1200 m/s. Such low velocity values clearly indicate the presence of free gas.

4. Both the general freshening trend of the interstitial waters and the intersample variation in the interstitial-water chloride concentrations between 205 and 452 mbsf suggest that gas hydrate is present in this interval (see “Inorganic Geochemistry” section, this chapter). Interstitial-water compositions are naturally modified by diffusion so that in a relatively static sedimentary sequence only small changes in chloride concentrations occur between adjacent samples. Thus, the relative amplitude of the chloride anomalies are proportional to the amount of gas hydrate that dissociated within the sample during core recovery.

5. Core temperatures upon recovery on the catwalk were noted to be quite variable. Because gas hydrate decomposition is endothermic, low-temperature anomalies are interpreted as indicating areas where hydrate decomposition occurred recently or where significant amounts of gas expansion occurred. Temperatures <5°C were observed only in the interval between 200 and 511.54 mbsf (see “Gas Hydrate” section, this chapter).

6. Data from downhole logs also are interpreted as indicating the presence of gas hydrate in the interval between 186.4 and 450.9 mbsf. Both the *P*-wave velocity and electrical resistivity logs are distinctly offset in this zone; however, there are no obvious changes in either the lithologic description or the physical properties data from this interval that explain these offsets. Thus, the discrepancy between the in situ observations made with the logs and the analyses of the recovered material is potentially related to some property that is different in situ than in the recovered cores (e.g., the presence of gas hydrate).

Defining the Zone of Gas Hydrate Occurrence

The depths to the top and the base of the zone of gas hydrate occurrence at Sites 994, 995, and 997 were measured using interstitial-water chloride anomalies and downhole-log data. The base of the zone of gas hydrate occurrence was also measured with ZO-VSP data. (Table 20; Fig. 45). Interstitial-water chloride anomalies established whether gas hydrate occurred within a given sample. The occurrence of the highest and lowest chloride anomalies establish the minimum range in the gas hydrate distribution zone. Because the data on the temperatures of the recovered cores and the spiky pattern of the interstitial-water chloride concentrations indicate that the distribution of gas hydrate is rather patchy, the lack of an interstitial-water chloride anomaly in individual samples does not confidently determine the limit of the zone. Thus, the top of a gas-hydrate-bearing zone might be higher and its base lower because of the distribution of samples. In Table 20 and Figure 45, we show the boundaries of the gas hydrate-containing zone extending from the last distinct chloride anomaly to the next sample that lies along the chloride baseline (see “Gas Hydrate Estimates” below). Thus, at Site 997 the base of the gas hydrate, as identified by the interstitial-water chloride values, occurs between 451 and 467 mbsf. Shipboard analyses of the direct-arrival ZO-VSP data indicated that the base of the gas hydrate is at 464 ± 8

mbsf (see “Geophysics” section, this chapter), assuming that the BSR coincides with the base of the gas hydrate. The bottom of the gas hydrate-bearing zone is picked as being at 450.9 mbsf in the downhole-logging data. Thus, a slight (>5 m) difference exists between the downhole log picks and the VSP estimate for the bottom of the gas hydrate-bearing zone at Site 997.

Comparisons among Sites 994, 995, and 997 suggest that the base of the gas hydrate-bearing zone lies at increasing sub-bottom depths along this drilling transect (Table 20; Fig. 45). Moreover, the ZO-VSP data indicate that the position of the BSR is at a slightly greater sub-bottom depth at Site 997 than Site 995. However, the water depths decrease along this transect (2797.6 mbsl at Site 994; 2778.5 mbsl at Site 995; and 2770.1 mbsl at Site 997). This observation contrasts with the usual expectation that the BGHS should get shallower as the water depths decrease because of the associated decrease in hydrostatic pressure.

At present, this observation is not understood; however, it may indicate variations in the pressure, temperature, gas and fluid compositions, and the microenvironment within the sediments, which alter the gas hydrate phase stability. The variation in the geothermal gradients measured at these sites (see “In Situ Temperature Measurements” section, this chapter) is inconsistent with this pattern. Nor have we identified variations in the gas and fluid chemistries, sediment lithology, or physical properties that explain this observation. However, this pattern might indicate that pore pressures under the crest of the Blake Ridge are a few percent above hydrostatic pressure.

Discrepancy Between Observed and Predicted Base of Gas Hydrate Stability

Direct sampling, chlorinity anomalies, and downhole-logging data all suggest that gas hydrate occurred at least intermittently within a zone between 186 and 452 mbsf (Table 20). The inferred gas hydrate-bearing zone does not extend to the predicted base of gas hydrate stability (491 to 524 mbsf; Fig. 46) as estimated with the experimental data and measured geothermal gradient at Site 997 (see “In Situ Temperature Measurements” section, this chapter). Why the discrepancy exists is unclear, and several possible explanations need to be considered:

1. The base of the inferred gas hydrate occurrence zone is a fossil from previous higher temperature and/or lower pressure conditions.
2. Experimental data do not adequately characterize the behavior of natural gas hydrate, especially in fine-grained sediments.
3. Gas hydrate actually existed below 460 mbsf, but we did not detect it.

Estimation of the Amounts of Gas Hydrate

The amounts of gas hydrate contained in sediments were estimated from the interstitial-water chloride anomalies and from the observed changes in the downhole-logging data.

1. Estimates of the amount of gas hydrate that existed in the seafloor before the sediments were recovered from Site 997 were made by assuming that diffusive equilibration prohibits significant and nonsystematic interstitial-water chloride concentrations from occurring between closely spaced samples. Thus, chloride spikes are only a result of gas hydrate decomposition during sample recovery. To produce an estimate of the interstitial-water salinity through the zone extending from 204.75 to 451.65 mbsf (Fig. 47A), where erratic chloride values were measured, a polynomial was fit to the relatively smooth chloride data above 195 and below 455 mbsf. The use of just the chloride data above 195 and below 455 mbsf in predicting the in situ chlorinity values for the interval between 195 and 455 mbsf results in a conservative estimate of gas hydrate amounts. All but one

Table 20. Top and base of gas hydrate distribution.

	Chloride anomaly depth (mbsf)	Zero-offset VSP depth (mbsf)	Logging depth (mbsf)	Experimental depth (mbsf)
Site 994 (depth of water = 2799.1 mbsl):				
Top	194.95–209.2		212.0	
Base	427.37–439.5		428.8	497 (SW)–529 (PW)
Site 995 (depth of water = 2778.5 mbsl):				
Top	190.25–195.35		193.0	
Base	438.0–465.12	440 ± 10 (DM)–450.0 (AM)	450.0	541 (SW)–577 (PW)
Site 997 (depth of water = 2770.1 mbsl):				
Top	179.57–204.75		186.4	
Base	451.65–467.45	464 ± 8 (DM)	450.9	495 (SW)–527 (PW)

Note: DM = direct measurements of first arrival, AM = acoustic modeling, SW = based on experiments in seawater, and PW = based on experiments in pure water.

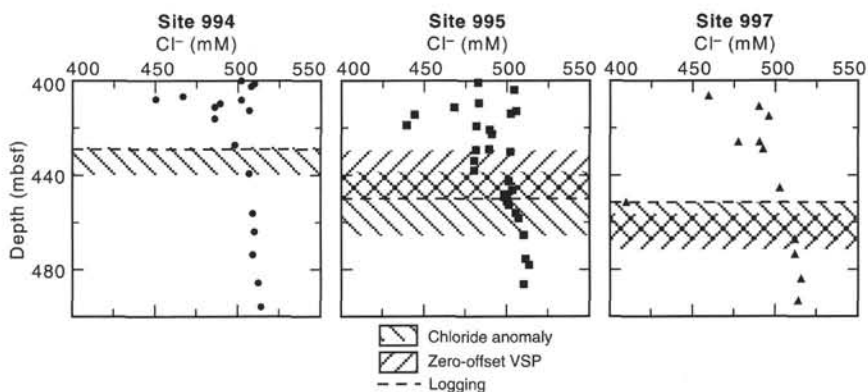


Figure 45. Plot of the depth to the base of gas hydrate occurrence at Sites 994, 995, and 997 as estimated by interstitial-water chloride anomalies, ZO-VSPs, and downhole logging.

of the measured chloride concentrations in this zone have lower values than the calculated in situ values, some significantly lower. The difference between the calculated in situ chloride concentrations and the measured chloride concentrations were used to establish the relative chlorinity anomaly that is associated with each sample (Fig. 47B).

The calculated chloride anomalies enable the amount of gas hydrate that occurred in these samples to be estimated. Corrections for the porosity of the samples were made using the shipboard physical properties data (see “Physical Properties” section, this chapter) that exist throughout this interval. The estimated volume percentage of the samples that was occupied by gas hydrate had a skewed distribution, ranging to as much as 13.6 vol% (at 329.4 mbsf) and having a mean value of 2.4 ± 2.7 vol% and a median value of 1.5 vol% for all the interstitial-water samples that were collected between 205 and 455 mbsf (Fig. 47C). However, these are minimum estimates because the baseline used to calculate these values may be lower than the actual in situ interstitial-water chlorinities and because the gas expansion during core recovery may result in lower core recovery from the more gas hydrate-rich sample.

2. Calculations of the percentage of gas hydrate that is required to explain the observed change in the downhole electrical resistivity log (Fig. 59, “Downhole Logging” section, “Site 995” chapter, this volume) indicate that the general trend through this interval (between 186.4 and 450.9 mbsf) can be explained by the pervasive addition of as much as 7.6% gas hydrate in the pore spaces (or ~4 vol% of bulk sediments). The same calculation indicates that the most concentrated horizon (~220 mbsf) contains as much as 22.8% gas hydrate in the pore space (~11 vol%). Independent estimation of the amounts of gas hydrate from different data sets (chloride anomalies and downhole-logging data) has provided very similar estimates of the percentage of gas hydrate contained in the sediments between ~190 and 450 mbsf.

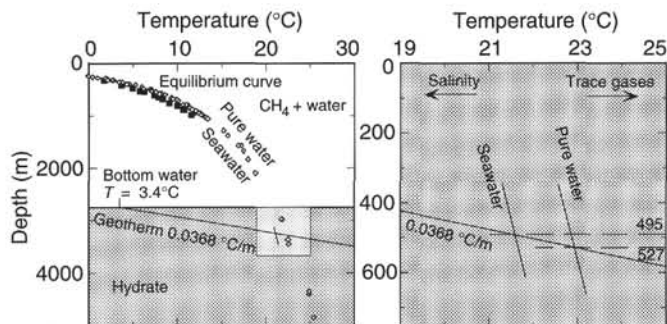


Figure 46. The zone of CH₄ hydrate stability in the marine environment lies between the sediment-water interface and the intersection of the geotherm and the CH₄-hydrate-water equilibrium curve (after Kvenvolden and McMenamin, 1980). At Site 997, the sediment-water interface is 2770 mbsl, and the geotherm is $3.4^\circ + 0.0368^\circ\text{C}/\text{mbsf}$. The depth of intersection for the CH₄-hydrate-water equilibrium curve in pure water (compiled in Sloan, 1990) occurs at ~527 mbsf; the depth of intersection for the CH₄-hydrate-water equilibrium curve in seawater (Dickens and Quinby-Hunt, 1994) occurs at ~495 mbsf. Depths along the equilibrium curves assume a hydrostatic pressure gradient of 0.010 MPa/m (1.467 psi/m). Note that dissolved ions shift the CH₄-hydrate-water equilibrium curve such that the zone of CH₄ hydrate stability is shallower than expected from consideration of the CH₄-pure water system, and that incorporation of trace gases (e.g., CO₂, H₂S, and C₂) into the hydrate lattice has the opposite effect.

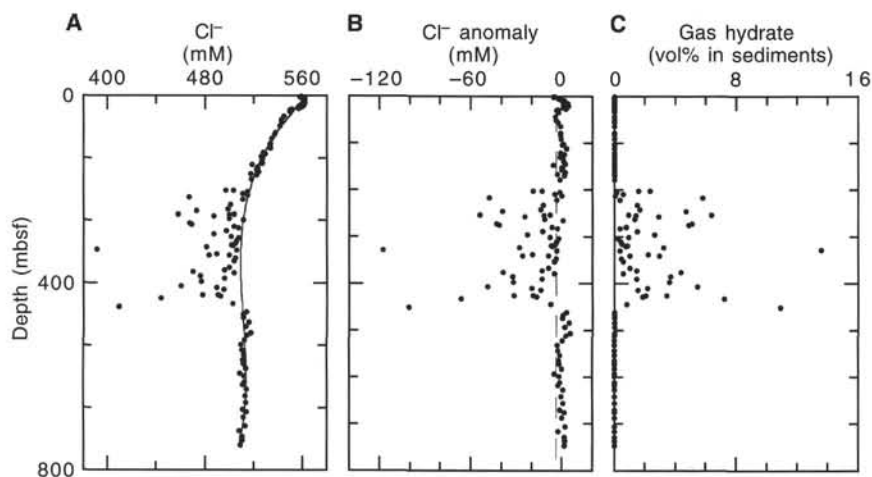


Figure 47. **A.** The interstitial-water chlorinity profile at Site 997 indicates a distinct freshening with depth that is highlighted by a zone of low and erratic values between 200 and 455 mbsf. A polynomial fit to the data above and below the 200–455 mbsf zone is indicated. **B.** Chlorinity anomalies are interpreted with respect to the polynomial. **C.** The percentage of gas hydrate by volume is calculated by assuming that the chloride anomalies (B) are solely produced by gas hydrate decomposition during core recovery and corrected by porosity using a linear fit to the porosity data in the physical properties section.

Origins of Fresher Interstitial Waters

Interstitial waters with a chloride concentration less than seawater were encountered through sediment sections below ~30 mbsf at Site 997 (in addition to Sites 994 and 995). Although the intersample variations in interstitial-water chloride concentration can be explained by gas hydrate decomposition during sampling, the origin of the fresher waters beneath the base of the current gas hydrate stability zone is unknown. The relationship between the current in situ chloride concentration, current gas hydrate amounts, and the history of gas hydrate formation and decomposition within these sediments needs to be established. In addition, other sources of freshwater need to be considered.

Habit of Natural Gas Hydrate Occurrences

Sites 994, 995, and 997 have stratigraphically similar patterns of gas hydrate distribution. However, slightly more gas hydrate may occur along the transect going from lower values at Site 994 to higher values at Site 997. Gas hydrate occurred throughout an ~250-m-thick section. The top of the gas hydrate-bearing zone (190–210 mbsf) was distinguished by one of the larger concentrations of gas hydrate, and some solid hydrate pieces were recovered. The distribution of shipboard core temperature measurements and interstitial-water chloride concentrations indicate that significant variations in the amount of gas hydrate occur on the centimeter to meter scale. However, we inferred that most of the hydrate in the recovered sediments was finely grained and dispersed within the available pore space.

The increase in the amount of gas hydrate inferred at Site 997 correlates with the increase in the amount of free gas in the sediments below the BSR. Site 997 is on the crest of the Blake Ridge (Fig. 1), where upward gas migration may be focused. In addition, an interval of dipping reflectors exists beneath the BSR on the southern flank of the Blake Ridge (Fig. 1) and extends upward to the BSR near Site 997. The results from Sites 994 and 995 suggest that this interval contains free gas. If upward migration occurs along this horizon, additional gas may be concentrated near Site 997.

The Nature of the BSR

We have attempted to clarify the nature and origin of BSR by comparing the results of core analysis, downhole logging, and VSP experiments among Sites 994, 995, and 997. Correlations between traveltimes measured in the ZO-VSP data indicate that the BSR occurs at 464 ± 8 mbsf at Site 997. No significant change in either lithology or physical properties measurements occurred at this depth. The lithologies and physical properties of the stratigraphic section

below 130 mbsf at Site 997 are indistinguishable from the section below ~130 mbsf at Sites 994 and 995 (see “Principal Results” sections, “Site 994” and “Site 995” chapters, this volume).

Both the sonic log and VSP data indicate that decreasing interval velocities occur near the depth of the BSR (~450 mbsf). Decreasing velocity without a change in sediment density will produce a negative polarity reflection. The BSR here is a negative polarity reflection that is presumably related to the decrease in acoustic velocity. The drop in velocity to below-seawater values is clearly related to the presence of free gas below 464 mbsf.

The base of the gas hydrate zone on the crest of the Blake Ridge (e.g., at Sites 995 and 997) likely serves as a seal that traps underlying free gas. Velocities on sonic logs and VSPs are anomalously low beneath the gas hydrate zone, and PCS cores indicate that gas is greatly oversaturated in the depth region. The total volume of gas may be as great in the underlying free-gas zone as within the overlying gas hydrate zone.

Conclusions

Interstitial-water chlorinity anomalies, anomalously cold temperatures in the recovered cores, and patterns in the downhole log data indicate that gas hydrate occupies between >1.5 vol% and 4 vol% or more of the sediment section from 195 to 450 mbsf at Site 997, with several intervals containing as much as 11 vol% gas hydrate. A significant portion of the gas hydrate is inferred to be finely dispersed within the homogenous sediments. All of the inferred gas hydrate occurs well above the predicted base of gas hydrate stability at this site. The BSR is apparently associated with a zone of free gas that is especially well developed for 30 m and extends for more than 100 m below the BSR.

REFERENCES

- Bangs, N.L.B., Sawyer, D.S., and Golovchenko, X., 1993. Free gas at the base of the gas hydrate zone in the vicinity of the Chile triple junction. *Geology*, 21:905–908.
- Borowski, W., Paull, C.K., and Ussler, W., III, 1995. Gas hydrates, methane inventory, and sulfate profiles: predicting methane flux and gas hydrate occurrence from sulfate profiles in piston cores. *Eos*, 76:S164.
- Bullard, E.C., 1939. Heat flow in South Africa. *Proc. R. Soc. London A*, 173:474–502.
- Cande, S.C., and Kent, D.V., 1995. Revised calibration of the geomagnetic polarity time scale for the Late Cretaceous and Cenozoic. *J. Geophys. Res.*, 100:6093–6095.
- Collett, T.S., Bird, K.J., Kvenvolden, K.A., and Magoon, L.B., 1988. Geologic interrelations relative to gas hydrates within the North Slope of Alaska. *Open-File Rep.—U.S. Geol. Surv.*, 88–389:150.

- Collett, T.S., Godbole, S.P., and Economides, C.E., 1984. Quantification of in-situ gas hydrates with well logs. *Proc. Annu. Tech. Meet. Petrol. Soc. CIM*, 35:571–582.
- Dickens, G.R., and Quinby-Hunt, M.S., 1994. Methane hydrate stability in seawater. *Geophys. Res. Lett.*, 21:2115–2118.
- Dillon, W.P., Grow, J.A., and Paull, C.K., 1980. Unconventional gas hydrate seals may trap gas off the Southeastern U.S. *Oil & Gas J.*, 78:124–130.
- Dillon, W.P., and Paull, C.K., 1983. Marine gas hydrates, II. Geophysical evidence. In Cox, J.L. (Ed.), *Natural Gas Hydrates: Properties, Occurrences, and Recovery*: Woburn, MA (Butterworth), 73–90.
- Duan, Z., Møller, N., Greenberg, J., and Weare, J.H., 1992. The prediction of methane solubility in natural waters to high ionic strength from 0° to 250°C and from 0 to 1600 bar. *Geochim. Cosmochim. Acta*, 56:1451–1460.
- Gradstein, F.M., and Sheridan, R.E., 1983. Introduction. In Sheridan R.E., Gradstein, F.M., et al., *Init. Repts. DSDP*, 76: Washington (U.S. Govt. Printing Office), 5–18.
- Heezen, B.C., Hollister, C.D., and Ruddiman, W.F., 1966. Shaping of the continental rise by deep geostrophic contour currents. *Science*, 152:502–508.
- Housen, B.A., and Musgrave, R.J., 1996. Rock-magnetic signature of gas hydrates in accretionary prism sediments. *Earth Planet. Sci. Lett.*, 139:509–519.
- Hovland, M., Lysne, D., and Whiticar, M., 1995. Gas hydrate and sediment gas composition, Hole 892A. In Carson, B., Westbrook, G.K., Musgrave, R.J., and Suess, E. (Eds.), *Proc. ODP. Sci. Results*, 146 (Pt. 1), 151–161.
- Katzman, R., Holbrook, W.S., and Paull, C.K., 1994. A combined vertical-incidence and wide-angle seismic study of a gas hydrate zone, Blake Ridge. *J. Geophys. Res.*, 99:17975–17995.
- Kawai, N., Yaskawa, K., Nakajima, T., Torii, M., and Horie, S., 1972. Oscillating geomagnetic field with a recurring reversal discovered from Lake Biwa. *Proc. Jpn. Acad.*, 48:186–190.
- Kvenvolden, K.A., and Kastner, M., 1990. Gas hydrates of the Peruvian outer continental margin. In Suess, E., von Huene, R., et al., *Proc. ODP. Sci. Results*, 112: College Station, TX (Ocean Drilling Program), 517–526.
- Kvenvolden, K.A., and McMenamin, M.A., 1980. Hydrates of natural gas: a review of their geologic occurrence. *Geol. Surv. Circ. (U.S.)*, 825.
- Lancelot, Y., and Ewing, J.I., 1972. Correlation of natural gas zonation and carbonate diagenesis in Tertiary sediments from the north-west Atlantic. In Hollister, C.D., Ewing, J.I., et al., *Init. Repts. DSDP*, 11: Washington (U.S. Govt. Printing Office), 791–799.
- Markl, R.G., and Bryan, G.M., 1983. Stratigraphic evolution of the Blake Outer Ridge. *AAPG Bull.*, 67:663–683.
- Markl, R.G., Bryan, G.M., and Ewing, J.I., 1970. Structure of the Blake-Bahama Outer Ridge. *J. Geophys. Res.*, 75:4539–4555.
- Mathews, M., 1986. Logging characteristics of methane hydrate. *The Log Analyst*, 27:26–63.
- Matsumoto, R., 1983. Mineralogy and geochemistry of carbonate diagenesis of the Pliocene and Pleistocene hemipelagic mud on the Blake Outer Ridge, Site 533, Leg 76. In Sheridan, R.E., Gradstein, F.M., et al., *Init. Repts. DSDP*, 76: Washington (U.S. Govt. Printing Office), 411–427.
- , 1989. Isotopically heavy oxygen-containing siderite derived from the decomposition of methane hydrate. *Geology*, 17:707–710.
- Needham, H.D., Habib, D., and Heezen, B.C., 1969. Upper Carboniferous palynomorphs as a tracer of red sediment dispersal patterns in the North-west Atlantic. *J. Geol.*, 77:113–120.
- Paull, C.K., and Dillon, W.P., 1981. Appearance and distribution of the gas hydrate reflector in the Blake Ridge region, offshore southeastern United States. *USGS Misc. Field Studies Map*, 1252.
- Pearson, C.F., Halleck, P.M., McGuire, P.L., Hermes, R., and Mathews, M., 1983. Natural gas hydrate deposit: a review of in-situ properties. *J. Phys. Chem.*, 87:4180–4185.
- Pettigrew, T.L., 1992. The design and preparation of a wireline pressure core sampler (PCS). *ODP Tech. Note*, 17: College Station, TX (Ocean Drilling Program).
- Prensky, S., 1995. A review of gas hydrates and formation evaluation of hydrate-bearing reservoirs. *Proc. SPWLA 36th Annu. Logging Symp.*, GGG.
- Schlumberger, 1989. *Log Interpretation Principles/Applications*: Houston, TX (Schlumberger Educ. Services).
- Ratcliffe, E.H., 1960. Thermal conductivities of ocean sediments. *J. Geophys. Res.* 65:1535–1541.
- Rowe, M.M., and Gettrust, J.F., 1993. Faulted structure of the bottom-simulating reflector on the Blake Ridge, western North Atlantic. *Geology*, 21:833–836.
- Ruppel, C., Von Herzen, R.P., and Bonneville, A., 1995. Heat flux through an old (~175 Ma) passive margin: offshore southeastern United States. *J. Geophys. Res.*, 100:20037–20057.
- Shipboard Scientific Party, 1972. Sites 102-103-104—Blake-Bahama Outer Ridge (northern end). In Hollister, C.D., Ewing, J.I., et al., *Init. Repts. DSDP*, 11: Washington (U.S. Govt. Printing Office), 135–218.
- , 1994. Sites 889 and 890. In Westbrook, G.K., Carson, B., Musgrave, R.J., et al., *Proc. ODP. Sci. Results*, 146 (Pt. 1): College Station, TX (Ocean Drilling Program), 127–239.
- Shipley, T.H., Houston, M.H., Buffler, R.T., Shaub, F.J., McMillen, K.J., Ladd, J.W., and Worzel, J.L., 1979. Seismic evidence for widespread possible gas hydrate horizons on continental slopes and rises. *AAPG Bull.*, 63:2204–2213.
- Sloan, E.D., 1990. *Clathrate Hydrates of Natural Gases*: New York (Marcel Dekker).
- Smith, J.D., and Foster, J.H., 1969. Geomagnetic reversal in Brunhes normal polarity epoch. *Science*, 163:565–567.
- Tucholke, B.E., Bryan, G.M., and Ewing, J.I., 1977. Gas hydrate horizon detected in seismic reflection profiler data from the western North Atlantic. *AAPG Bull.*, 61:698–707.
- Tucholke, B.E., and Mountain, G.S., 1979. Seismic stratigraphy, lithostratigraphy, and paleosedimentation patterns in the North American Basin. In Talwani, M., Hay, W., and Ryan, W.B.F. (Eds.), *Deep Drilling Results in the Atlantic Ocean: Continental Margins and Paleoenvironment*. Am. Geophys. Union, Maurice Ewing Ser., 3:58–86.

Ms 164IR-110

NOTE: Core-description forms (“barrel sheets”) and core photographs can be found in Section 4, beginning on page 337. Forms containing smear-slide data can be found in Section 5, beginning on page 599.

SHORE-BASED LOG PROCESSING

HOLE 997B

Bottom felt: 2781.6 mbrf

Total penetration: 750.7 mbsf

Total core recovered: 242.8 m (66.6%)

Logging Runs

Logging string 1: DITE/SDT/HLDT/NGT/LDEO-TLT

Logging string 2: AACT/GST/NGT

Logging string 3: LDEO-SST

Logging string 4: FMS/GPIT/NGT (2 runs)

A wireline heave compensator was used to counter ship heave.

Bottom-Hole Assembly Depths

The following bottom-hole assembly depths are as they appear on the logs after differential depth shift (see "Depth Shift" section) and depth shift to the seafloor. As such, there might be a discrepancy with the original depths given by the drillers on board. Possible reasons for depth discrepancies are ship heave, the use of the wireline heave compensator, and drill string and/or wireline stretch.

DITE/SDT/HLDT/NGT: Bottom-hole assembly at ~113 mbsf.

AACT/GST/NGT: Bottom-hole assembly at ~114.5 mbsf.

FMS/GPIT/NGT: Bottom-hole assembly at ~114.5 mbsf.

Processing

Depth shift: Original logs have been interactively depth shifted with reference to the NGT from FMS/GPIT/NGT pass 2 and to the seafloor (-2775.5 m). This amount corresponds to the depth of the seafloor as seen on the logs and differs 6.1 m from the "bottom felt" depth given by the drillers.

Gamma-ray processing: Data have been processed to correct for borehole size and type of drilling fluid.

Acoustic data processing: The array sonic tool was operated in the standard depth-derived borehole compensated, long (8-10-10-12 ft.) spacing mode. Above 450 mbsf, the logs have been processed to eliminate some of the noise and cycle skipping experienced during the recording. Because of the occurrence of free gas both in the formation and in the borehole from 450 mbsf to TD, the propagation of acoustic waves between the tool source and the receivers was affected. The receivers would pick up only a very low-amplitude signal, and the data acquisition computer had difficulty selecting the arrival times. As a result, the acoustic data from below 450 m are highly unreliable, and accurate sonic waveform processing is required to get valuable formation velocities. No processed acoustic data are presented from below 450 mbsf.

Geochemical processing: The elemental yields recorded by the GST tool represent the relative contribution of only some of the rock-forming elements (iron, calcium, chlorine, silicon, sulfur, hydrogen, gadolinium, and titanium—the last two computed during geochemical processing) to the total spectrum. Because other rock-forming elements are present in the formation (such as aluminum, potassium, and so on), caution is recommended in using the yields to infer lithologic changes. Instead, ratios (see file *acronyms.doc* on CD-ROM in back pocket, this volume) are more appropriate to determine changes in the macroscopic properties of the formation. A list of oxide factors used in geochemical processing includes the following:

$\text{SiO}_2 = 2.139$

$\text{CaCO}_3 = 2.497$

$\text{FeO}^* = 1.358$

$\text{TiO}_2 = 1.668$

$\text{K}_2\text{O} = 1.205$

$\text{Al}_2\text{O}_3 = 1.889$

FeO^* computed using an oxide factor that assumes a 50:50 combination of Fe_2O_3 and FeO factors.

Quality Control

Invalid density spikes were recorded at 612–615, 621, 629, and 637–638 mbsf.

Data recorded through bottom-hole assembly, such as the gamma-ray data from above 113 mbsf, should be used qualitatively only because of the attenuation on the incoming signal. Invalid gamma-ray data were recorded at 60.5–64, 87.5–91.5, and 111.5–114 mbsf on the AACT/GST/NGT run.

Hole diameter was recorded by the hydraulic caliper on the HLDT tool (CALI) and the caliper on the FMS string (C1 and C2).

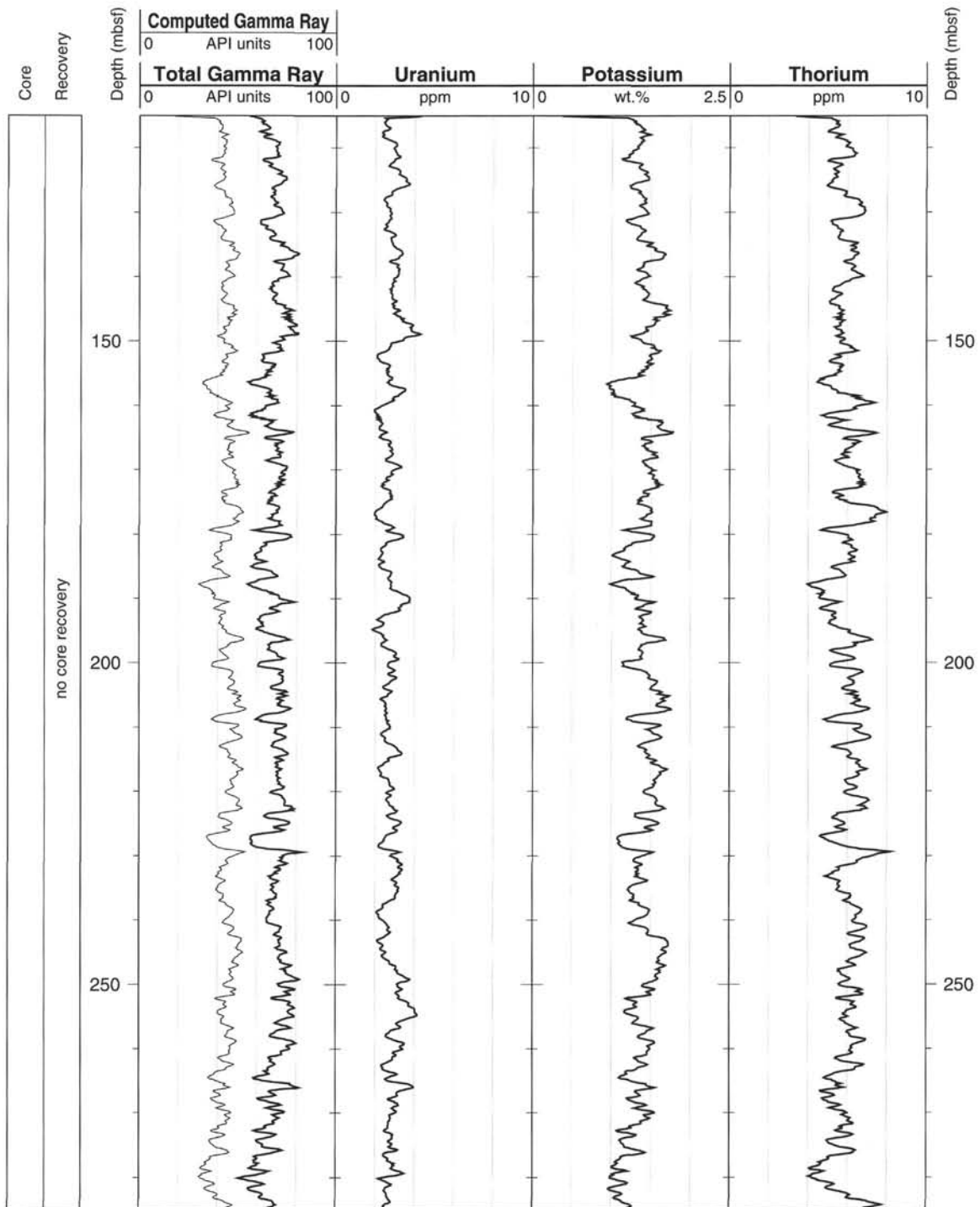
The results of geochemical processing are presented along with the calcium carbonate measurements performed on board. FACT = quality control curve in geochemical processing. Accuracy of the estimates is inversely proportional to the magnitude of the curve.

Details of standard shore-based processing procedures are found in the "Explanatory Notes" chapter (this volume). For further information about the logs, please contact:

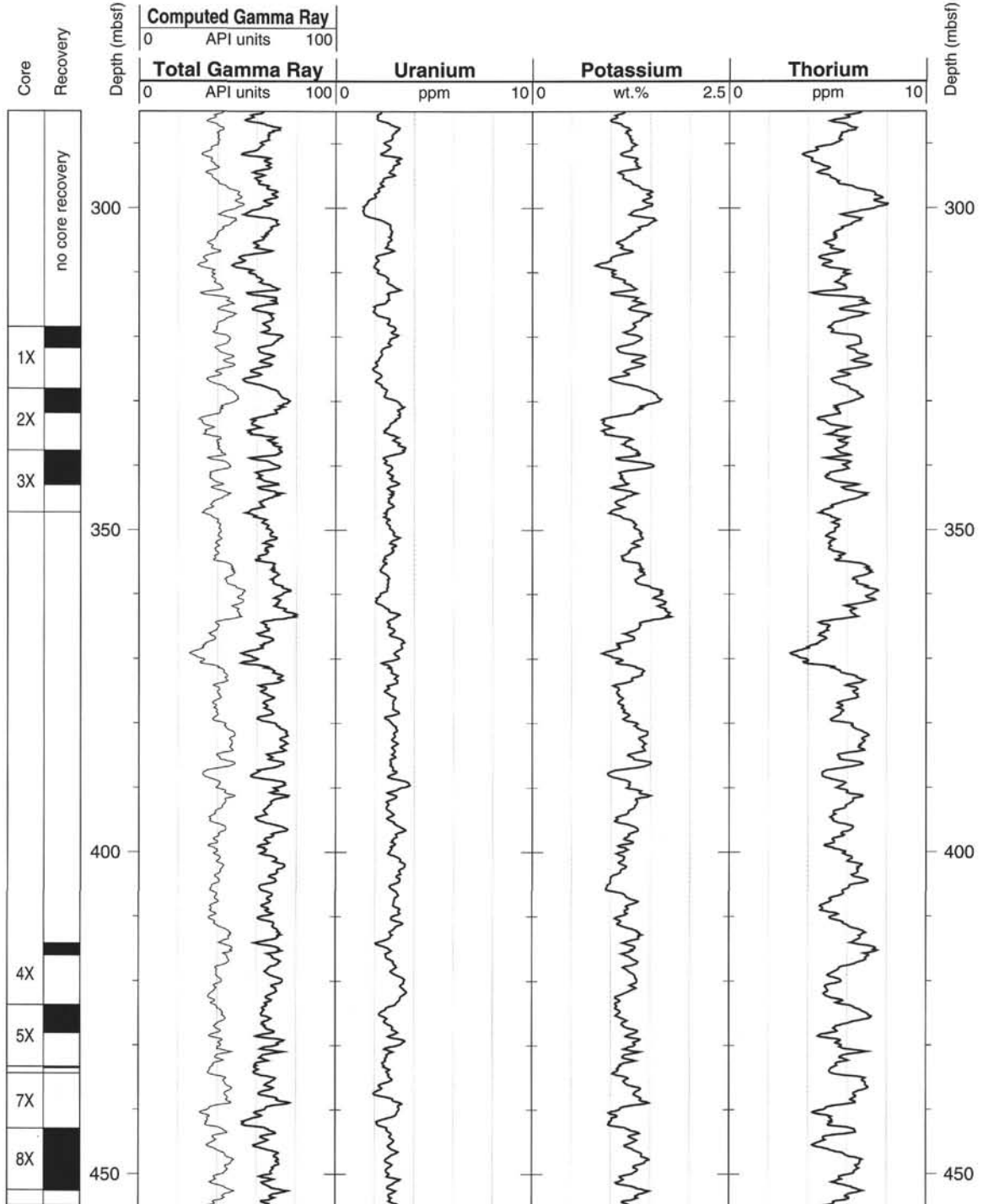
Cristina Broglia
Phone: 914-365-8343
Fax: 914-365-3182
E-mail: chris@ldeo.columbia.edu

Elizabeth Pratson
Phone: 914-365-8313
Fax: 914-365-3182
E-mail: beth@ldeo.columbia.edu

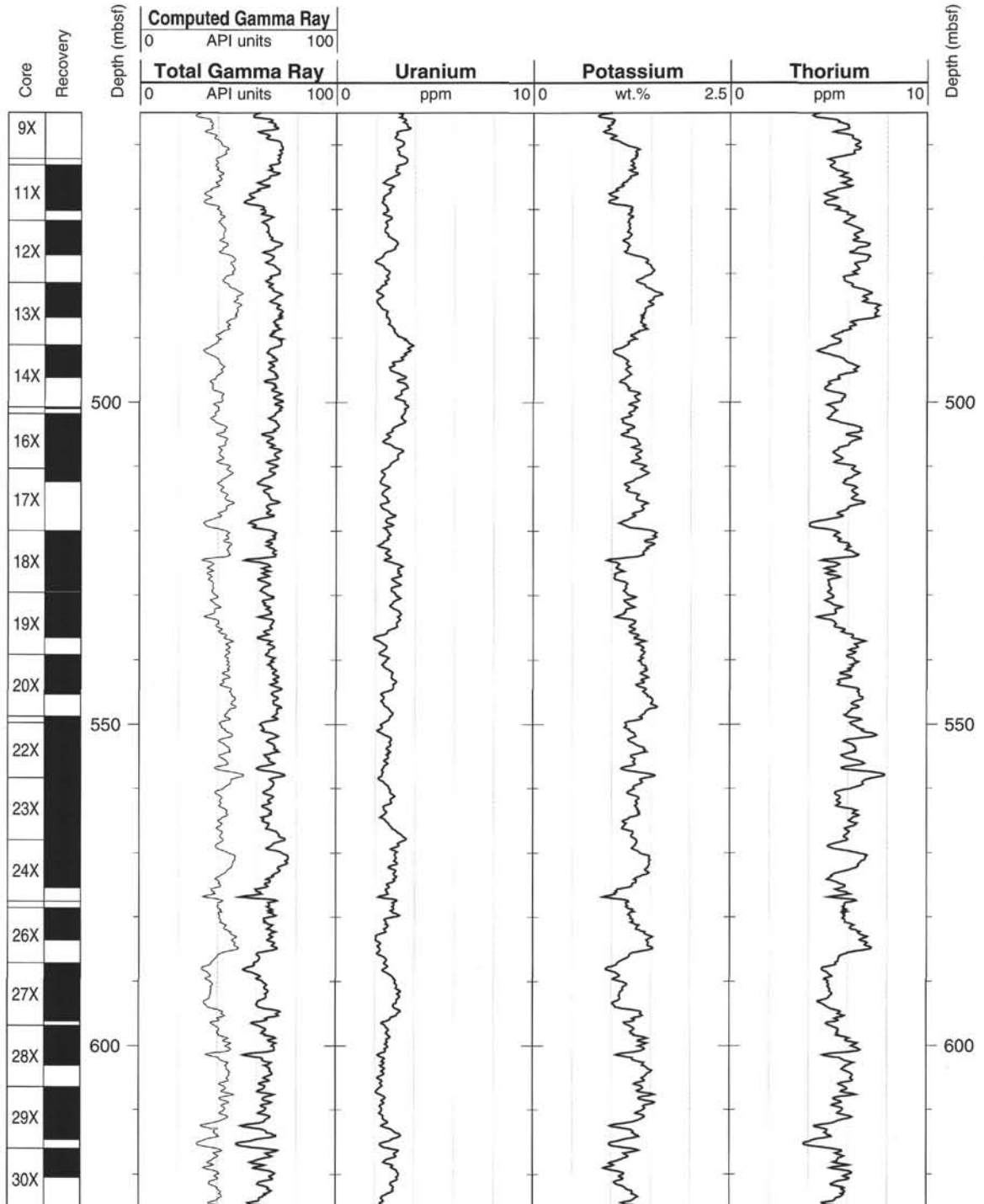
Hole 997B: Natural Gamma Ray Logging Data



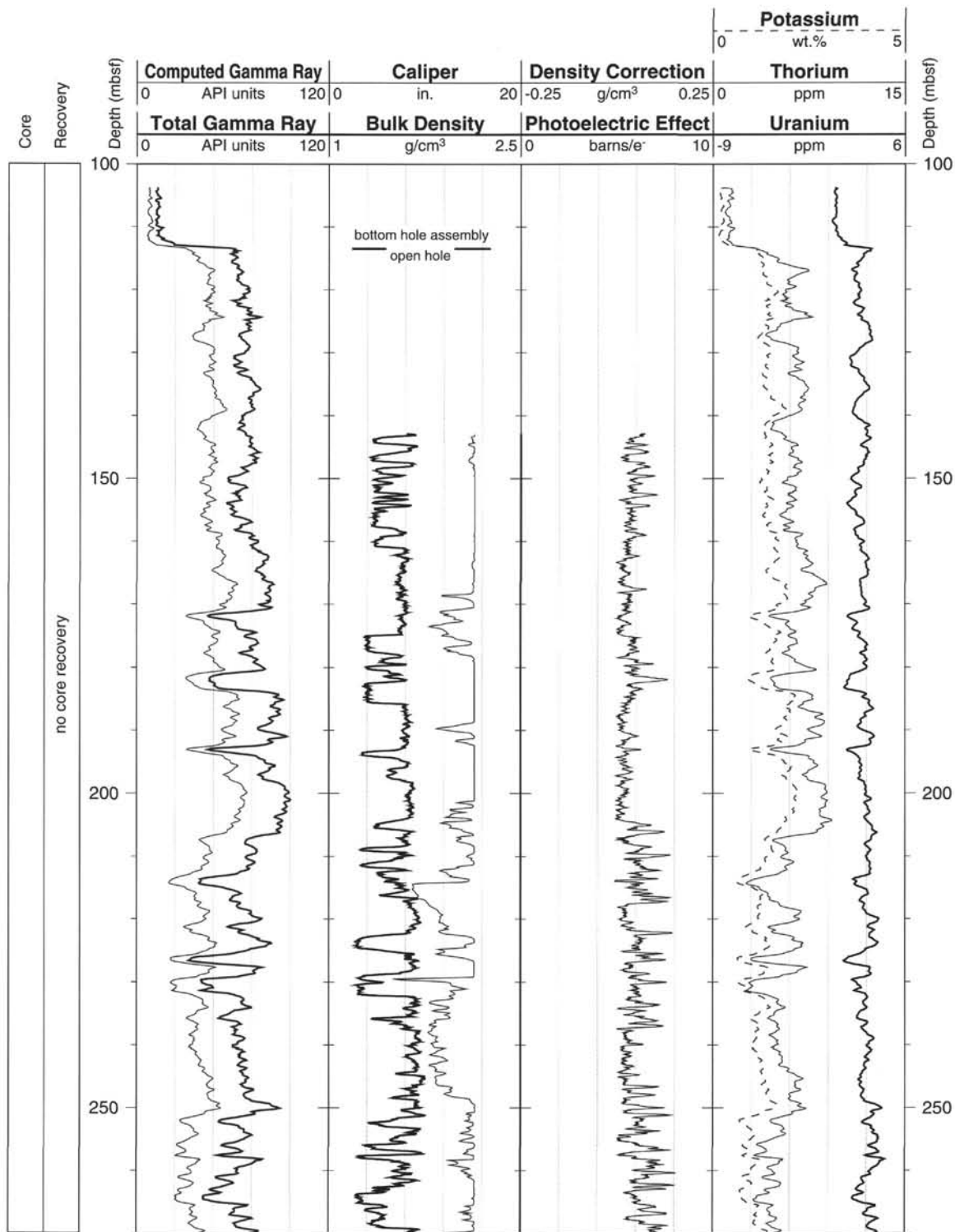
Hole 997B: Natural Gamma Ray Logging Data (cont.)



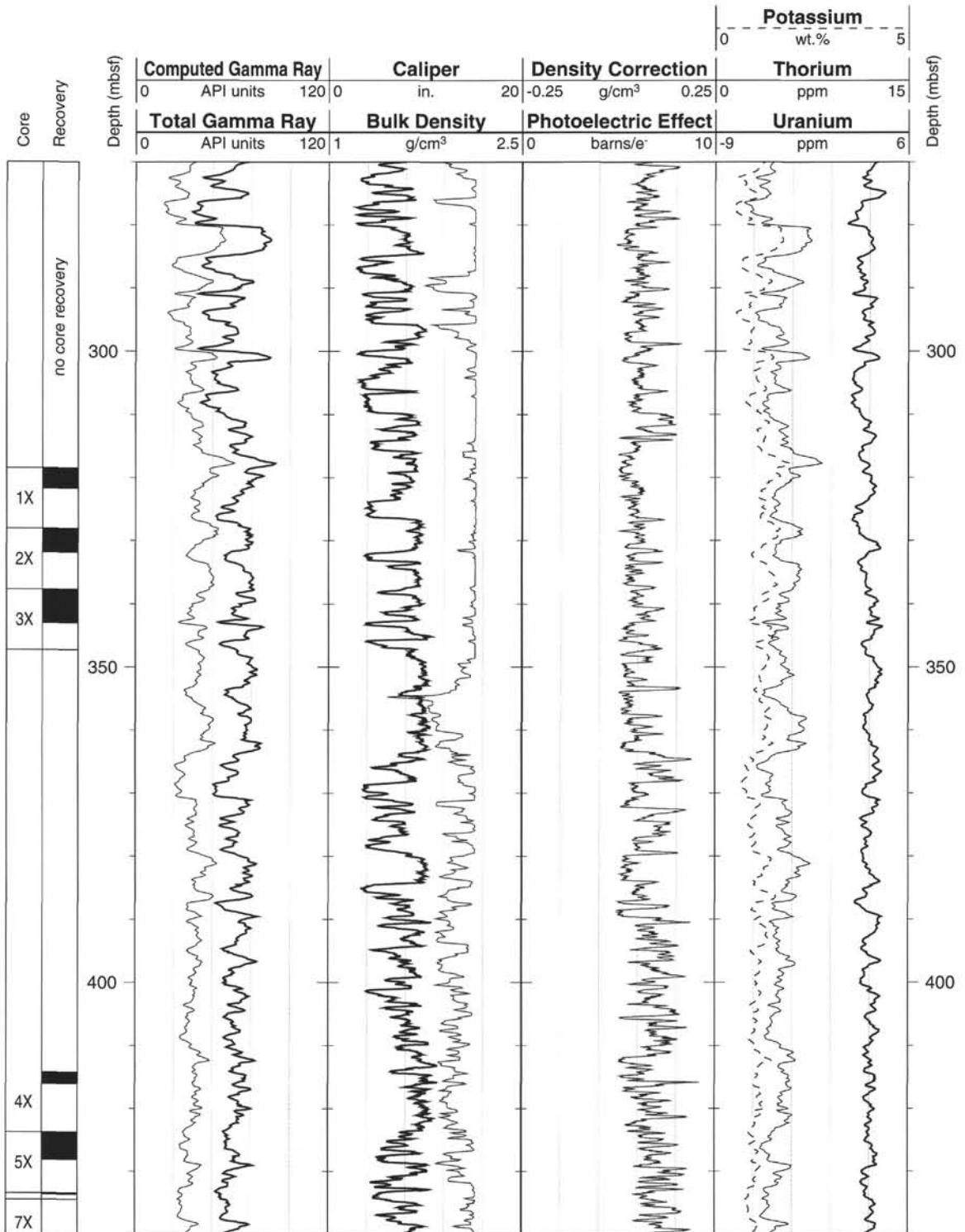
Hole 997B: Natural Gamma Ray Logging Data (cont.)



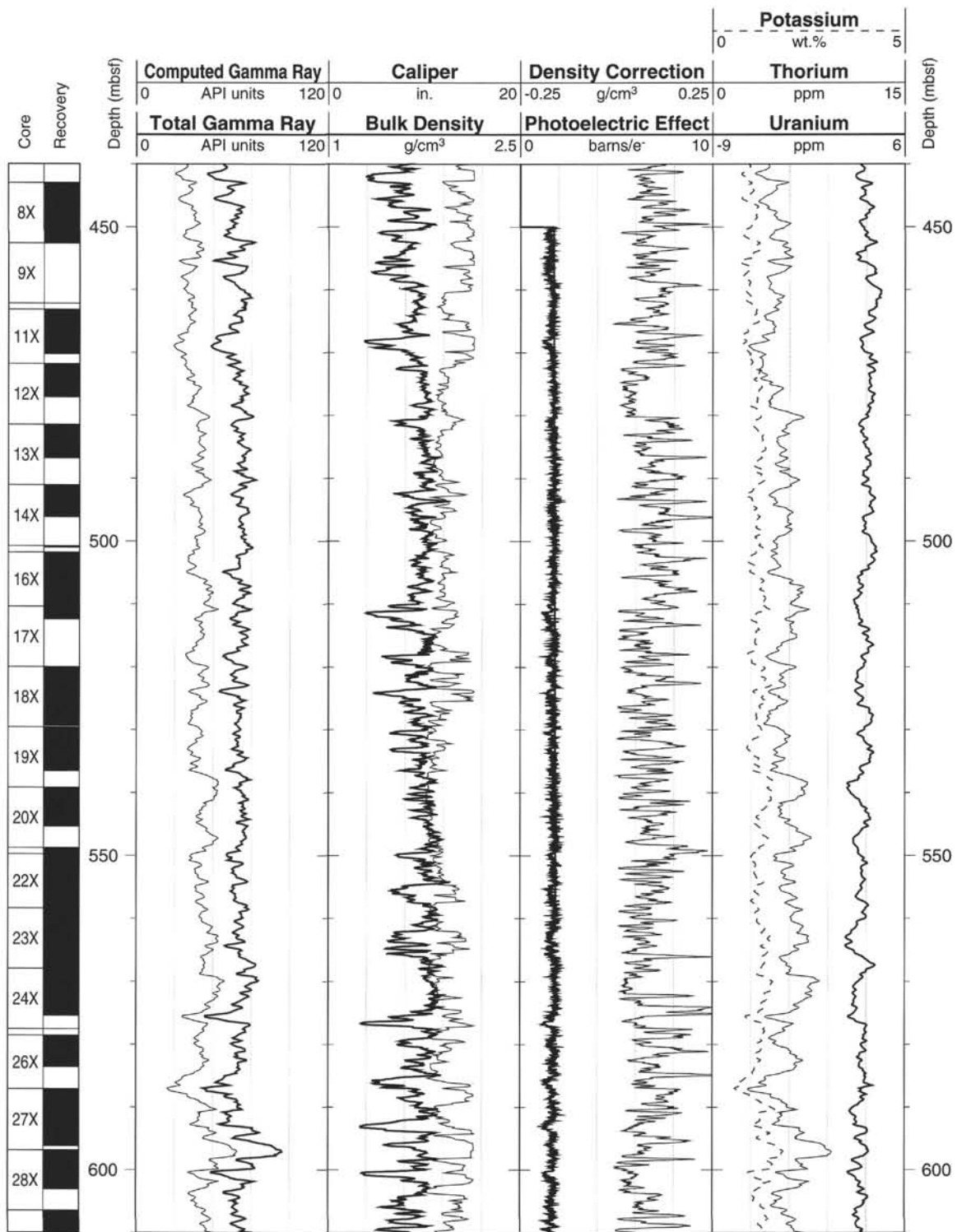
Hole 997B: Natural Gamma Ray-Density Logging Data



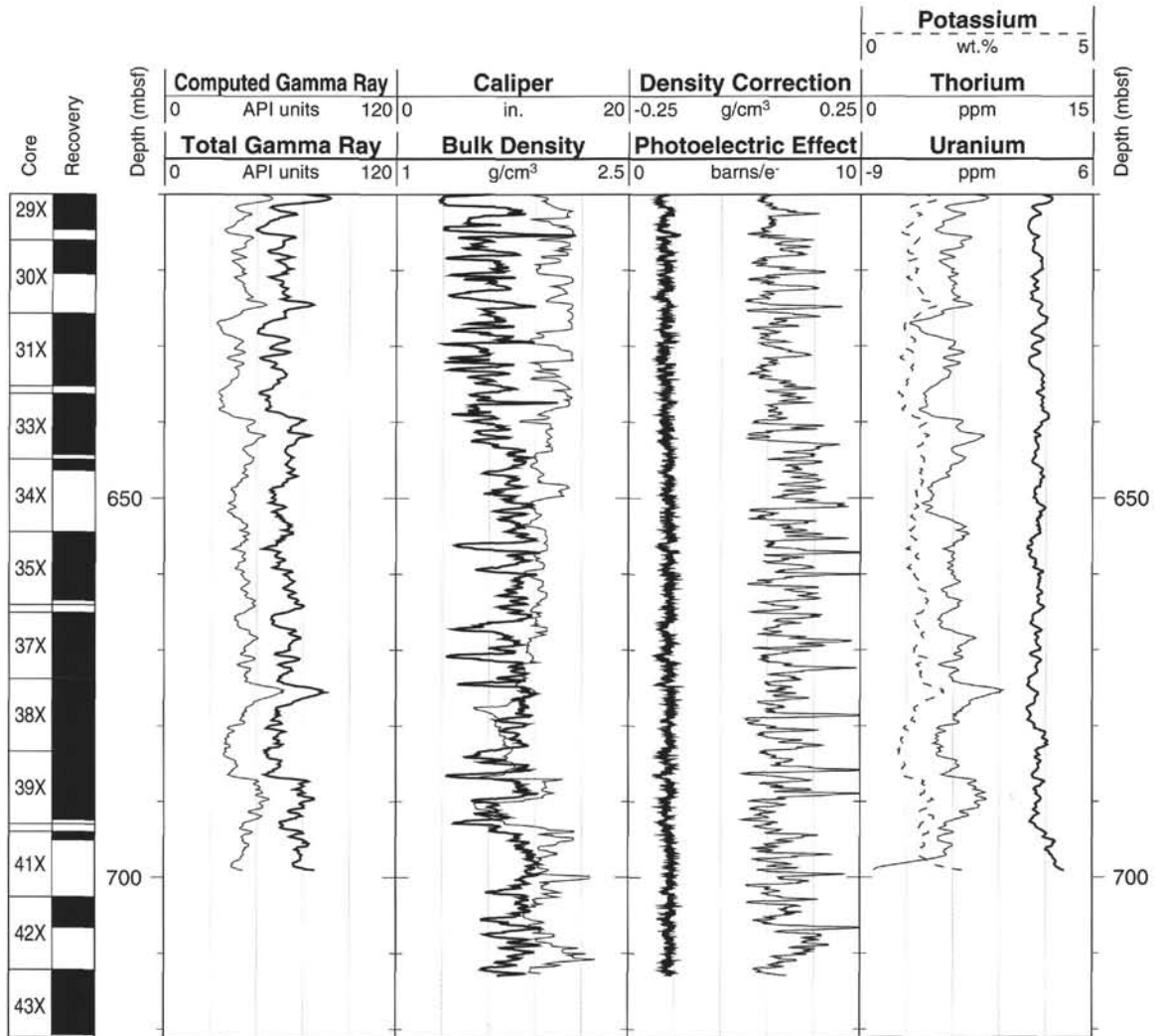
Hole 997B: Natural Gamma Ray-Density Logging Data (cont.)



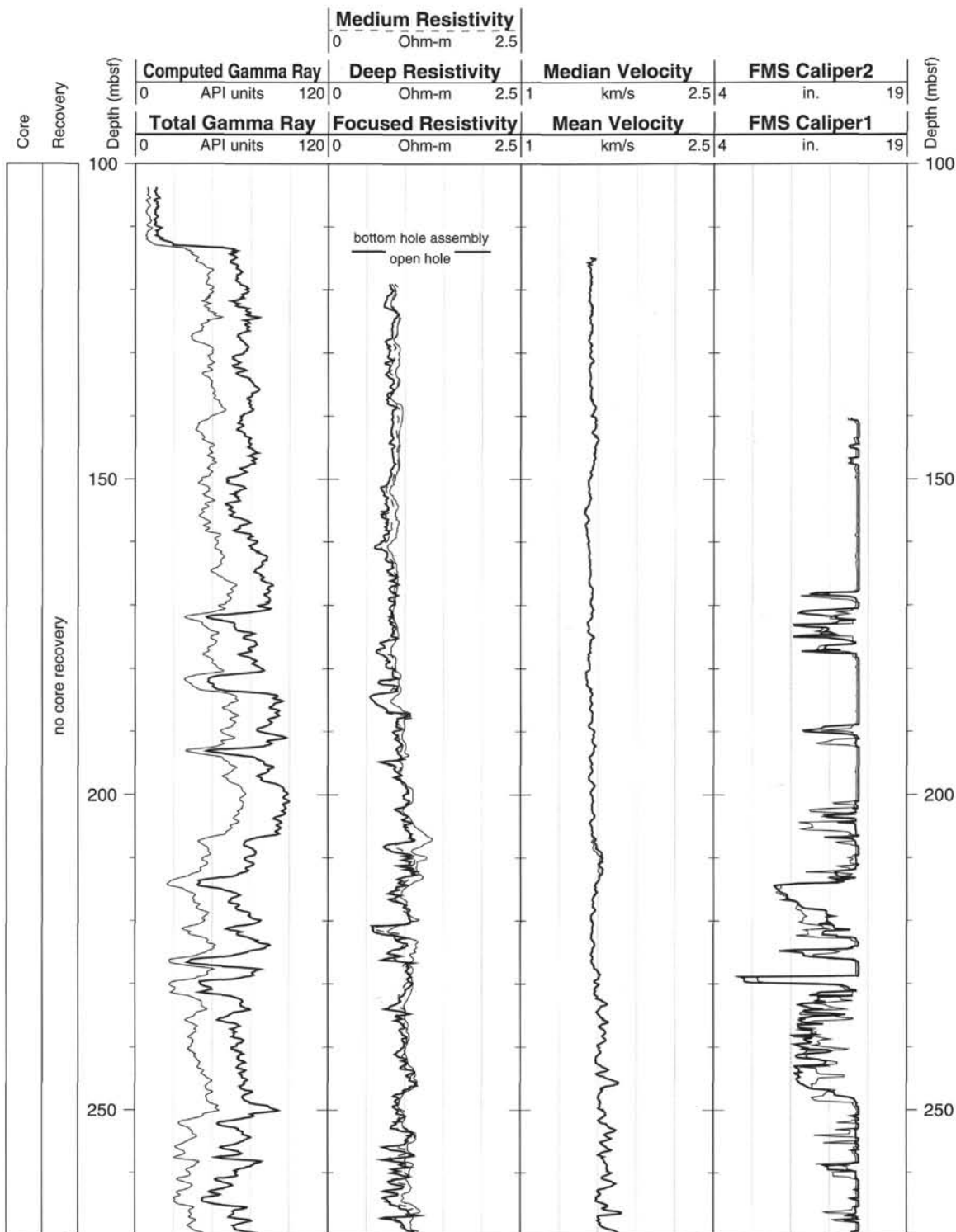
Hole 997B: Natural Gamma Ray-Density Logging Data (cont.)



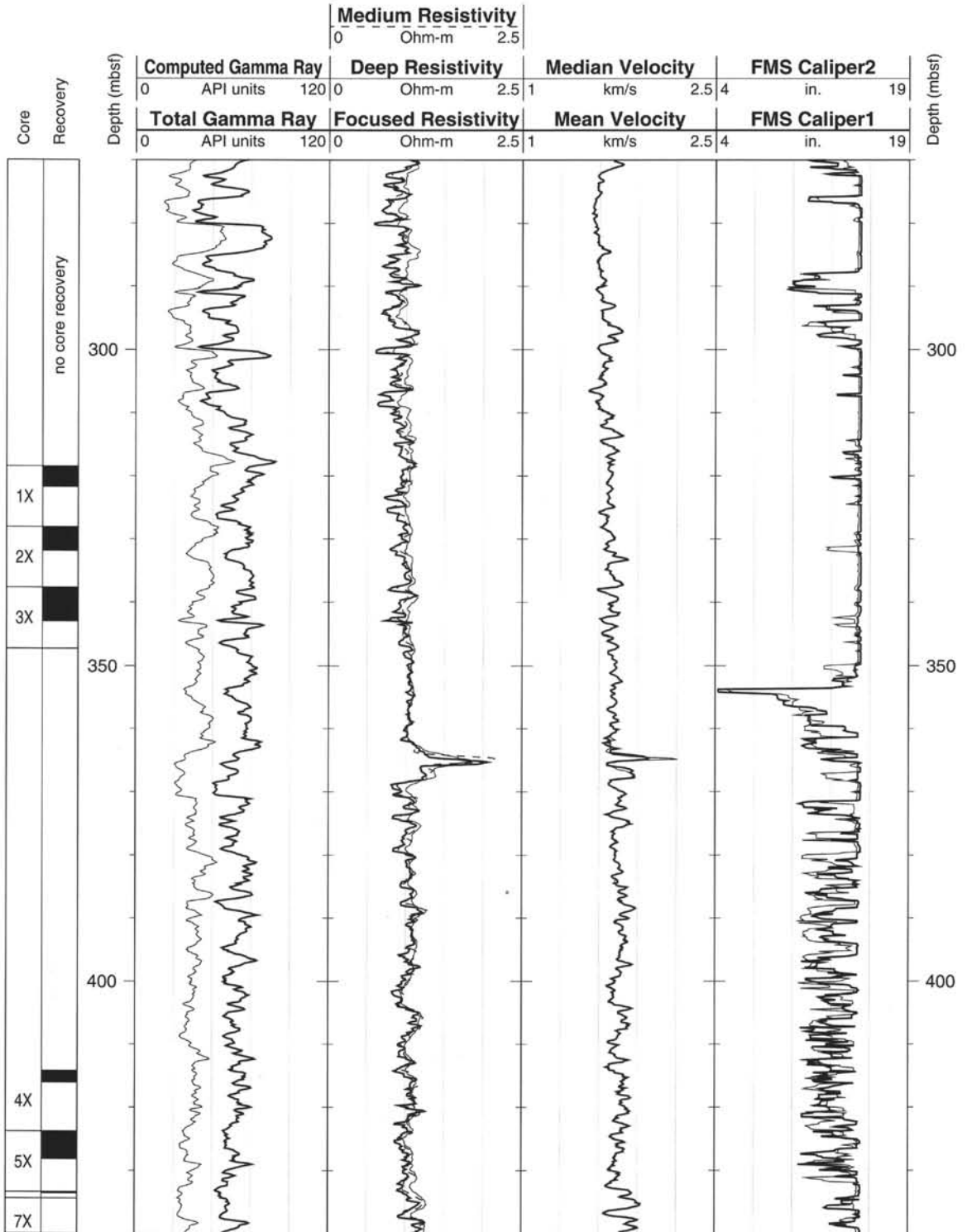
Hole 997B: Natural Gamma Ray-Density Logging Data (cont.)



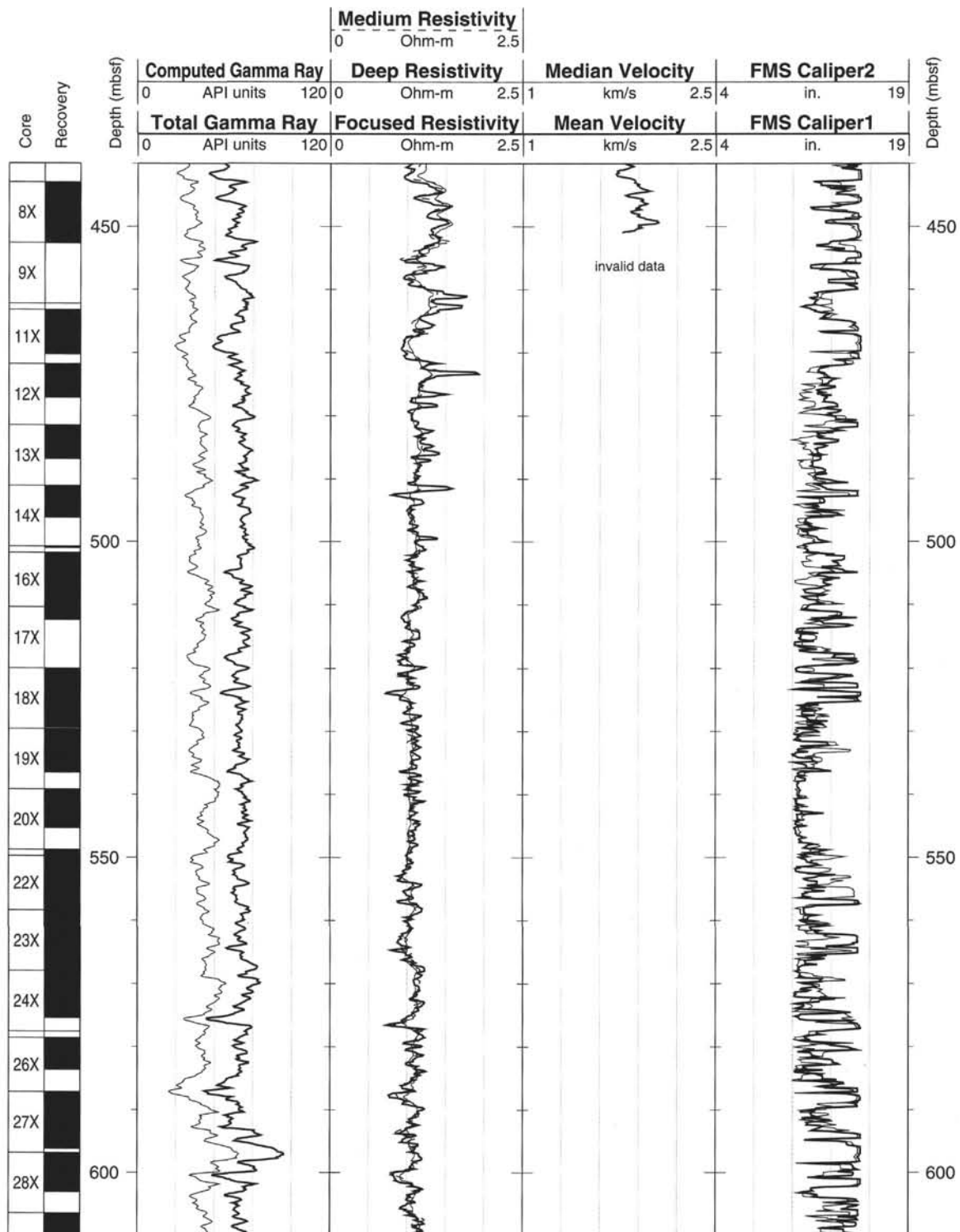
Hole 997B: Natural Gamma Ray-Resistivity-Sonic Logging Data



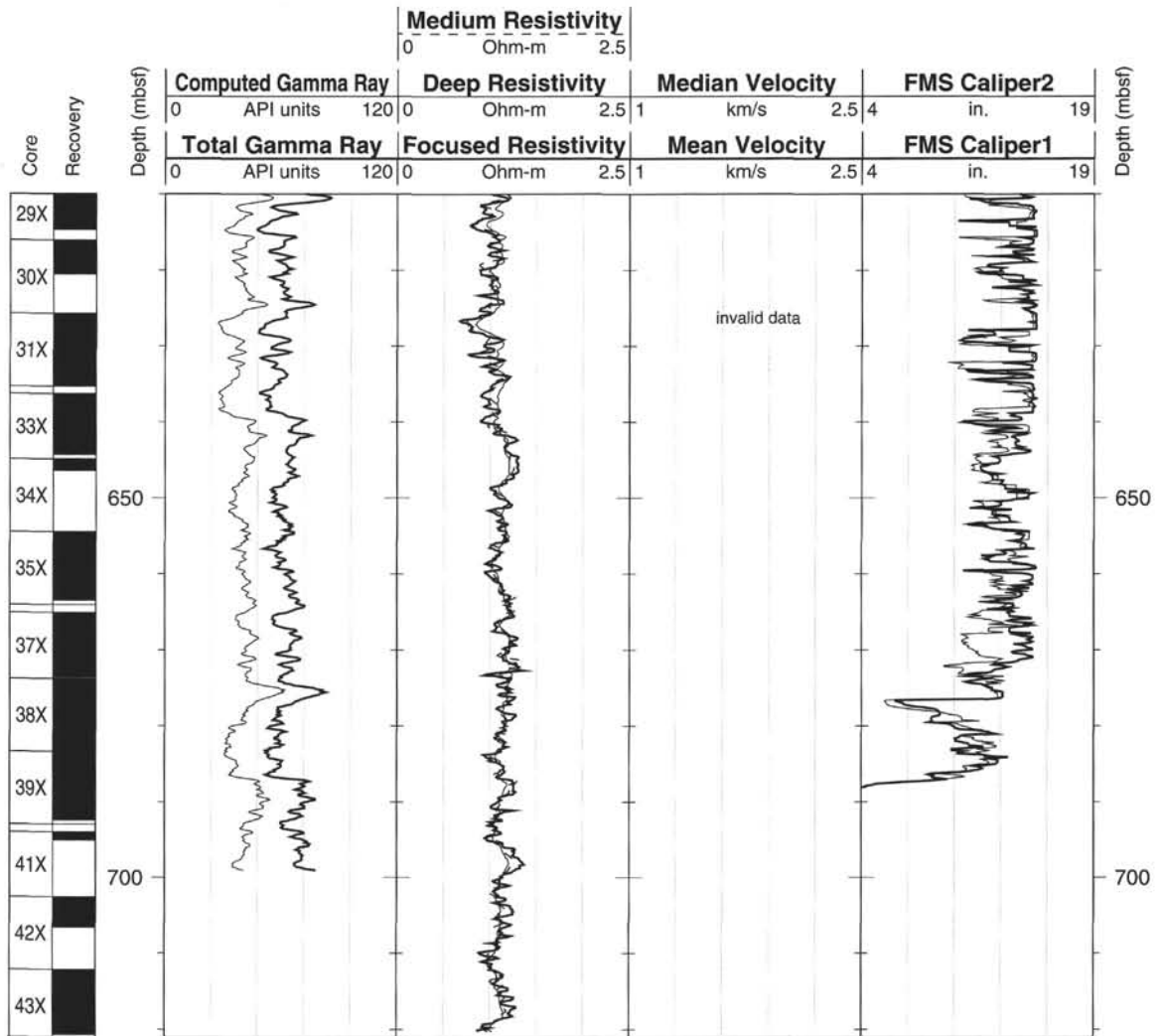
Hole 997B: Natural Gamma Ray-Resistivity-Sonic Logging Data (cont.)



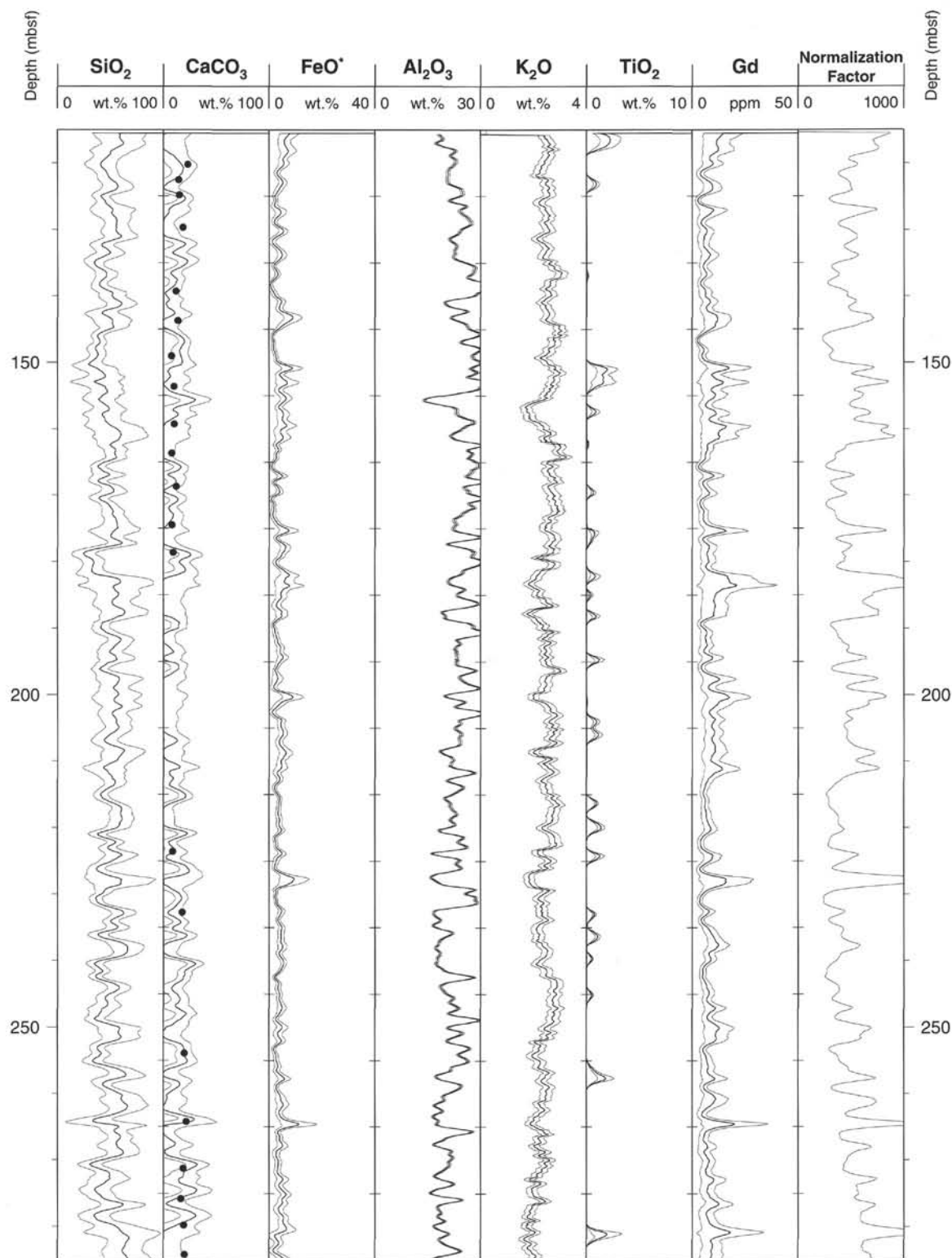
Hole 997B: Natural Gamma Ray-Resistivity-Sonic Logging Data (cont.)



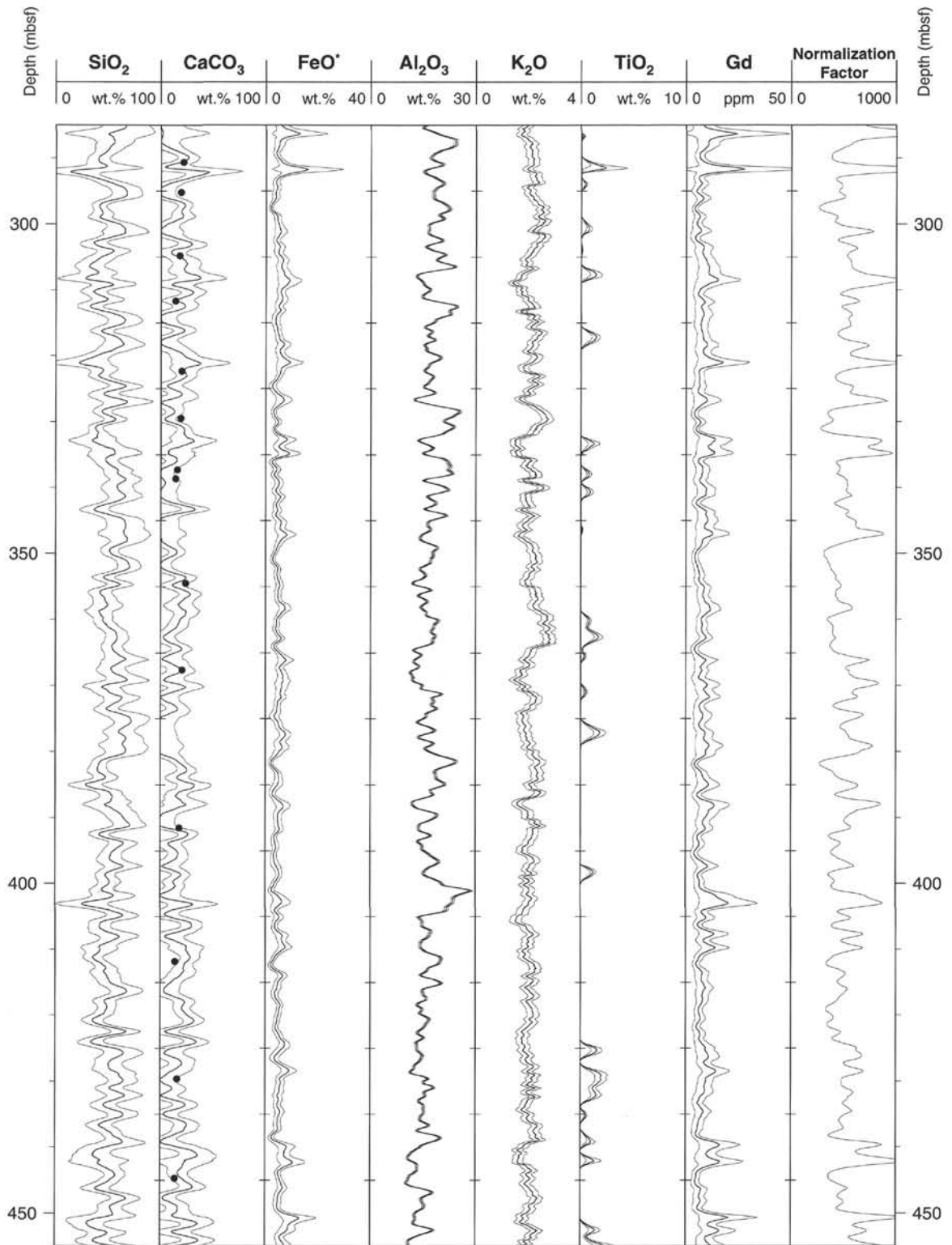
Hole 997B: Natural Gamma Ray-Resistivity-Sonic Logging Data (cont.)



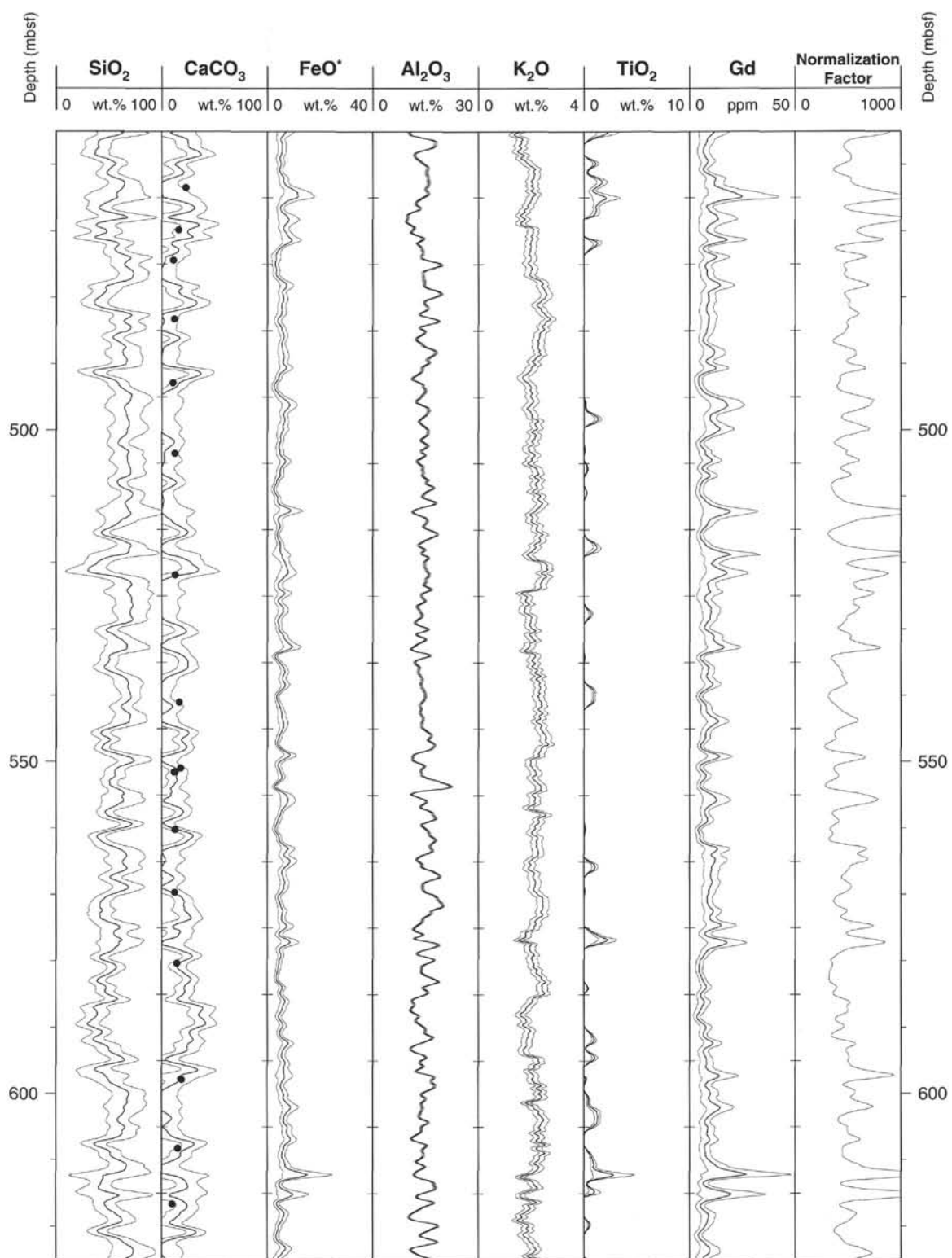
Hole 997B: Geochemical Logging Data



Hole 997B: Geochemical Logging Data (cont.)



Hole 997B: Geochemical Logging Data (cont.)



Hole 997B: Geochemical Logging Data (cont.)

